Journal of Materials Chemistry A

This article can be cited before page numbers have been issued, to do this please use: Z. Chen, X. Duan, W. Wei, S. Wang and B. Ni, *J. Mater. Chem. A*, 2019, DOI: 10.1039/C9TA03220G.

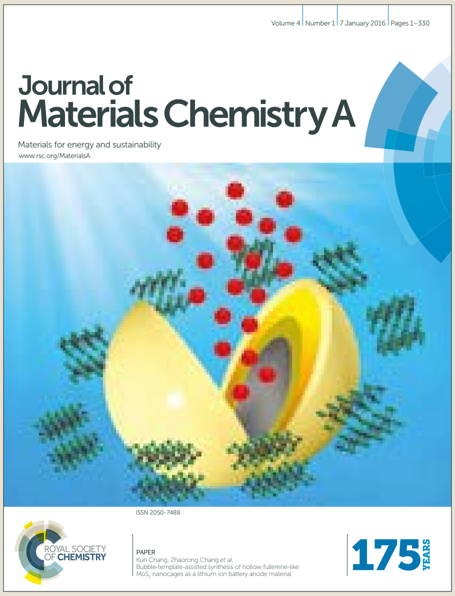

Volume 4 | Number 1 | 7 January 2016 | Pages 1–330

Journal of Materials Chemistry A

Materials for energy and sustainability
www.rsc.org/MaterialsA

ISSN 2050-7488

ROYAL SOCIETY OF CHEMISTRY

PAPER
Kun Chang, Zhaorong Chang *et al.*
Bubble-template-assisted synthesis of hollow fullerene-like MoS_2 nanocages as a lithium ion battery anode material

175 YEARS

ROYAL SOCIETY OF CHEMISTRY

rsc.li/materials-a

Table of Contents Entry

View Article Online
DOI: 10.1039/C9TA03220G

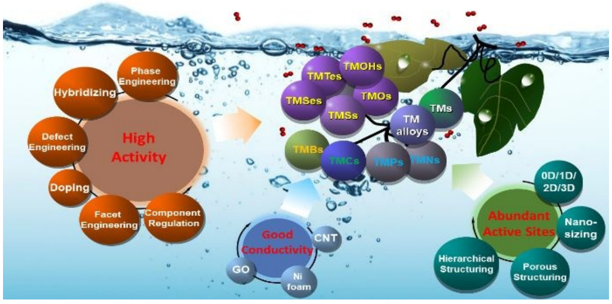

Transition Metal-Based Electrocatalysts for Alkaline Hydrogen Evolution Reaction.

View Article Online
DOI: 10.1039/C9TA03220G

Recent Advances in Transition Metal-Based Electrocatalysts for Alkaline Hydrogen Evolution

Zhijie Chen,[a] Xiaoguang Duan,[b] Wei Wei,[a] Shaobin Wang,[b] Bing-Jie Ni[a,*]

[a] *Centre for Technology in Water and Wastewater, School of Civil and Environmental Engineering, University of Technology Sydney, NSW 2007, Australia*

[b] *School of Chemical Engineering, The University of Adelaide, South Australia 5005, Australia*

*Corresponding Author: Bing-Jie Ni

Tel.: +61 295147401; E-mail: bingjieni@gmail.com

View Article Online
DOI: 10.1039/C9TA03220G

Abstract

With the increasing demands in energy consumption and raising environmental concerns, it is of vital significance for developing renewable and clean energy sources to substitute traditional fossil fuels. As an outstanding candidate, hydrogen is recognized as a green energy carrier for its high gravimetric energy density, zero carbon footprints, and earth-abundance. Currently, water splitting in alkaline electrolytes represents one of the most promising methods for sustainable hydrogen production, and the key challenge lies in the development of high-performance electrocatalysts for hydrogen evolution reaction (HER). Given the rapid advances in the design and development of efficient catalysts towards alkaline HER, especially the capable transition metal (TM)-based materials, this review aims to summarise recent progress in the theoretical understanding of alkaline HER and the TM-based electrocatalysts. TM-based catalysts classified by their different anionic compositions (metals, alloys, oxides, hydroxides, sulfides, selenides, tellurides, nitrides, phosphides, carbides, and borides) are comprehensively showcased. Special attention is given to the mainstream strategies that can upgrade the catalytic properties of each category, as well as the underlying structure-activity regimes. Additionally, the challenges for the future development of novel catalysts are also analyzed.

Keywords: water splitting; alkaline hydrogen evolution reaction; transition metals; electrocatalysts

View Article Online
DOI: 10.1039/C9TA03220G

1. Introduction

Developing sustainable and clean energy supplies to substitute traditional fossil fuels has aroused great concerns because of the approaching environmental and energy crisis.[1, 2] In the last few decades, renewable energy resources (e.g., solar, wind, and geothermal) have been extensively explored as sustainable alternatives for conventional fossil fuels. However, the spatial and temporal distribution of these energy sources has deeply limited their large-scale application.[3, 4] Hydrogen has been recognized as a green energy carrier for its high gravimetric energy density, environmental friendliness, and earth-abundance.[4, 5] Hitherto, industrial hydrogen production is largely dominated by steam methane reforming and coal gasification, whereas these processes are intensive energy consuming and will result in low hydrogen purity with massive pollutant/carbon emissions.[6, 7] Alternatively, water electrocatalysis is a clean and sustainable approach to produce high-purity hydrogen (>99%).

Electrocatalytic water splitting can be conducted in both acidic and alkaline solutions. Currently, acidic HER is limited by the unsatisfactory stability of the metal catalyst and poor membrane permanence.[8] In contrast, alkaline electrolyzers are technologically well developed and are commercially available.[9] Furthermore, alkaline hydrogen evolution is also an important reaction in the chlor-alkali process.[10] Herein, renovating alkaline HER techniques is of crucial importance to fulfill the enormous demands for hydrogen energy. Unfortunately, HER in alkaline electrolytes is strictly hampered by the sluggish kinetics.[5] To accelerate HER, numerous catalysts have been developed in recent years. Platinum group metals (PGMs, e.g., Pt and Pd) based materials are the most attractive HER catalysts, which possess low overpotentials, low Tafel slopes, high exchange current densities, and remarkable stabilities in water reduction reactions. Nevertheless, the

View Article Online
DOI: 10.1039/C9TA03220G

prohibitive costs and scarcity of these noble metals limit the commercial application of PGMs catalysts. The earth-abundant transition metals (TMs) based catalysts also show great potentials for alkaline HER. The commonly applied TMs based electrocatalysts include TMs, TM alloys, and TMXs (X= O, S, Se, Te, N, P, C, and B). These materials have been extensively studied, and to our delight, some exhibit extremely high capability in HER even comparable to that of PGMs-based catalysts.

To date, a handful of reviews have been dedicated with focusses on the mechanisms, challenges, and emerging strategies in alkaline HER.[7, 11, 12] For electrocatalysts, Jamesh et al. analyzed the earth-abundant-elements based catalysts for alkaline HER.[13] Gong et al. reviewed the Ni-based catalysts,[4] and Wei et al. summarised the heterostructure materials including Pt- (Pt/Ni(OH)$_2$) and MoS$_2$ -based catalysts.[3] Lately, the compelling role of anions in electrocatalysts has been extensively researched.[14-19] This review aims to not only offer a comprehensive overview of the latest progress of TMs (mainly refer to non-noble metals) based catalysts grouped by different anionic elements but also identify the advanced strategies to precisely regulate the atomic structure and electronic configurations of the electrocatalysts toward alkaline HER.

Herein, we will first discuss the electrochemistry of alkaline HER and several popular parameters/indexes for evaluating the properties of catalysts. Second, fruitful achievements of TM-based catalysts will be described classified by different anionic elements, including TMs, TM alloys, TMOs, LDHs, TMSs, TMSes, TMTes, TMNs, TMPs, TMCs, and TMBs. Particularly, the state-of-the-art strategies for tailoring the catalytic performance and features of different classified catalysts are highlighted (**Scheme 1**). The underlying structure-performance mechanisms will be unveiled. Finally,

View Article Online
DOI: 10.1039/C9TA03220G

we present the major challenges and future perspectives in this booming field. We hope that this timely and comprehensive review will inspire more future studies to advance the design principles and promote the application of TMs based catalysts with respectful performance for HER in alkaline electrolytes.

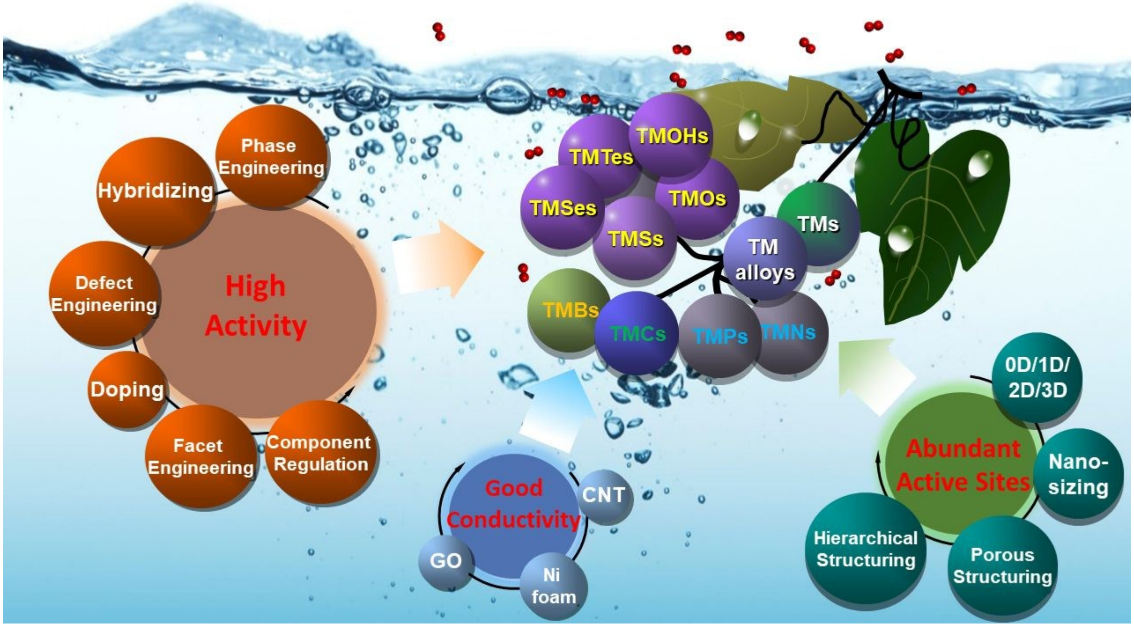

Scheme 1. Transition Metal-Based Electrocatalysts for Alkaline Hydrogen Evolution

2. Electrochemistry of hydrogen evolution in alkaline solution

2.1 General mechanisms of alkaline HER

The HER in alkaline solution begins with water adsorption and dissociation process which can generate H* by breaking the H-O-H bonds. It is widely recognized that this process is the rate-determining step (RDS) in HER because extra energy is required to produce protons. Commonly, the alkaline HER follows the classical Volmer-Heyrovsky process or the Volmer-Tafel process (**Figure 1**, Equations 1-3).

Volmer step: $H_2O + e^- \rightarrow H^* + OH^-$ (1)

Heyrovsky step: $H^* + H_2O + e^- \rightarrow H_2 + OH^-$ (2)

View Article Online
DOI: 10.1039/C9TA03220G

$$\text{Tafel step: } 2H^* \rightarrow H_2 \qquad (3)$$

Apart from the reduction of protons into adsorbed H*, the Volmer step in alkaline electrolytes involves two key steps, the adsorption and dissociation of water molecules over the catalyst surface.[4] These multi-step surface reactions make the Volmer step more intricate than that of the acidic HER in which the sophisticated "volcano plot" successfully correlates the intrinsic catalytic activity of the catalysts with the adsorption energy of H atoms. However, there have not yet highly developed principles to describe the complicated alkaline HER process.

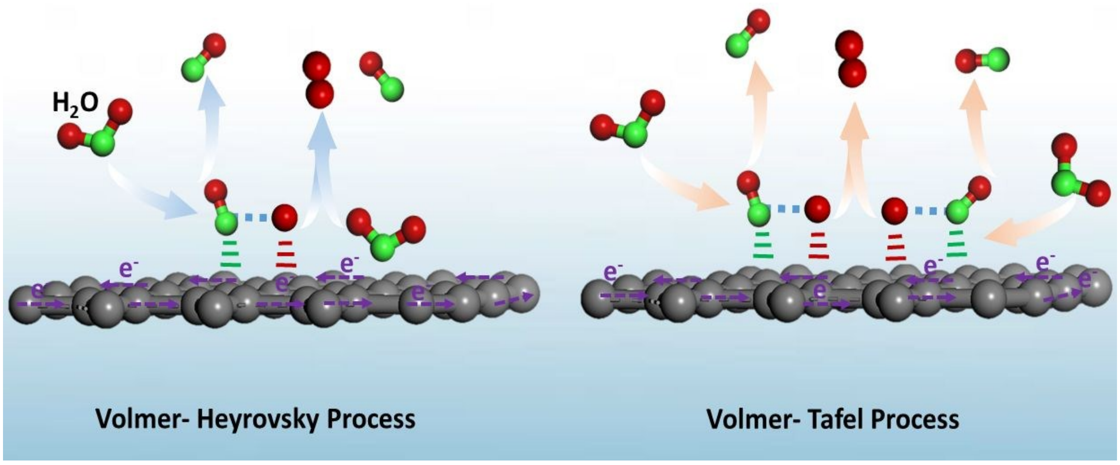

Figure 1. Schematic diagram of the Volmer-Heyrovsky and Volmer-Tafel processes on a catalyst surface.

Most of the research articles and reviews reported that the inferior performance of electrocatalysts in alkaline solution to the acidic one is due to the extra energy required in the Volmer step.[4, 20] However, several emerging catalysts (e.g., Ru-MoO_2,[21] MoO_2/α-Mo_2C,[22] Mo_2C,[23, 24] Mo_2C/G-NCS,[25] C-CWC,[26] DR-MoP,[27] $NiCo_2P_2$-ACNT,[28] NCP,[29] $NiCo_2P_x$,[30] Ni-Cu-P[31]) have been developed which are active both in acid and alkaline media and demonstrate better catalytic capability in alkaline electrolytes than in acidic media. Nevertheless, there is a lack of understanding of their better performance in alkaline solutions.

View Article Online
DOI: 10.1039/C9TA03220G

2.2 Energetics of alkaline HER

As depicted in **Figure 1**, HER in basic solutions may proceed via two pathways, i.e., either Volmer-Tafel or Volmer-Heyrovsky reactions. Accordingly, the conversion of water molecules to hydrogen molecules contains three successive stages, including water adsorption, water dissociation, and hydrogen generation. Generally, three corresponding computational descriptors, water adsorption energy (E_{ad}), the activation energy of water dissociation (E_{ac}), and adsorption-free energy of H* (ΔG_{H*}) are employed to evaluate the ease of a catalyst to initiate the reactions.

ΔG_{H*} is the most frequently documented one among the three parameters, which can illustrate the binding strength of H* on the catalyst surface both in acidic and alkaline media. The hydrogen generation is most feasible if the value of ΔG_{H*} is close to zero, because of the optimal balance between absorption and desorption of hydrogen atoms on the catalyst surface.[8] Nevertheless, the alkaline HER cannot be described merely by ΔG_{H*}.[8, 32] Recently, the E_{ad} and E_{ac} have attracted increasing attention due to their critical roles in the Volmer step of the whole alkaline HER process. For E_{ad}, a lower value indicates a better affinity between the water molecule and catalyst surface, thus facilitating the following reactions. A smaller E_{ac} represents a faster water dissociation process because less activation energy is required. Therefore, a desirable catalyst should possess a low E_{ad}, a minor E_{ac}, and a small absolute value of ΔG_{H*}. To give an example, Yu et al. investigated the catalytic performance of $Ni_{2(1-x)}Mo_{2x}P$,[33] and the computed energetic profiles are presented in **Figure 2**. Firstly, the E_{ad} of ternary NiMoP were lower than those of Ni_2P **(Figure 2a and b)**, especially for the Mo exposed plane (-0.699 eV). Secondly, Mo exposed plane of NiMoP also possesses the lowest E_{ac} over the other selected configurations **(Figure 2c)**. Therefore, the Volmer step on NiMoP surface is more favourable than that on Ni_2P catalyst. Finally, the ΔG_{H*} values also support that Mo exposed NiMoP owns the best hydrogen generation capability due to its lowest $|\Delta G_{H*}|$, thus benefiting the Heyrovsky step **(Figure 2d)**. The E_{ad}, E_{ac}, and ΔG_{H*} of different samples collaboratively suggest that NiMoP manifests better HER performance. It is worth noting that the obtained energies of different active sites/facets on the catalyst surface are important indicators of the underlying mechanisms. Also, they provide valuable guidance for the designing of desirable catalysts.

To gain a better understanding of alkaline HER, comprehensively computational energetics are required. The values of E_{ad}, E_{ac}, and ΔG_{H*} of catalysts are sound indicators of their corresponding properties of water adsorption, water dissociation, and hydrogen generation. For instance, the catalytic activity of Pt in alkaline media is about two orders of magnitude lower than that in acidic solutions because of the sluggish water dissociation process (high E_{ac}).[8] Under this circumstance, the presence of a cocatalyst to effectively cleavage the O-H bonds is highly favourable, such as the layered double hydroxides (LDHs)-based materials.[3] Thus, the Pt-$Ni(OH)_2$ hybrids possess a perfect combination of E_{ad}, E_{ac}, and ΔG_{H*} and exhibits appealing alkaline HER ability. Therefore, the computational energies are handy descriptors in the design of high-performance electrocatalysts.

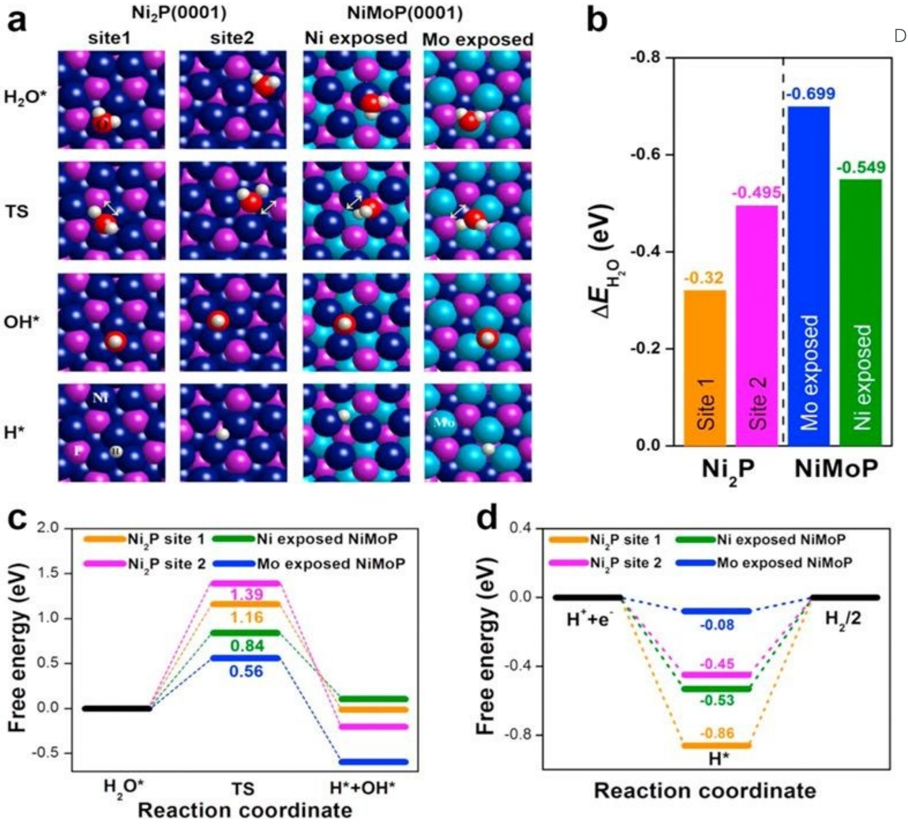

Figure 2. Density functional theory (DFT) calculations. (a) Chemisorption models of H_2O adsorption, OH adsorption, and H adsorption for the calculated free energies over Ni_2P (0001) and NiMoP (0001) terminations. Here TS represents a transition state of H_2O activation. (b) The corresponding adsorption free energy of H_2O, (c) free energy diagram for H_2O activation (cleavage of O-H bonds of H_2O molecules), and (d) free energy diagram for H adsorption (ΔG_H) on the (0001) surfaces of Ni_2P and NiMoP. Reproduced with permission.[33] Copyright 2018, Elsevier Ltd.

2.3 Key parameters for evaluating catalysts in alkaline HER

As reported, many electrocatalytic parameters can be used to assess the overall electrochemical performance of the developed catalysts from different aspects, although it is difficult to compare the performance of different catalysts for alkaline HER.[34] The most frequently reported parameters are the overpotential and Tafel slope, which can offer key information of catalytic activities as well as HER mechanisms.[35] Other valuable parameters are also evaluated including the exchange current density, turnover frequency, Faradaic efficiency, mass and specific activities, and stability. In this part, the aforementioned parameters are briefly introduced and discussed, and more information about these parameters can be referred to a comprehensive review reported by S. Anantharaj et al.[36]

2.3.1 Overpotential

Theoretically, the overall water-splitting processes only require a cell voltage of 1.23V (0 V is for HER and 1.23V for oxygen evolution reaction (OER)). However, due to the reaction hindrances in the real system, both HER and OER require additional potentials to initiate the reactions.[14] The extra potential is called overpotential (η), which is a key parameter to evaluate the activity of catalysts. Typically, the overpotentials at a fixed current density such as 10 mA cm^{-2} (η_{10}) and/or 100 mA cm^{-2} (η_{100}) of different catalysts are compared, and a smaller η represents a better electrocatalytic activity. Commonly, the iR corrected overpotentials are reported, but an actual water electrolysis cell does not run according to iR corrected overpotentials. Hence, it is necessary to report the iR uncompensated data in addition to the iR corrected overpotential to further simulate the real water electrolysis system.[36]

2.3.2 Tafel slope and exchange current density

Tafel slope is one of the primary indicators for evaluating the activity of catalysts, which is beneficial to predict the kinetics of alkaline HER process.[36] It means the rising rates of current density with the increase of overpotential which can be obtained from the Tafel plot. The Tafel plot is derived from the linear sweep voltammetry (LSV) results and recorded with the linear portion at relatively low overpotentials fitted by the Tafel equation ($\eta = a + b \log j$, where η is the overpotential, b is the Tafel slope, and j is the current density).[14] The calculated Tafel slope is in inverse ratio to the charge transfer coefficient, and catalysts with high charge transfer ability favour a small Tafel slope.[37]

View Article Online
DOI: 10.1039/C9TA03220G

Also, the Tafel slope is an indicator of the reaction pathway and RDS. Specifically, the Tafel slopes of the Volmer, Heyrovsky, and Tafel reactions are calculated to be 118.2 mV dec^{-1}, 39.4 mV dec^{-1}, and 29.6 mV dec^{-1}, respectively.[30] For a typical catalyst, Volmer reaction is the rate-determining step when the calculated b is close to 118.2 mV dec^{-1}, and kinetics for adsorption of H atoms onto catalyst surface are sluggish.[38] If the b is around 39.4 mV dec^{-1}, Heyrovsky while the generation of H_2 is principally controlled by desorption process. If b approaches 29.6 mV dec^{-1}, the combination of adsorbed H atoms and the desorption of H_2 will be rate-limiting steps. As a result, it is convenient to judge the hydrogen evolution pathway through the calculated value of the Tafel slope. For example, the Tafel slope of V_8C_7 NMs/GR is about 89.4 mV dec^{-1} which falls within the range of 39.4-118.2 mV dec^{-1}, illustrating the Volmer-Heyrovsky processes.[39] Similarly, the $NiCo_2P_x$ possesses a small Tafel slope of 34.3 mV dec^{-1}, implying a Volmer-Tafel mechanism.[30]

Plotting log ($1/R_{ct}$) *vs.* η (where R_{ct} is the charge transfer resistance) from the electrochemical impedance spectroscopy (EIS) data is another method to obtain the Tafel slope. It is suggested that the latter method can simply reveal the charge transfer kinetics, while Tafel slopes obtained from the former one may include contributions from catalyst and electrode resistance.[40] However, the value of Tafel slope is greatly influenced by the selected experimental parameters (e.g., potential ranges). Tafel slopes over a narrow low-potential range can attain very low values.[34, 37]

When η = 0, the acquired current density from the Tafel equation is named exchange current density (j_0). It can be obtained by extrapolating the linear part of Tafel plots. Normally, j_0 indicates the intrinsic activity of the catalysts under the equilibrium state,

View Article Online
DOI: 10.1039/C9TA03220G

the value is similar to the rate constants employed in the heterogeneously electrocatalytic process.[38] The j_0 is determined by both thermodynamics and kinetics. The intrinsic property of electrocatalysts and experimental conditions (e.g., electrolyte composition and temperature) will also affect the value.[38] Accordingly, a desirable high-performance electrocatalyst possesses a low b and a high j_0. A detailed discussion of Tafel slope and j_0 is presented in a recent review.[36]

2.3.3 Mass and specific activities

The mass and specific activities are quantitative parameters to illustrate the catalytic reactivity of electrocatalysts. The current normalized by the catalyst loading is the mass activity, which is normally expressed in amperes per gram (A/g). The current normalized by the Brunauer-Emmett-Teller (BET) surface area or the electrochemical surface area (ECSA) is the specific activity. As suggested, the BET strategy often leads to a highly inexact result, while ECSA normalized activity has gained more attentions in recent studies.[36] ECSA is considered to disclose the intrinsic surface area of the catalyst exposed to the electrolyte. Hence, the activity calculated by ECSA appears to be more precise. In other words, this method offers an accurate measurement of the catalytic ability of different catalysts with distinguished components, morphology, size, shape, topography and porous structure.[36] In some cases, the double layer capacitance (C_{dl}) of the catalyst is offered in the literature because of its positive correlation with ECSA. A detailed discussion involves mass and specific activities can be found in a previous review.[37]

2.3.4 Turnover frequency

The turnover frequency (TOF) is an important kinetic parameter defined as the number of reactants that can be converted by the catalyst to the desired product per catalytic site per unit of time. Hence, independent of the active surface area, TOF can rigorously reflect the intrinsic activity of active centers on a catalyst.[14, 34] TOF can be obtained from the equation: TOF = $(j \times A)(\alpha \times F \times n)^{-1}$, where j is the current density at a given overpotential, A is the surface area of the working electrode, α is the electron transfer number at a given overpotential, F is the Faraday constant, and n is the number of moles of coated metal atoms on the electrode. It should be mentioned that not all the atoms in the catalyst deliver catalytic activities and can be equally accessible. Nevertheless, the calculated TOF is still a handy tool for comparing the activities of similar catalysts.

2.3.5 Faradaic efficiency

Faraday efficiency (FE) is used to quantify the number of electrons that are engaged in the target reactions instead of the side reactions. It is the ratio of the quantity of experimentally produced H_2 to the theoretical calculated H_2 amount in HER. The amount of the product (H_2) can be measured by gas chromatography (GC) or the water displacement method. Normally, the reported FE in HER are close to 100%, and a higher FE represents a better selectivity for the alkaline HER process.

2.3.6 Stability

Apart from those aforementioned parameters that focus on the activity of catalysts, stability is another vital issue which can determine the feasibility of an electrocatalyst in practical applications. There are two popular methods to evaluate the long-term durability of catalysts. One is to record the chronopotentiometry curves or chronoamperometry curves at constant current densities in a long operation (>12 h). The decrease of the current density at a fixed potential or the rise of the overpotential at a fixed current density (commonly 10 mA cm^{-2}) can reveal the durability of the catalysts.

View Article Online
DOI: 10.1039/C9TA03220G

The less variation of current density or the overpotential marks better longevity. Another method is the accelerated degradation test, which records and compares the cyclic voltammetry (CV) curves or LSV curves before and after thousands of cycles. The shift of the onset overpotential and the overpotential at a constant current density indicates the durability of the catalyst. The smaller shift, the better the stability.

3. Transition metal-based electrocatalysts for hydrogen evolution in alkaline media

Transition metals have significantly contributed to the development of advanced electrocatalysts because of their high abundance, impressive activities, and easy accessibility. Lately, researchers perform intensive and extensive studies on the design and application of TM-based catalysts for alkaline HER. To our delight, grand progress on both catalyst synthesis and mechanism explorations rapidly push the boundary of the field to a high level. **Table1** lists the key information (e.g., main catalytic performance and applied strategies) of typical catalysts that discussed in this review, some of which are comparable to the PGMs-based catalysts. Obviously, part of these TM-catalysts are promising alternatives to the noble-based materials and provide new concepts to design cost-efficient electrocatalysts for alkaline HER. Notably, TMs, TM alloys, and TMXs (X= O, S, Se, N, P, C, and B) all exhibit outstanding catalytic activities, while the design principles and underlying mechanisms are different. In this section, the recent achievements of TM-based catalysts will be showcased and classified by the anionic elements.

Table 1 TM-based electrocatalysts for alkaline HER.

View Article Online
DOI: 10.1039/C9TA03220G

Category	Electrocatalyst	Key strategy	Electrolyte	η_{10}/ mV	Tafel slope/ mV dec^{-1}
TMs	Ni-rGO/Ni foam[41]	Hybridization	1 M NaOH	36	77
	N,P-doped Ni[42]	Co-doping	1 M KOH	24	34
	Mn-doped *hcp* Ni[43]	Phase engineering, Doping	1 M KOH	80	68
	W-SAC[44]	Single-Atom catalysis	0.1 M KOH	85	53
	Ru-NC-700[45]	Single-Atom catalysis	0.1 M KOH	47	14
TM alloys	Ni_3Fe@N-C NT/NFs[2]	Hybridization; Hierarchical structure	1 M KOH	72	98
	RuCo@NC[46]	Hybridization	1 M KOH	28	31
TMOs	Ni_3S_2/VO_2 CSN[47]	Hybridization	1 M KOH	100	114
	Ni_5P_4@$NiCo_2O_4$[48]	Hybridization	1 M KOH	27	27
	$NiCo_2O_4$ nanosheet[49]	Facet engineering	1 M KOH	105	62.1
	Reduced $NiCo_2O_4$[50]	Defect engineering	1 M KOH	135	52
	NiCo/Ar-EA[51]	Defect engineering	1 M KOH	317 (η_{360})	132
	Fe-$NiCo_2O_4$@HNCP[52]	Doping	1 M KOH	124	47
	P-doped β-$CoMoO_4$[53]	Doping	1 M KOH	138	68.74
	$Co_2Mo_3O_8$/Co/NF[54]	Hybridization; Hierarchical structure	1 M KOH	50	49
TMOHs	β-$Ni(OH)_2$/Pt[55]	Hybridization	0.1 M KOH	92	42
	NiFeRu-LDH[56]	Doping	1 M KOH	29	31
	MoS_2/NiCo-LDH[57]	Hybridization	1 M KOH	78	76.6
TMSs	N-doped Ni_3S_2/NF[58]	Doping	1 M KOH	155	113
	N-doped Ni_3S_2/VS_2[59]	Doping	1 M KOH	151	107.5
	Sn-Ni_3S_2/NF[60]	Doping	1 M KOH	170 (η_{100})	55.6
	$Fe_{17.5\%}$-Ni_3S_2/NF[61]	Doping	1 M KOH	47	95

View Article Online
DOI: 10.1039/C9TA03220G

	Co_3S_4 PNS_{vac}[62]	Defect engineering	1 M KOH	63	58
	CoMoS[63]	Defect engineering	1 M KOH	98	82
	Cu NDs/Ni_3S_2 NTs-CFs[32]	Hybridization	1 M KOH	128	76.2
	$NiCo_2S_4/Ni_3S_2$/NF[64]	Hybridization	1 M KOH	119	105.2
TMSes	Co-WSe_2/MWNTs[65]	Doping	1 M KOH	241	-
	Ni-$MoSe_2$[66]	Doping	1 M KOH	206	81
	N-$NiSe_2$[67]	Doping	1 M KOH	86	69
	P-$CoSe_2$[68]	Doping	1 M KOH	92	90
	$CoSe_2$-$MoSe_2$/G[69]	Hybridization	1 M KOH	198	79
	$NiCoSe_2$/CC[70]	Component optimization	1 M KOH	112.7	65
	$CoNiSe_2$@CoNi-LDHs/NF[71]	Hybridization	1 M KOH	106	74
	$MoSe_2$-$CoSe_2$[72]	Hybridization	1 M KOH	127 (η_0)	89
	c-$CoSe_2$[73]	Phase engineering	1 M KOH	190	85
	o-$CoSe_2$|P[74]	Phase engineering; Doping	1 M KOH	104	69
	Ni_3Se_2/NiSe[75]	Phase engineering	1 M KOH	168 (η_{100})	72.1
TMTes	$Co_{1.11}Te_2$/C[76]	Component optimization	1 M KOH	178	77.3
TMNs	Mo_5N_6[77]	Component optimization	1 M KOH	94	66
	Ni_3N@CQDs[78]	Hybridization	1 M KOH	69	108
	Ni_3N/Ni[79]	Hybridization	1 M KOH	12	29.3
	NC-NiCu-NiCuN[80]	Hybridization	1 M KOH	93	55
	Ni_3N-CeO_2/TM[81]	Hybridization	1 M KOH	80	122
TMPs	$Ni_{90}P_{10}$/Ti[82]	Component optimization	1 M KOH	125	55.7
	$Ni_{0.67}Co_{1.33}P$/N-C NFs[83]	Component optimization	1 M KOH	130	70
	$Ni_{1.8}Cu_{0.2}$-P/NF[84]	Doping	1 M KOH	78	70
	O-$NiMoP_2$/Ni[85]	Doping	1 M KOH	31	62.11
	N-Co_2P/CC[86]	Doping	1 M KOH	34	51

	O,Cu-CoP[87]	Co-doping	1 M KOH	72	57.6
	Ni@Ni_2P-Ru[88]	Hybridization	1 M KOH	31	41
	FeP/Ni_2P[89]	Hybridization	1 M KOH	14	24.2
TMCs	Mo_2C/G3-NCS750[25]	Porous structure; Doping	1 M KOH	66	37
	N,P-Mo_xC NF[90]	Co-doping; Hybridization	1 M KOH	135	57.1
	Mo_2N-Mo_2C/HGr-3[91]	Hybridization	1 M KOH	154	68
	CoP/Mo_2C-NC[92]	Hybridization	1 M KOH	67.2	66
	Mo/Mo_2C-HNS-750[93]	Hybridization	1 M KOH	79	62.86
TMBs	Ni_xB/f-MWCNT[94]	Porous structure; Hybridization	1 M KOH	116	70.4
	Co-B/Ni[95]	Porous structure	1 M KOH	70	68

3.1 Transition metals

Due to the promising electrocatalytic activities and durability, transition metals have been widely employed in electrocatalysis, especially HER in basic solutions. To date, earth-abundant TMs (Ni, Co, W, Fe, etc.) have exhibited excellent performance for HER. Ni is the most intensively researched TM and miscellaneous approaches have been engaged to achieve the desirable Ni-based electrocatalysts. For example, diverse Ni-carbon (reduced graphene oxide (rGO),[41] carbon quantum dot,[96] carbon nanotube[97]) composites were fabricated act as high-performance catalysts for alkaline HER. These sophisticated hybrids take advantage of the intrinsic activity of Ni and the features of carbon materials with good conductivity, large surface area, easy surface functionalization, and high stability.[96] Take Ni-rGO as an example, Wang et al. applied supergravity electrodeposition to construct the Ni-rGO/NF catalyst. The catalyst showed great electrocatalytic activities with a low Tafel slope (77 mV dec^{-1}), a small overpotential (η_{10} =36 mV), as well as a high exchange current density (j_0 = 3.408 mA cm^{-2}).[41] The excellent performance derives from the large specific surface area, improved electrical conductivity, and synergistic effect between Ni particles and rGO sheets. Additionally, DFT calculations suggest that Ni-rGO possessed superior interfacial activities in adsorption/desorption of H* than the pure Ni and rGO sheet.

Doping transition metals with heteroatoms arises as an efficient strategy to boost the catalytic performance, because doping can regulate the electronic structure of the host metals by tailoring the local charge redistribution without changing the desired intrinsic features of the host elements.[42] Very recently, Jin et al. found that the nitrogen and phosphorus dual-doped Ni exhibited better electrocatalytic activities than the pure nickel, nickel compounds (Ni_3N, Ni_2P), as well as other doped Ni samples (N-Ni, P-Ni, S-Ni, S-N-Ni, S-P-Ni), with η_{10} =24 mV in alkaline HER.[42] Experimental results and DFT calculations indicated that the alien atoms could induce charge redistribution on the Ni surface and manipulate the electronic structure of Ni metal in catalysis. In addition, chronoamperometry tests, spectroscopic and TEM measurements suggested that the N-P-Ni was quite stable under the operating condition. This doping scheme was also applicable to Co metal catalysts, thus providing a new strategy for activating transition metal catalysts.

It is suggested that the exposed crystal phase of metal crystals has a dominant impact on their performance because of the variations in packing density, reactivity, and durability. Shao et al. compared the electrocatalytic properties of hexagonal-close-packed (*hcp*) Ni,[43] face-centered cubic (*fcc*) Ni, and Mn-doped *hcp* Ni. The experimental results disclosed that the *hcp* Ni owned a higher HER activity than the *fcc* Ni, and the introduction of Mn further improved the catalytic activity of *hcp* Ni (**Figure 3a-d**).

View Article Online
DOI: 10.1039/C9TA03220G

Surprisingly, the Mn-doped *hcp* Ni exhibited the lowest overpotential (η_{10} =80 mV) and Tafel slope (68 mV dec^{-1}), the highest TOF (0.53 H_2 s^{-1}@ η=100 mV), as well as the best stability. Further study indicated that the Mn-*hcp* Ni possessed a higher *d*-band center and a lower water dissociation energy (**Figure 3e-f**). As a result, the formed MnO/*hcp* Ni surface remarkably boosted the HER activity through favourable water adsorption and fast water dissociation.

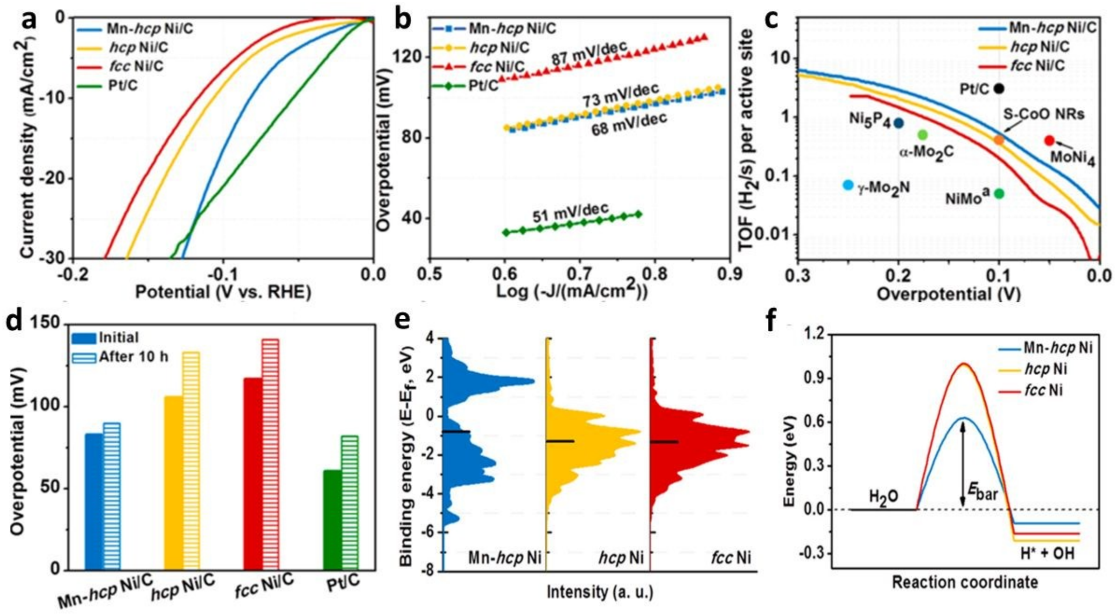

Figure 3. (a) HER polarization plots and (b) the Tafel slopes of Mn-*hcp* Ni/C, *hcp* Ni/C, *fcc* Ni/C, and Pt/C. (c) TOF plots of Mn-*hcp* Ni/C, *hcp* Ni/C, and *fcc* Ni/C against overpotential and TOF values of the commercial Pt/C and the reported electrocatalysts at specific overpotentials. (d) The comparison of overpotentials at 10 mA cm^{-2} before and after 10 h chronopotentiometry tests of Mn-*hcp* Ni/C, *hcp* Ni/C, *fcc* Ni/C, and Pt/C. (e) Surface valence band photoemission spectra of Mn-*hcp* Ni, *hcp* Ni, and *fcc* Ni. The black lines point to the locations of *d*-band center. (f) Calculated energy diagram of water dissociation on the three metal slabs. Reproduced with permission.[43] Copyright 2018, American Chemical Society.

Lately, single atom catalysts (SACs) have attracted enormous attention because of their unique catalytic activities and selectivity, as well as high atomic utilization. SACs are defined as catalysts that contain singly isolated metal atoms anchored on substrates without appreciable interactions with other similar atomically dispersed metal atoms.[45,

[98] For example, Chen et al. anchored single W atoms in N-doped carbon matrix from metal-organic framework (MOF) for alkaline HER.[44] The obtained catalysts exhibited a low η_{10} of 85 mV, a low Tafel slope of 53 mV dec^{-1} and an extremely high TOF of 6.35 H_2 s^{-1} (η=120 mV). A computational study revealed that the $W_1N_1C_3$ moiety owned a low Gibbs free energy of hydrogen adsorption (ΔG_{H*}) of 0.033 eV, which demonstrated that the $W_1N_1C_3$ moiety played a crucial role in improving the HER activity. Additionally, the unique structure of $W_1N_1C_3$ moiety possesses high stability, because of the strong interaction between the W atoms and the carbon support. In similar research, Lu and co-workers found that the RuC_xN_y moieties in the Ru and N co-doped carbon materials was the primary active sites in the alkaline HER, while the Ru nanoparticles played a less significant role.[45] The Ru atoms and C atoms adjacent to the Ru centers possible served as the catalytic centres for the outstanding HER performance. These atomically dispersed metals possess great potential for catalyzing water splitting in alkaline solutions. Currently, the fabrication process of single atom catalysts is still the main obstacle that hinders their wide applications. In this regard, many efficient methods have been developed to fabricate SACs, such as the mass-selected soft-landing technique and the wet-chemistry method.[98]

3.2 Transition metal alloys

Alloying is claimed as a sagacious way to upgrade the catalytic activity and longevity of TMs.[99, 100] TM alloying can raise the electrocatalytic efficiency by a synergistic combination of electrocatalytic metals or enlarging the ratios of the real and the geometric surface areas.[100] Currently, Ni-based alloys are the most reported TM alloys because of their high catalytic performance in alkaline HER and low price. For instance, Li et al. applied the electrospinning strategy to construct a 1D hierarchical nanoarchitecture comprising Ni_3Fe nanoalloy-encapsulated carbon nanotubes grown onto N-doped carbon nanofibers (Ni_3Fe@N-C NT/NFs).[2] The immobilized Ni_3Fe nanoparticles worked as catalytic sites and the N-doped carbon nanostructures facilitated the electron transport and mass diffusion. Moreover, the Ni_3Fe nanoalloys encapsulated in carbon nanotubes could remarkably optimize the electron structure of the surrounding carbons because of the electron-penetration effect, thus elevating the electrocatalytic activity. Compared with Ni-based and Fe_2O_3-based catalysts, i.e., Ni@N-C NT/NFs and Fe_2O_3@N-CNFs, Ni_3Fe@N-C NT/NFs possessed the lowest η_{10} of 72 mV, the lowest Tafel slope of 98 mV dec^{-1}, as well as the highest ECSA of 407.5 cm^{-2}. Additionally, the computational results revealed that the Ni_3Fe@N-C NT/NFs attained a favourable ΔG_{H*} of -0.14 eV, thus promoting the HER kinetics. Similarly, Ni-Cu alloys,[6, 101] Ni-Mo alloys,[102-104] and Co-based alloys[46, 105] also exhibited decent catalytic capabilities for alkaline HER.

Apart from those earth abundant TMs, noble metal-based alloys have enticed intensive attention recently due to their distinctive catalytic behaviors. Alloying noble metals with other TMs (e.g., Ni, Fe, Co) to obtain the multicomponent electrocatalysts is a smart strategy to increase the atomic utilization efficiency of noble metals and decrease the consumption of noble metals by up to an order of magnitude.[46, 106] More importantly, noble-transition alloys significantly enhance catalytic capability because of the redistribution of charge and tailored surface properties during the formation process of alloys.[46, 107] Lately, Ru, a noble metal cheaper than Pt, Pd, and Ir, evoking intense excitement to the researchers for its high catalytic activities for HER and relatively low price. For example, Su and co-workers developed a high-performance electrocatalyst composed of Ru-Co nanoalloy encapsulated in nitrogen-doped graphene layers.[46] The

View Article Online
DOI: 10.1039/C9TA03220G

synthetic route is presented in **Figure 4a**. The FESEM results indicated that the obtained catalysts possessed an irregular morphology **(Figure 4b)**. TEM and high-resolution TEM images showed that the alloy particles were coated with thin N-doped graphene shells which were beneficial to enhancing the catalytic activity **(Figure 4c-f)**. The sample S4 (3.58 wt. % Ru in RuCo alloy) exhibited the best HER ability in 1 M KOH compared to other samples with different Ru contents. Specifically, S4 owned the smallest overpotential (η_{10} =28 mV) and Tafel slope (31 mV dec^{-1}), as well as the best durability (**Figure 4g-i**), which is better than the benchmark Pt/C (20 wt.%) catalysts. In addition, the results of the etching test indicated that the metallic Co played an indispensable role in the outstanding HER performance in alkaline media **(Figure 4j)**. Further computational results suggested that the number of electrons transferred from the alloy core to the graphene shell was higher than that of the metal core, which implied lower ΔG_{H*} and thus better catalytic activities (**Figure 4k** and **l**). Furthermore, the frequently documented Pt-based alloys also present appealing catalytic capability for alkaline HER.[106, 108-111] These results declared that alloying noble metals with TMs are an effective and economic strategy for fabricating high-performance HER electrocatalysts with a lower cost.

View Article Online
DOI: 10.1039/C9TA03220G

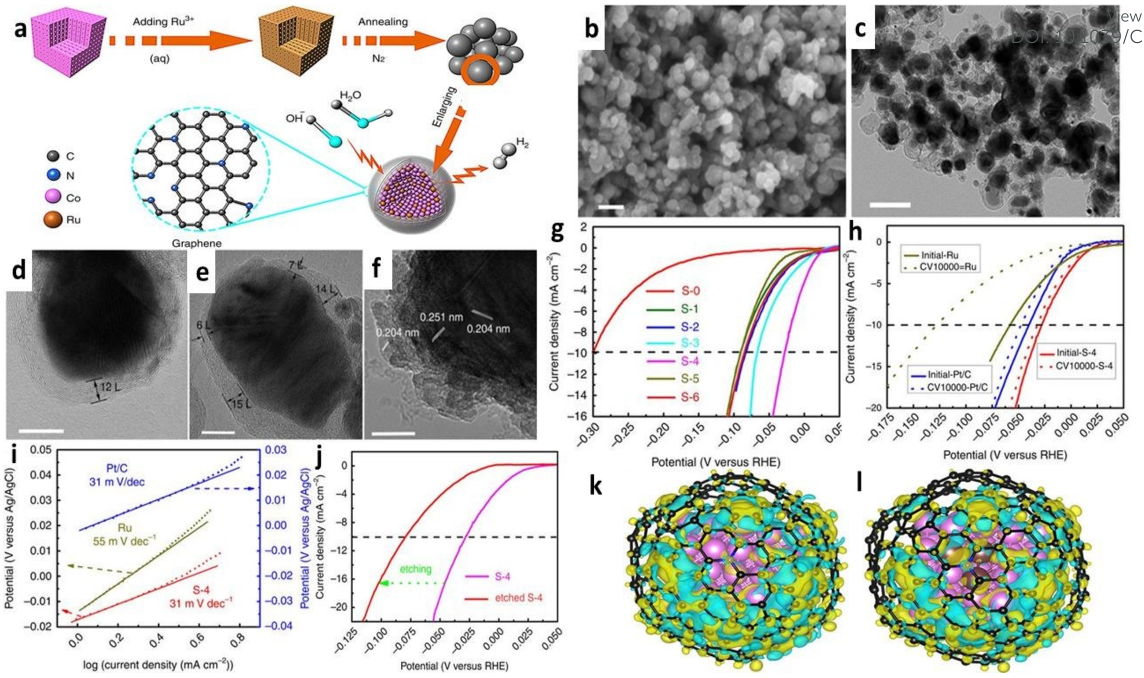

Figure 4. (a) Schematic illustration of the synthetic route and model of the RuCo nanoalloys encapsulated in nitrogen-doped graphene layers. (b, c) The FESEM and TEM images of S-4. Scale bars, 100 nm. (d-f) HRTEM images of S-4. Scale bars, 10 nm. (g) HER polarization curves of RuCo@NC samples with the same mass loading. (h) HER polarization curves of S-4, Ru and Pt/C with the same mass loading and durability test after 10,000th cycles. (i) Tafel plots of S-4, Ru and Pt/C. (j) HER polarization curve of etched S-4 by 1M HCl. (k, l) Calculated charge-density differences between Co and Co_3Ru models, respectively. The isosurface value of the color region is 0.01 eÅ^{-3}. The yellow and cyan regions refer to increased and decreased charge distributions, respectively. Reproduced with permission.[46] Copyright 2018, Nature Publishing Group.

The electrochemical stability of catalysts is a key criterion that determines the practicability of a designed electrocatalyst in industrial applications. The oxidation and corrosion of TM alloys has been a concern in the alkaline HER process, whilst a vast number of the TM electrocatalysts have been reported to deliver a great stability. Apart from the conventional chronopotentiometry and chronoamperometry methods introduced before, other techniques are also applied to evaluating the durability of catalysts, including X-ray diffraction (XRD), X-ray photoelectron spectra (XPS), transmission electron microscopy (TEM), scanning electron microscopy (SEM), and Fourier-transform infrared spectroscopy (FTIR).[102, 112-117] These tests along with the electrochemical measurements can provide comprehensive information (e.g., catalytic

View Article Online
DOI: 10.1039/C9TA03220G

activities, components, morphology, surface properties) of the materials before and after durability testing. For example, Ahn et al. investigated the stability of Ni-Co-Fe alloys derived from the Prussian blue analog.[112] Firstly, chronopotentiometry tests were conducted and the catalysts showed an initial HER potential of -0.34V vs. RHE, and a voltage loss of merely 0.05V after 20000s. Then, TEM characterization was further performed to verify the structural durability of the ternary alloy. The main nanocuboid morphology was maintained during the HER tests, although the edges were slightly roughened because of the formation of metal hydroxides. The favourable electrochemical stability is mainly due to the particularly rigid porous structure of the robust MOF, and the unique architecture facilitates the gas bubbling and retains the framework.

3.3 Oxygen group transition metal catalysts

3.3.1 Transition metal oxides

Electrocatalysts based on transition metal oxides (TMOs) have gained enormous interests due to their low toxicity, earth-abundance, low cost, and high activities.[118] Previously, pure TMOs exhibit superb potentials for OER yet poor reactivity toward HER because of their unappealing hydrogen desorption ability.[118, 119] Encouragingly, great efforts have been made to shape TMOs into appropriate catalysts for alkaline HER, affording the engineered TMOs good candidates for overall water splitting.

Hitherto, CoO_x,[119-121] VO_2,[47] MnO_2,[21, 122] and NiO,[118, 123] are representatives that possess high catalytic performance after modifications. Hybridizing TMOs with other electroactive materials (e.g., TMOs,[124-126] TMPs,[48, 127] TMs,[123, 128, 129] TM alloys,[130, 131] TMSs[132, 133]) is an advisable approach to improve the catalytic performance of bare TMOs. Take VO_2 as an example, compositing VO_2 with Ni_3S_2 could yield an appealing hybrid for overall water splitting, which only took a low potential of 1.42 V to attain a current density of 10 mA cm^{-2}.[47] The astonishing catalytic activity originated from the interfaces which gave rise to a low-energy-level *d* band center and a low Gibbs free energy. Lately, Zhang and Co-workers constructed nanometric Ni_5P_4 clusters on $NiCo_2O_4$ via a phosphating process.[48] The Ni_5P_4@$NiCo_2O_4$ exhibited superior catalytic performance than Ni_5P_4 and $NiCo_2O_4$, with a low Tafel slope of 27 mV dec^{-1} and an overpotential of 27 mV at 10 mA cm^{-2}. DFT calculations implied that $NiCo_2O_4$ significantly improved the water dissociation step, and Ni_5P_4 facilitated the hydrogen adsorption and desorption process. Addditionally, the presence of Ni_5P_4 promoted the electron transfer within the $NiCo_2O_4$ nanoflakes, which further ameliorated the overall electrochemical reactivity. The hybridization of Ni_5P_4 and $NiCo_2O_4$ thus delivered an excellent HER activity in alkaline electrolytes.

Bimetallic oxides of $M_1M_2O_x$ (M_1, M_2: transition metal) also manifest great potentials for alkaline HER. In the following part, we mainly focus on the application of two series of typical oxides, i.e., spinel TMOs and $MMoO_4$. Spinel bimetallic TMOs (e.g., $NiCo_2O_4$) have a more flexible redox property, and higher conductivity than the corresponding individual metal oxides, herein manifesting a better catalytic activity in electrochemistry.[48] However, the electrocatalytic ability of such pristine TMOs in HER is still unsatisfactory. To break the bottleneck, several approaches have been developed, including doping,[52, 134, 135] defect (oxygen vacancy) engineering,[50, 51] crystal-plane engineering,[49] compositing[48, 124, 126, 136] and hierarchical structuring.[137] Recently, Fang et al. fabricated $NiCo_2O_4$ nanocrystals exposing various crystal planes, including $NiCo_2O_4$ nanosheet exposing (1 1 0) crystal planes,[49] $NiCo_2O_4$ octahedron exposing (1 1 1) crystal planes and $NiCo_2O_4$ truncated octahedron exposing (1 1 1) and (1 0 0) crystal planes

(**Figure 5a-g**). The experimental results suggested that $NiCo_2O_4$ nanosheets exhibited the best catalytic activity for alkaline HER, followed by $NiCo_2O_4$ octahedron and $NiCo_2O_4$ truncated octahedron (**Figure 5h** and **i**). Moreover, density functional theory (DFT) calculations revealed that the (1 1 0) crystal planes have the lowest ΔG_{H*} of 0.15 eV relative to (1 0 0) (0.62 eV) and (1 1 1) (0.36 eV) planes, implying that the (1 1 0) surface was more active than (1 0 0) and (1 1 1) planes for HER (**Figure 5j**). These fruitful findings disclose that selectively exposing favourable grain boundaries of electrocatalysts the can achieve high activities in HER.

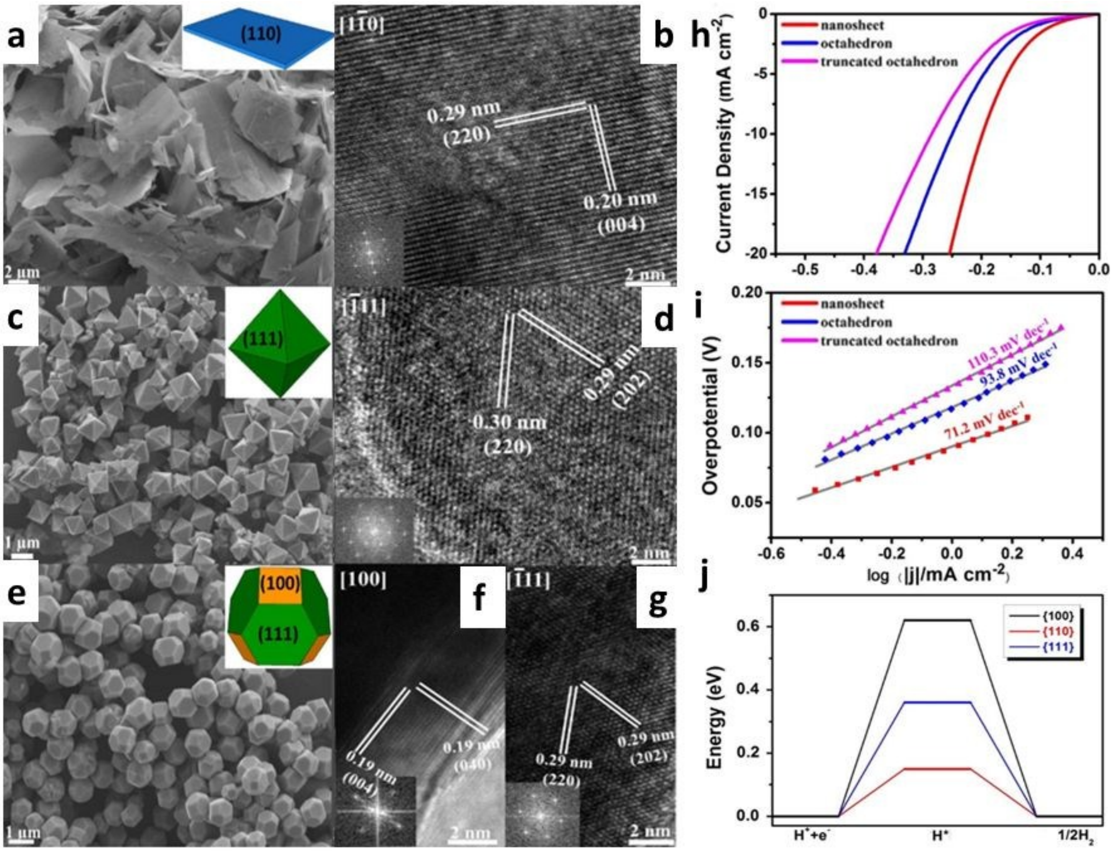

Figure 5. (a- b) The SEM and HRTEM images of the $NiCo_2O_4$ nanosheet exposing (1 1 0) crystal planes. (c- d) The SEM and HRTEM images of $NiCo_2O_4$ octahedron exposing (1 1 1) crystal planes. (e- g) The SEM and HRTEM images of $NiCo_2O_4$ truncated octahedron exposing (1 1 1) and (1 0 0) crystal planes. (h) Polarization curves and (i) the corresponding Tafel slopes of the $NiCo_2O_4$ nanosheet, $NiCo_2O_4$ octahedron, $NiCo_2O_4$ truncated octahedron. (j) The HER free energy change diagram of $NiCo_2O_4$ (1 0 0), (1 1 0) and (1 1 1) crystal planes. Inset images in (a, c, e) are the models of crystals. Inset

images in (b, d, f, g) are the corresponding fast Fourier transform patterns. Reproduced with permission.[49] Copyright 2018, Elsevier Ltd.

Oxygen vacancy engineering is another efficient method to simultaneously modulate the electronic structure, conductivity, and the reactive species' adsorption energy.[50, 51, 118] As a result, the presence of oxygen vacancies can profoundly boost intrinsic catalytic activities. Lately, Feng et al. developed an "adsorption-calcination-reduction" strategy to fabricate a series of spinel TMOs ($NiCo_2O_4$, $CoMn_2O_4$, and $NiMn_2O_4$) (**Figure 6a**).[50] The XAFS analysis revealed the existence of abundant oxygen vacancies in the reduced $NiCo_2O_4$, leading to the decline in Co coordination numbers (**Figure 6b** and **c**). Compared to unmodified $NiCo_2O_4$, the reduced sample possessed a lower overpotential (135 vs. 236 mV, η_{10}) and a smaller Tafel slope (52 vs. 95 mV dec^{-1}). Furthermore, the projected density of states (PDOS) of Co *d* orbital in the reduced $NiCo_2O_4$ shifted to the low-energy direction. This leftward shift indicated that the distribution of electrons in the *d* band drifted away from the Fermi level (**Figure 6d**), indicating that the catalyst attained weakened chemical bonding with intermediates with lower adsorption energy. These findings were further verified by the calculated ΔG_{H*} (**Figure 6e**). In another study, Liu et al. found that the oxygen vacancy content had a prominent effect on the catalytic capability of $NiCo_2O_4$.[51] Specifically, increasing the oxygen vacancy concentration would decrease the adsorption energy and the dissociation energy barrier of H_2O molecules on catalyst surfaces, thus improving the catalytic ability in alkaline HER.

Doping is a conventional strategy to upgrade the activity of catalysts by increasing active sites, optimizing the electronic structure, inducing phase transformation, and regulating reaction energy barrier, etc. Very recently, Lai et al. investigated the catalytic performance of TM-doped $NiCo_2O_4$ (TM= Fe, Co, Ni, Zn, Mn, Cu),[52] and the preparation

View Article Online
DOI: 10.1039/C9TA03220G

route is depicted in **Figure 6f**. The alkaline HER activity of Fe-doped $NiCo_2O_4$ was higher than that of pristine $NiCo_2O_4$, with a low η_{10} of 124 mV and a small Tafel slope of 47 mV dec^{-1} (**Figure 6g** and **h**), as well as a high TOF value of 0.39 s^{-1} at an overpotential of 200 mV. The DFT analysis indicated that the electrons transferred from the N-doped carbon polyhedron (HNCP) to the partially charge-delocalized Fe-$NiCo_2O_4$, which increased the electronic states near the Fermi level of Fe/Co/Ni *d* orbitals (**Figure 6i** and **j**). This charge transfer process improves the overall properties of catalysts. Compared with $NiCo_2O_4$@HNCP, the obtained energy barriers of Fe-doped $NiCo_2O_4$@HNCP revealed the improved thermodynamic and kinetic performance **(Figure 6k)**. Moreover, Cu, Mn, and Zn doped $NiCo_2O_4$ also exhibited higher catalytic activities than the pristine one.

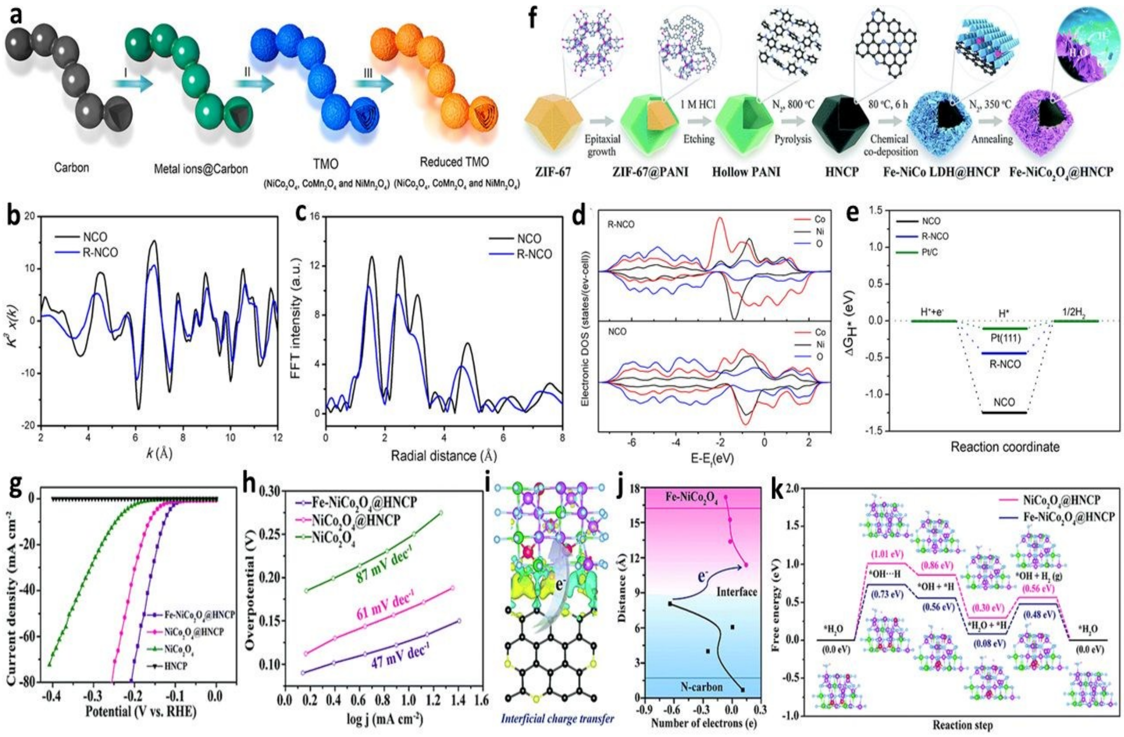

Figure 6. (a) Schematic illustration of the formation process of R-TMO with a necklace-like multishelled hollow structure: (I) The absorption of metal ions on the carbon, (II) calcination of the absorbed carbon, and (III) reduction of the TMO to obtain R-TMO with a necklace-like multishelled hollow structure. (b) Co K-edge EXAFS data. (c) The corresponding k^3-weighted Fourier-transformed data of pristine $NiCo_2O_4$ and R-

$NiCo_2O_4$. (d) Calculated DOS curves for pristine $NiCo_2O_4$ and R-$NiCo_2O_4$. (e) Calculated free energy diagram of the HER on pristine $NiCo_2O_4$ and R-$NiCo_2O_4$. (a- e). Reproduced with permission.[50] Copyright 2018, American Chemical Society. (f) Schematic illustration of the synthesis process of Fe-$NiCo_2O_4$@HNCP. (g) Polarization curves and (h) Tafel curves of Fe-$NiCo_2O_4$@HNCP and the compared samples in 1.0 M KOH solution for HER with a scan rate of 5 mV s^{-1}. (i) Charge density distribution of Fe-$NiCo_2O_4$@HNCP around the interface. (j) Bader charge analysis of average atoms near the interface of N-carbon and Fe-$NiCo_2O_4$. (k) Calculated free energy diagram of HER on Fe-$NiCo_2O_4$, and $NiCo_2O_4$. (f- k). Reproduced with permission.[52] Copyright 2019, The Royal Society of Chemistry.

Mo-based materials are promising HER catalysts among which transition metal molybdates ($MMoO_4$) have been demonstrated as efficient electrocatalysts for alkaline HER due to their high activities and adjustable electronic structures by the synergy of Mo and M.[54] Lately, Li and co-workers investigated the catalytic properties of P-doped β-$CoMoO_4$ prepared by a two-step strategy **(Figure 7a)**.[53] The doped sample showed a better performance than β-$CoMoO_4$ and Co-Mo-O, with a small overpotential (η_{10} = 138 mV) and a low Tafel slope (68.76 mV dec^{-1}) (**Figure 7b** and **c**). The density of states (DOS) of different samples indicated that the P doping narrowed the bandgap of β-$CoMoO_4$ from 2.09 eV to 1.87 eV, introduced more charge carriers and ameliorated the electrical conductivity **(Figure 7d)**. Furthermore, DFT results indicated that P-doped β-$CoMoO_4$ owned a similar energy barrier in the Volmer step ($\Delta G(H_2O)$ = 0.45 eV) to pure β-$CoMoO_4$ ($\Delta G(H_2O)$ = 0.41 eV), while the ΔG_{H*} of the P-doped $CoMoO_4$ was quite lower than the pristine one (0.41 eV vs. 0.76 eV) (**Figure 7e** and **f**). Hence, the optimized electrical conductivity and hydrogen adsorption free energy resulted in the improved catalytic activity. Interestingly, Ou et al. used $CoMoO_4{\bullet}0.9H_2O$ as a precursor to produce $Co_2Mo_3O_8$ **(Figure 7g)**.[54] The prepared hierarchical structures are composed of internal Co nanowires and $Co_2Mo_3O_8$ outer layers **(Figure 7h)**. Compared with the pristine $CoMoO_4{\bullet}0.9H_2O$, $Co_2Mo_3O_8$ demonstrated a better catalytic activity (**Figure 7i** and **j**). Furthermore, the authors declared that the bimetallic suboxides with lower-valence Mo

View Article Online
DOI: 10.1039/C9TA03220G

species (Mo^{4+}, Mo^{5+}) facilitated the water adsorption and intermediate formation processes. This approach may be beneficial to the design of desirable electrocatalysts of bimetallic suboxides reduced from the corresponding oxide precursors.

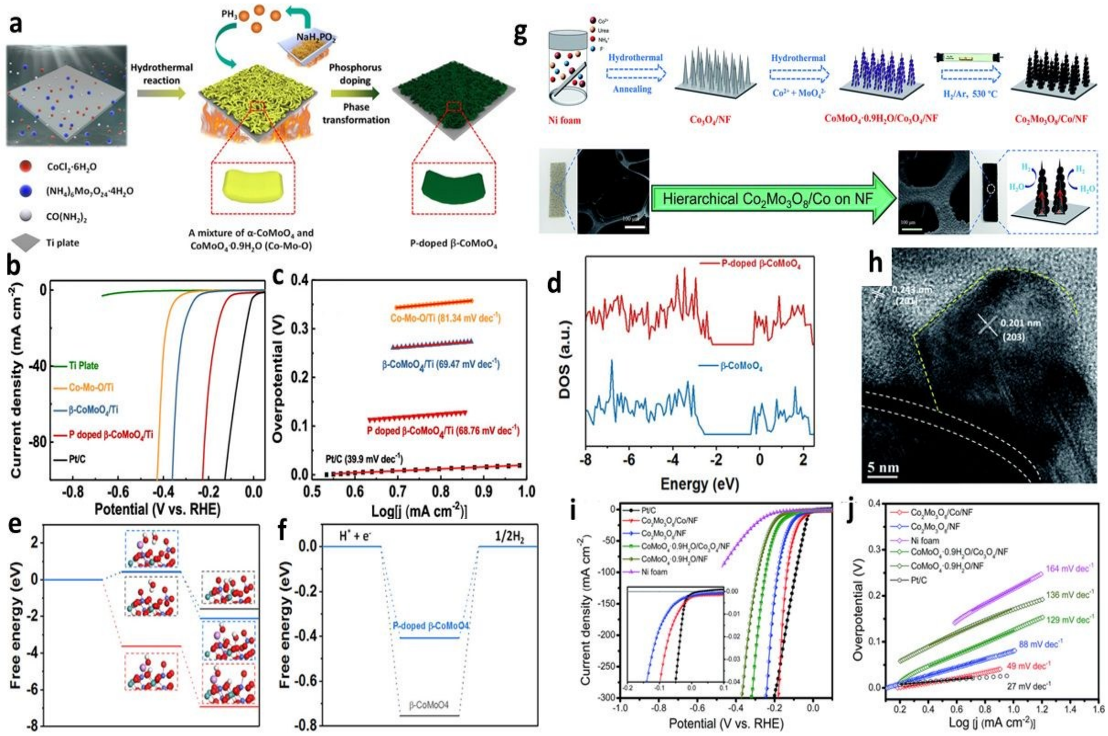

Figure 7. (a) Schematic illustration of the synthesis route of P-doped β-$CoMoO_4$ on a Ti plate. (b) Linear sweep voltammetry (LSV) polarization curves of Ti plate, Co-Mo-O/Ti, β-$CoMoO_4$/Ti, P-doped β-$CoMoO_4$/Ti, and Pt/C. (c) Tafel plots for Co-Mo-O/Ti, β-$CoMoO_4$/Ti, P-doped β-$CoMoO_4$/Ti, and Pt/C. (d) Total density of states of β-$CoMoO_4$ and P-doped β-$CoMoO_4$. The Fermi level is set at 0 eV. (e) Calculated free energy diagram for the Volmer step on the original P-doped β-$CoMoO_4$ model (red line), revised P-doped β-$CoMoO_4$ model (grey line), and β-$CoMoO_4$ model (blue line). (f) Calculated free energy diagram for the Tafel step. (a- f). Reproduced with permission.[53] Copyright 2018, American Chemical Society. (g) Schematic illustration of the process for fabricating the $CoMoO_4$•$0.9H_2O/Co_3O_4$ composite on Ni foam and reducing it to $Co_2Mo_3O_8$/Co/NF under a H_2/Ar atmosphere. (h) The HRTEM image of $Co_2Mo_3O_8$/Co. The white dash shows the outline of the tip region of a Co nanowire and the yellow dash shows the outline of a $Co_2Mo_3O_8$ nanosheet. (i) LSV curves and (j) Tafel plots of $Co_2Mo_3O_8$/Co/NF, $Co_2Mo_3O_8$/NF, $CoMoO_4$•$0.9H_2O/Co_3O_4$/NF, $Co_2Mo_3O_8$/NF, Ni foam, and Pt/C. (g- j). Reproduced with permission.[54] Copyright 2018, The Royal Society of Chemistry.

3.3.2 Transition metal (oxy)hydroxides

Transition metal (oxy)hydroxides (TMOHs), including the special class of layered double hydroxide (LDH) materials, possess layered structures with high specific surface area, distinctive electron distribution, outstanding catalytic activity and stability in alkaline solutions, as well as low cost.[35, 138] Pristine TMOHs own excellent activities in OER, which are comparable to TMOs. Moreover, TMOHs are also great candidates for alkaline HER because they can effectively adsorb hydroxyl species and subsequently catalyze their dissociation.[57] Therefore, TMOHs can largely facilitate the Volmer step. On the other hand, the following hydrogen evolution step (Heyrovsky step or Tafel step) requires another active substance for the adsorption and recombination of reactive hydrogen intermediates.[55, 139] Therefore, hybridizing TMOHs with those conventional HER electrocatalysts (X) is an efficient approach to obtain high-performance catalysts for alkaline HER. Successful applications “TMOHs + X” hybrids have been extensively reported, and several typical samples are detailed in this part.

Combining TMOHs with noble metals cam fabricate high-activity catalysts. The derived composites can take advantage of high catalytic activities of noble metals and favourable water dissociation ability of TMOHs. To date, Pt-$Ni(OH)_2$,[55, 140-142] $Ni(OH)_2$-PtO_2,[143] Pt-$Co(OH)_2$,[144] $Co(OH)_2$-Au-$Ni(OH)_2$,[145] NiFeRu-LDH,[56] PtO_2-CoOOH,[146] etc. have been studied as excellent catalysts in alkaline HER. Lately, Yu et al. discussed the influence of crystal structure (α- and β-$Ni(OH)_2$) on the performance of $Ni(OH)_2$/Pt.[55] The experimental results indicated that β-$Ni(OH)_2$/Pt exhibited the best catalytic activity, followed by α-$Ni(OH)_2$/Pt and Pt (**Figure 8a** and **b**). Further study indicated that the adsorption of H_2O on the β-$Ni(OH)_2$/Pt surface was more favourable than that on the α-$Ni(OH)_2$/Pt surface, declaring the stronger hydrogen bonding interactions between β-$Ni(OH)_2$ and water molecules. The calculated free energies of β-$Ni(OH)_2$/Pt were lower

View Article Online
DOI: 10.1039/C9TA03220G

than those of α-$Ni(OH)_2$/Pt, revealing more feasible Volmer and Heyrovsky steps at the β-$Ni(OH)_2$/Pt surface. Moreover, the charge difference isosurface of the α- or β-$Ni(OH)_2$/Pt surface disclosed noticeable charge transfers between Pt and α- or β-$Ni(OH)_2$ **(Figure 8c)**. The local density of states (LDOS) of β-$Ni(OH)_2$/Pt exhibited more significant peaks, confirming β-$Ni(OH)_2$/Pt was more active than the α-$Ni(OH)_2$/Pt **(Figure 8d)**. The high activity of the β-$Ni(OH)_2$/Pt hybrid mostly aroused from the high edging catalytic activities of β-$Ni(OH)_2$ and its strong interaction with Pt substrate that significantly improved the catalytic activity of Pt for alkaline HER.[55] Shortly, the better performance of β-$Ni(OH)_2$/Pt results from the coupling effect with optimized electron configures toward favourable binding with H_2O molecules **(Figure 8e)**. Using noble metals as heteroatom dopants can further tailor the activity of LDH. Take Ru as an example, Chen et al. designed a Ru-doped NiFe-LDH with a one-pot hydrothermal approach **(Figure 8f)**.[56] The as-prepared NiFeRu-LDH sample displayed higher catalytic activities than the pristine NiFe-LDH and Pt/C. Surprisingly, the low overpotential (η_{10} = 29 mV) and Tafel slope (31 mV dec^{-1}) were achieved which surpassed most of the reported catalysts (**Figure 8g** and **h**). Theoretical calculations demonstrated that the water dissociation energy barrier of NiFeRu-LDH was quite lower than that of NiFe-LDH (0.50 eV vs. 1.02 eV). Consequently, the presence of Ru highly improved the sluggish Volmer step of NiFe-LDH. However, little difference was found in the hydrogen adsorption free energy, so the Tafel step was merely influenced (**Figure 8i** and **j**).

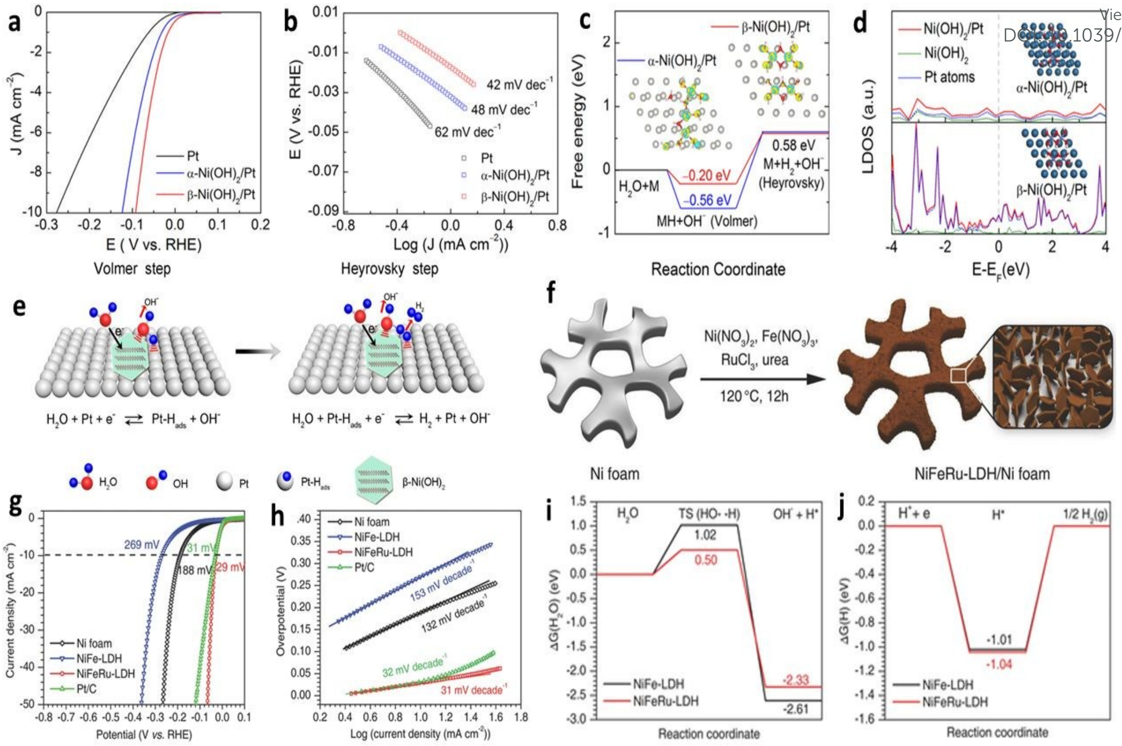

Figure 8. (a) LSV curves and (b) Tafel plots of Pt, α-Ni(OH)$_2$/Pt, and β-Ni(OH)$_2$/Pt electrodes for HER in 0.1 M KOH. (c) Adsorption free energy diagram for the Volmer and Heyrovsky steps. (d) LDOS of the α- or β-Ni(OH)$_2$/Pt electrode. (e) Schematic diagrams of the Ni(OH)$_2$/Pt electrode (only a β-Ni(OH)$_2$ sheet is shown as an example) for Volmer and Heyrovsky steps during HER. (a- e). Reproduced with permission.[55] Copyright 2018, American Chemical Society. (f) Schematic illustration for in situ growth of the NiFeRu-LDH on the Ni foam. (g) Polarization curves and (h) corresponding Tafel plots of the NiFeRu-LDH, NiFe-LDH, nickel foam, and Pt/C electrocatalysts. (i) Calculated adsorption free energy diagrams for the Volmer step and (j) the Tafel step on the as-built NiFe-LDH and NiFeRu-LDH models. (f- j). Reproduced with permission.[56] Copyright 2018, Wiley-VCH.

Integrating TMOHs and TM-based active compounds such as transition metal sulfides (TMSs) can produce high-performance and low-cost catalysts. For example, Hu et al. designed a MoS$_2$/NiCo-LDH hybrid by a two-step hydrothermal process.[57] The HRTEM image revealed the co-existence of MoS$_2$ and NiCo-LDH, as well as the interface between the (015) facet of NiCo-LDH and the neighboring (002) facet of MoS$_2$ **(Figure 9a)**. The hybrids exhibited better catalytic activities than sole MoS$_2$ and NiCo-LDH, suggesting the synergistic effect between MoS$_2$ and NiCo-LDH (**Figure 9b** and **c**). The enhanced alkaline HER kinetics was also implied by the electrochemical impedance spectroscopy (EIS) that the hybrids owned a quite lower charge-transfer resistance than MoS_2 (1.7 Ω vs. 11.2 Ω, η = 200 mV) **(Figure 9d)**. DFT calculations demonstrated the activation energies for different steps of MoS_2/NiCo-LDH were all lower than those of the bare MoS_2. Accordingly, hybridizing of MoS_2 with NiCo-LDH can facilitate the overall HER process through synergistic chemisorption of H on MoS_2 and OH on LDH **(Figure 9e** and **f)**. Apart from MoS_2/LDHs, MoS_2-CoOOH,[147] WS_2,[148] $NiS_2/Ni(OH)_2$,[149] Ni_3S_2/NiOOH,[150] and $Ni(OH)_2$-CoS_2[151] are also appealing catalysts which realised promoted activities in alkaline HER. Apart from the TMSs, electroactive materials with other anions also exhibit great potentials as co-catalysts, such as $CoNiSe_2$@CoNi-LDHs,[71] $Ni(OH)_2/NiSe_2$,[152] $Ni(OH)_2$-Ni_3N,[153] $Ni(OH)_2$-WP,[154] $Ni(OH)_2$-Ni_2P,[155] NiFe-LDH/CeO_x[156]. The combination may vary from one to another, but the origin of synergy is similar. Specifically, the present of TMOHs can optimize the dissociation of water molecules and concomitant generation of hydrogen intermediates (H_{ad}) which subsequently adsorb on catalyst surfaces and finally recombine into H_2.

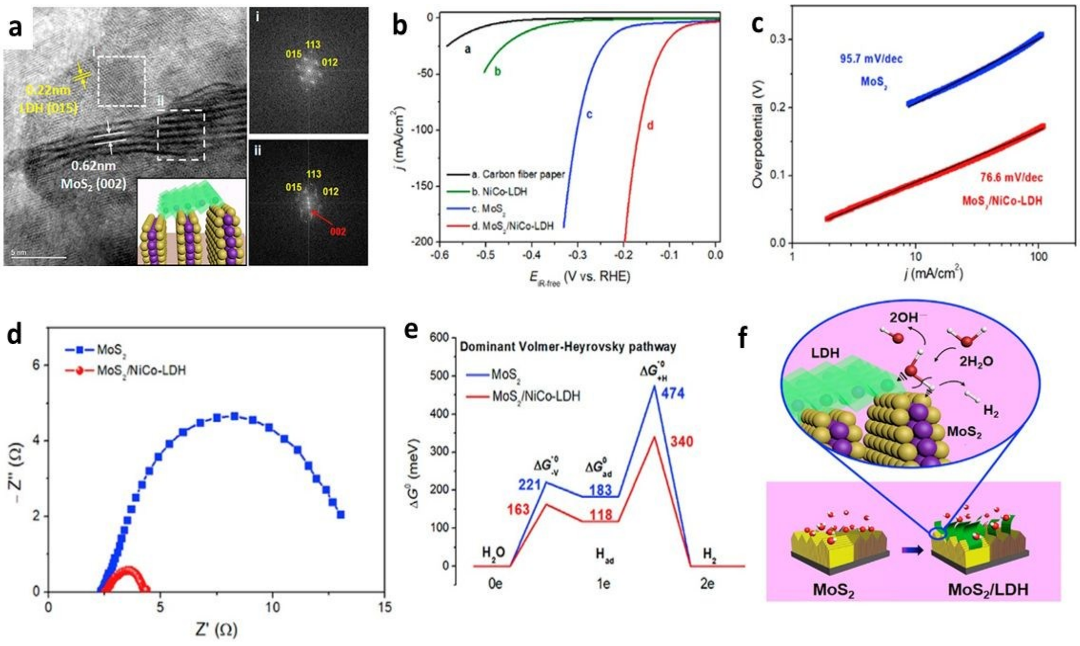

Figure 9. (a) HRTEM image of the MoS_2/NiCo-LDH composite. The corresponding FFT patterns of the selected areas marked by white dashed squares (i and ii) are shown.

Inset: schematic illustration of the designed MoS_2/NiCo-LDH heterostructure. (b) Polarization curves of the CFP substrate, bare NiCo-LDH, MoS_2, and MoS_2/NiCo-LDH composite catalysts. (c) Tafel plots for the bare MoS_2 and MoS_2/NiCo-LDH composite catalysts. (d) Nyquist plots of the bare MoS_2 and MoS_2/NiCo-LDH composite catalysts at the overpotential of 200 mV. (e) Free energy diagram of the dominant Volmer-Heyrovsky pathway for HER in the alkaline electrolyte for bare MoS_2 (blue) and MoS_2/NiCo-LDH composite (red) catalysts. (f) Schematic illustration of the HER in MoS_2/LDH interface in an alkaline environment. The synergistic chemisorption of H (on MoS_2) and OH (on LDH) benefits the water dissociation step. Reproduced with permission.[57] Copyright 2018, Elsevier Ltd.

3.3.3 Transition metal sulfides

Moreover, TMSs themselves are outstanding catalysts for alkaline HER due to the high electrocatalytic activity and natural abundance.[37] Researchers hold different opinions on the role of S atoms in TMSs in their excellent catalytic activities. On one hand, catalytic activities was determined by the electronic properties of S atoms. S atoms in TMSs can withdraw electrons from the transition metals due to the high electronegativity, and then sulphur can act as the active sites to stabilise the reaction intermediates.[157] On the other hand, S atoms may play an indirect role in alkaline HER by creating S-vacancies to tailor the electron density of TMs or improving water dissociation via the $S^{\delta-}$-TM^{n+}-H_2O network.[157, 158] Currently, MoS_2, Ni_xS_y, and Co_xS_y are the most reported TMSs, and the fabrication and catalysis of MoS_2 have been extensively reviewed.[3, 18, 159, 160] Therefore, in this part, we put the emphasis on the alkaline HER application of other TMSs.

Ni_xS_y (NiS, NiS_2, Ni_3S_2, etc.) manifests good structural stabilities and appealing catalytic activities which exhibits great potentials for alkaline HER, especially the Ni_3S_2. To further elevate the catalytic performance of Ni_3S_2, doping appears as an attractive method. Take nitrogen as an example, Kou et al. prepared an N-doped Ni_3S_2/NF through hydrothermal reaction and ammonia treatment (**Figure 10a**).[58] Compared to the pristine Ni_3S_2, the modified one exhibited a better alkaline HER ability with a lower overpotential and Tafel slope (**Figure 10b** and **c**). In addition, theoretical analysis implied that the

View Article Online
DOI: 10.1039/C9TA03220G

outstanding catalytic activity of N-doped Ni_3S_2 could be attributed to the enriched active sites on the catalyst surface and the favourable ΔG_{H*} (**Figure 10d**). Interestingly, it was unveiled that the activity of Ni_3S_2 particularly relied on the coordination number of the surface S atoms, as well as the charge depletion of the neighboring Ni atoms. Yu et al. also suggested that N-doping could significantly improve the electrocatalytic activity of Ni_2S_3.[161] The N-doped Ni_2S_3 possessed a high surface area, and the great differences in electronegativity between H and N facilitated the adsorption of H. These features significantly upgraded the catalytic performance of N-doped Ni_2S_3, with a lower overpotential compared to Ni_2S_3 (η_{10} =105 mV *vs.* 228 mV). Similarly, Zhong and co-workers investigated the electrocatalytic performance of N-doped Ni_3S_2/VS_2.[59] Compared with bare Ni_3S_2/VS_2, the N-doped sample exhibited improved conductivity and larger catalytically active area. Consequently, the N-doped Ni_3S_2/VS_2 exhibited a lower overpotential (η_{10} =151 mV) and a lower Tafel slope (107.5 mV dec^{-1}) than other samples (e.g., Ni_3S_2/VS_2, N-doped Ni_3S_2, and Ni_3S_2). Briefly, the N-doping method can enrich the catalytic active sites, improve the conductivity and optimize the adsorption energy of reaction intermediates.

Other than anion-doping, introducing metal atoms into Ni_3S_2 frameworks also can improve the electrocatalytic performance. Jian et al. fabricated Sn-doped Ni_3S_2 nanosheets by a facile hydrothermal process.[60] The modified Ni_3S_2 owned a small overpotential (η_{100} =171 mV) and a low Tafel slope (33.8 mV dec^{-1}). Impressively, the Sn-Ni_3S_2/NF only took a very low potential of 1.46V at 10 mA cm^{-2} for the overall water splitting. The Sn doping changed the morphology of pristine Ni_3S_2 and improved the intrinsic catalytic performance. Apart from Sn, other metals (e.g., Fe,[61] V,[162] Mn[163]) also act as effective dopants that can improve the alkaline HER activity of Ni_3S_2. For example, Zhang et al. disclosed the mechanism of for the enhanced electrocatalytic performance of Fe-Ni_3S_2/NF by systematic experiments and DFT calculations.[61] The Fe-doping could enlarge the active surface area, improve the electronic conductivity, boost the water adsorption ability, and optimize the H adsorption energy of Ni_3S_2. These advantages cooperatively benefit the overall electrocatalytic performance of $Fe_{17.5\%}$-Ni_3S_2/NF, with a low Tafel slope of 95 mV dec^{-1} and a low overpotential of 47 mV at 10 mA cm^{-2}.

Defect engineering by constructing S vacancies can further tailor the catalytic performance of TMSs. Theoretically, the presence of vacancies can modify the physicochemical properties and the electronic configuration of TMSs,[164] thus refining the intrinsic activity of catalysts. Zhang and co-workers fabricated non-layered structure of Co_3S_4 ultrathin porous nanosheets with plentiful S vacancies (Co_3S_4 PNS_{vac}) by Ar plasma-induced dry exfoliation (**Figure 10e**).[62] The obvious electron paramagnetic resonance (EPR) signal with g=2.003 implied the abundant S vacancies (**Figure 10f**). Electrochemical experiments indicated that the mass activity of Co_3S_4 PNS_{vac} was higher than that of pristine Co_3S_4 samples. As a result, the modified Co_3S_4 owned an extraordinarily large mass activity of 1056.6 A g^{-1} at an overpotential of 200 mV, which was superior to the Pt/C (20 wt.%) electrode (**Figure 10g**). In addition, Co_3S_4 PNS_{vac} possessed a lower water adsorption energy than Co_3S_4, so S vacancies could efficiently expedite the initial step of alkaline HER (**Figure 10h**). The activation energy barrier of water dissociation process for Co_3S_4 PNS_{vac} was also the lowest, which could benefit the formation of catalyst-H_{ads} (**Figure 10i**). Altogether, the kinetics of alkaline HER can be impressively boosted. Moreover, Wu et al. suggested that the rich S vacancies/defect sites in CoMoS layers could enhance the reactive sites for alkaline HER,[63] because the catalytic active sites located at the basal edges of catalysts. More relevant information on

View Article Online
DOI: 10.1039/C9TA03220G

this topic can be found in the previous reviews by Jia et al.,[165] Yang et al.,[166] and Zhang et al.[164]

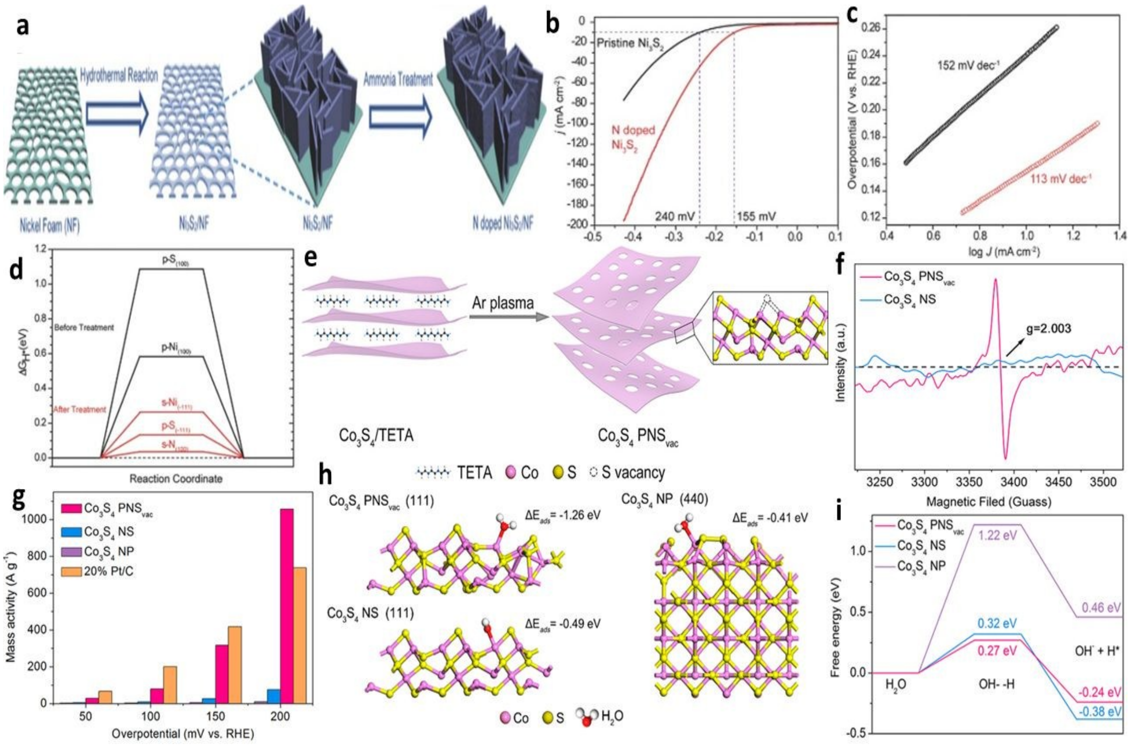

Figure 10. (a) Schematic illustration of the synthesis of Ni_3S_2/NF and N-doped Ni_3S_2/NF. (b) HER polarization curves of the pristine (black) and N-doped Ni_3S_2/NF (red) collected in 1 M KOH at a scan rate of 5 mV s^{-1} (dashed lines highlight the potential at 10 mA cm^{-2}). (c) Tafel plots of the pristine and N-doped Ni_3S_2/NF. (d) Reaction energy of H adsorption, ΔG_{H*}, displayed for sites present before (black lines) and after treatment (red lines). (a- d). Reproduced with permission.[58] Copyright 2018, Wiley-VCH. (e) Scheme for the preparation of Co_3S_4 PNS_{vac}. (f) EPR spectra of Co_3S_4 PNS_{vac} and Co_3S_4 NS. (g) The mass activity of different samples as a function of overpotential. (h) The adsorption energies (ΔE_{ads}) and (i) the activation energy barriers of an H_2O molecule on three models surfaces. (e- i). Reproduced with permission.[62] Copyright 2018, American Chemical Society.

Recently, a growing number of high-performance TMSs are fabricated as hybrids, such as MoS_2-CoS_2@MoO_2,[167] MoS_2/$LaNiO_{3-\delta}$,[168] MoS_2-$Co(OH)_2$,[169] MoS_2/Ni_3S_2/Ni,[170] MoS_2/MoP/NC[171] and Pt_3Ni/NiS[172]. These composites commonly consist of two or more active components. Strong interactions between the different compounds can induce the electron transfer which will significantly optimize the intrinsic catalytic activity of the metallic sites in TMSs.[32] Recently, Feng et al. reported a Cu-Ni_3S_2 hybrid for alkaline HER (**Figure 11 a** and **b**).[32] Compared with the single Ni_3S_2 and Cu-based samples, the metal/metal sulfide hybrids manifested a smaller overpotential (η_{10} =128 mV) and a lower Tafel slope (76.2 mV dec^{-1}) (**Figure 11c** and **d**). The DFT calculations indicated that the electron density of Cu increased while the electron density of Ni_3S_2 decreased. The positively charged Cu could adsorb and activate H_2O molecules by capturing O atoms of water. As a result, the Cu/Ni_3S_2 hybrids owned a lower water adsorption energy and could promote H_2O adsorption for alkaline HER (**Figure 11e**). In addition, the Cu/Ni_3S_2 hybrids attained appropriate adsorption energy of H (**Figure 11f**), which was beneficial to H desorption. In short, the hybridization of Cu with Ni_3S_2 can facilitate the entire process of the alkaline process (**Figure 11g**).

In addition, the mixed TMSs possess more active sites and the electron tunneling effects between different TMSs also benefit the alkaline HER. For instance, Liu et al. fabricated a 3D heteromorphic $NiCo_2S_4$/Ni_3S_2/NF network with NiCo-LDH as the precursor (**Figure 11i**).[64] The HRTEM image elucidated the interfacial heterostructure between $NiCo_2S_4$ and Ni_3S_2 terminations (**Figure 11h**). The electrochemical tests indicated that $NiCo_2S_4$/Ni_3S_2/NF manifested a better catalytic activity towards HER with the lowest overpotential (η_{10} =119 mV) and smallest Tafer slope (105.2 mV dec^{-1}) compared to other samples in **Figure 11j** and **k**. Moreover, recently documented hybrids, like NiS_2/MoS_2,[173] MoS_2/Co_9S_8,[174] MoS_2/NiS,[175, 176] NiS/NiS_2/Ni_3S_2,[177] MoS_2/Ni_3S_2,[178] $NiCo_2S_4$/Co_9S_8[179] also exhibit distinguished catalytic performance in alkaline HER.

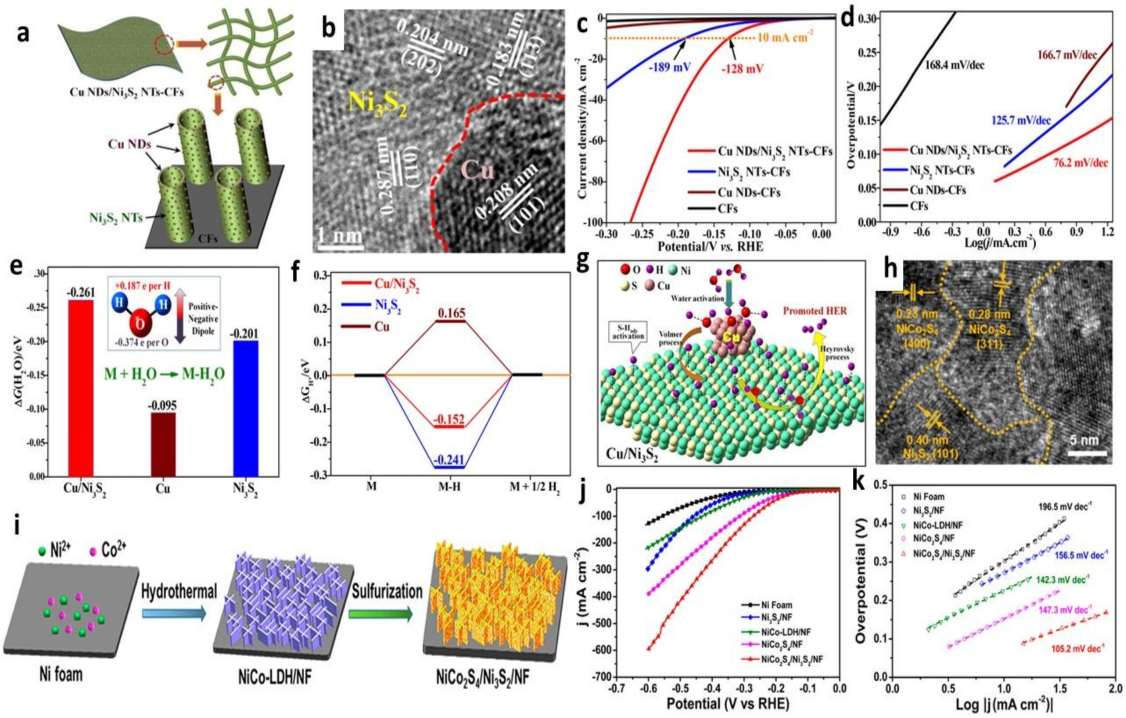

Figure 11. (a) Schematic illustration of the microstructure of Cu NDs/Ni_3S_2 NTs-CFs. (b) HRTEM image of Cu/Ni_3S_2 border. (c) Polarization curves and (d) Tafel plots of Cu NDs/Ni_3S_2 NTs-CFs, Ni_3S_2 NTs-CFs, Cu NDs-CFs, and CFs. (e) The calculated adsorption free energy changes of H_2O on Cu/Ni_3S_2, Ni_3S_2, and Cu. (f) H adsorption free energy profiles of Cu NDs/Ni_3S_2 hybrid, Ni_3S_2, and Cu. (g) Schematic illustration of water adsorption, water activation, and hydrogen generation processes on Cu/Ni_3S_2. (a-g). Reproduced with permission.[32] Copyright 2018, American Chemical Society. (h) HRTEM images of $NiCo_2S_4$/Ni_3S_2/NF. (i) Schematic illustration of 3D $NiCo_2S_4$/Ni_3S_2/NF. (j) Polarization curves and (k) the corresponding Tafel slopes of $NiCo_2S_4$/Ni_3S_2/NF, NiCo-LDH/NF, $NiCo_2S_4$/NF, Ni_3S_2/NF, and bare Ni foam at a scan rate of 5 mV s^{-1} without IR correction. (h- k). Reproduced with permission.[64] Copyright 2018, American Chemical Society.

3.3.4 Transition metal selenides

Transition metal selenides (TMSes) have allured increasing attention in electrocatalysis due to their metallic nature with low intrinsic electrical resistivity. Compared to TMOs and TMSs, TMSes manifests a faster electron-transfer capacity so as to facilitate the electrocatalytic processes. Mo_xSe_y, Co_xSe_y, and Ni_xSe_y are the most popular electrocatalysts for alkaline HER in this series. However, the bare TMSes still requires improvement to compete with the noble metal-based electrocatalysts.

View Article Online
DOI: 10.1039/C9TA03220G

Doping TMSes with heteroatoms is a popular approach to enhance the intrinsic catalytic activity. The introduction of a second cation or anion may have different influences on the properties of original TMSes, giving rise to modulated catalytic performance. For example, Zhang et al. explored the role of Co in the Co-WSe_2/MWNTs, and they found that the introduction of Co could improve the inherent activity of the active sites.[65] However, the Co-doped catalyst showed a poor activity-stability relationship in alkaline solutions. The main reason is that the Co incorporation resulted in a high proportion of metal atoms being exposed on the surface, rendering the catalyst thermodynamically metastable and vulnerable to oxidation. In another study, Zhao and co-authors unveiled the importance of Ni dopant in $MoSe_2$.[66] The dopants can not only facilitate water adsorption but also optimize H adsorption. Similarly, Jing et.al suggested that the N-doped $NiSe_2$ had a lower ΔG_{H*} and water adsorption energy compared to the bare $NiSe_2$.[67] Consequently, the N-doped catalysts demonstrate better electrocatalytic performance with a low overpotential of 86 mV at 10 mA cm^{-2}. Interestingly, the role of P in the P-substituted $CoSe_2$ is quite different.[68] Zhu et al. suggested that the presence of P could generate more vacancies/defects in the $CoSe_2$ and significantly benefited the structural transformation into metallic cobalt which is the intrinsic catalytic species for HER.

Hybridizing with conductive carbon-based materials/substrates (e.g., carbon cloth,[180] N-doped carbon framework,[181] carbon fiber paper,[182] N-doped graphene,[183] N-doped carbon nanotube,[184] N-doped porous carbon,[185, 186] carbon microspheres[187]) can further enhance the conductivity of TMSes. Meanwhile, the carbon skeleton can prevent TMSes particles from self-aggregation and corrosion.[70, 181, 182, 187] Moreover, coupling with carbons can regulate the electron spin density and charge distribution of the TMSes surface, which

View Article Online
DOI: 10.1039/C9TA03220G

manipulated the intrinsic activity of the hybrids.[181] Recently, Wang et al. prepared $CoSe_2$-$MoSe_2$ hybrids with reduced graphene oxide and amorphous carbon (CS-MS/rGO-C) by a scalable spray-drying and selenization process.[187] Compared with CS-MS, CS-MS/C, and CS-MS/rGO, CS-MS/rGO-C exhibited the best catalytic performance in alkaline HER (Tafel slope of 83.2 mV dec^{-1}, η_{10} of 215 mV). Further study indicated that the appealing catalytic activity of CS-MS/rGO-C stemmed from two aspects. Firstly, the hollow porous microspheres significantly increased the contact areas between the electrolyte and the catalyst, thus enabling enormous active sites exposed into the electrolyte. Secondly, the conductivity of the composite could be remarkably improved by the highly conductive carbon substrate.

Bimetallic selenides own obvious advantages over those monometallic selenides due to the optimized electronic structure by two metal elements.[70] Taking $NiCoSe_2$ as an example, Yu and co-workers fabricated the TMSes by an electrodeposition technique (**Figure 12a**).[70] The HRTEM image displayed a clear lattice fringe of hexagonal $NiCoSe_2$ (**Figure 12b**). The results of electrochemical experiments revealed that bimetallic $NiCoSe_2$ possessed a better catalytic performance than CoSe, NiSe, and NiCo-OH, with a lower overpotential (η_{10} = 112.7 mV) and a smaller Tafel slope (65 mV dec^{-1}) (**Figure 12c**). The electronic structure of $NiCoSe_2$ showed that Ni, Co, and Se contributed cooperatively to the total DOS (TDOS), and the overlap *d*-orbitals of Ni and Co implied a covalent interaction between the Co and Ni atoms. What's more, the PDOS of $NiCoSe_2$ revealed that all the *d* orbitals from Ni, Co and Se contributed dominantly to the TDOS, and the Se *p*- orbitals contributed to the covalent interactions among the three elements (**Figure 12d** and **e**). Such regulated electronic structure vastly enhanced the intrinsic electrocatalytic activity of $NiCoSe_2$. Moreover, the structurally engineered mixed metal

View Article Online
DOI: 10.1039/C9TA03220G

selenides manifested a high superhydrophilicity, which facilitated the water adsorption process (**Figure 12f** and **g**).

Hybridizing TMSes with other electroactive materials is well recognized as an appropriate method to further improve their electrocatalytic activity. Typically, TMSes/LDHs (e.g., $CoNiSe_2$@CoNi-LDHs/NF,[71] CoSe@NiFe-LDH/NF,[188] SWCNTs/ex-$MoSe_2$:$NiCl_2$[189]), TMSes/TMSes (e.g., $MoSe_2$-$CoSe_2$,[69, 72, 187, 190] $MoSe_2$-CoSe,[185] $MoSe_2$-NiSe,[191], $MoSe_2$-$Ni_{0.85}Se$[192]), and TMSes/TMCs (e.g., SWCNTs/$MoSe_2$-2:Mo_2C[193]) have been applied as high-performance catalysts for alkaline HER. Taking $CoNiSe_2$@CoNi-LDHs/NF as an example, Yang et al. found that the combination of 1D $CoNiSe_2$ with 2D CoNi-LDHs could notably improve the electrocatalytic activity, with an overpotential of η_{10} = 215 mV.[71] DFT calculations and in-situ Raman tests revealed that the LDHs-$CoNiSe_2$ interfaces could significantly facilitate water adsorption and dissociation to generate H_{ads} because of the strong electronic interactions through the interface, thus enhancing the alkaline HER process.

Constructing TMSe/TMSe heterostructures also can enhance the catalytic activity of the bare TMSe catalysts, especially for the $MoSe_2$-based materials. For instance, Zhao et al. reported that the $CoSe_2$/$MoSe_2$ heterostructures delivered a better activity in alkaline HER than $MoSe_2$.[190] $CoSe_2$ species was revealed to be able to facilitate the water adsorption and subsequent dissociation processes. Meanwhile, $MoSe_2$ species provided the active sites for adsorption and combination of adsorbed hydrogen (H*). In another study, Wang et al. prepared hierarchical $MoSe_2$-$CoSe_2$ nanotubes (MS-CS NTs) by a facile hydrothermal selenization process (**Figure 12h**).[72] The prepared nanotubes consisted of few-layered $MoSe_2$ nanosheets and $CoSe_2$ nanoparticles (**Figure 12i**).

View Article Online
DOI: 10.1039/C9TA03220G

Electrochemical tests marked that the MS-CS NTs owned a higher catalytic activity than $MoSe_2$ and $CoSe_2$ in 1M KOH (**Figure 12j** and **k**). The authors concluded that the highly conductive $CoSe_2$ particles in the few-layered $MoSe_2$ nanosheets significantly refined the charge transfer process, thus improving the electrocatalytic performance.

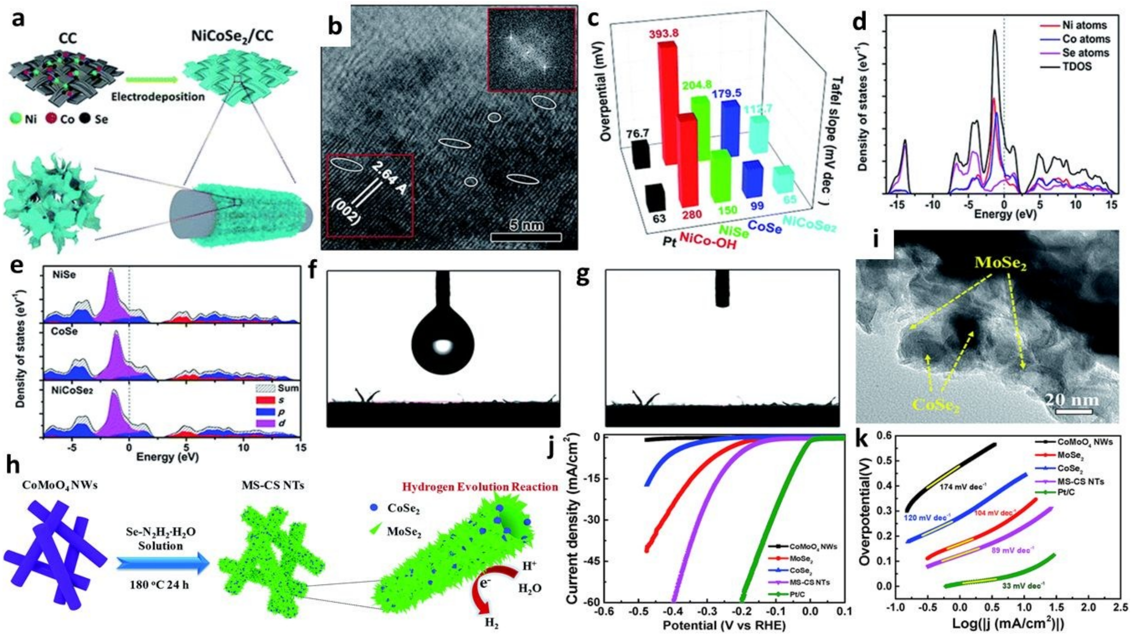

Figure 12. (a) Schematic diagram of the construction of the $NiCoSe_2$ nanosheet network. (b) HRTEM image of the $NiCoSe_2$. The inset of (b) shows the corresponding fast Fourier transform (FFT) pattern. (c) Comparison of the overpotentials required at 10 mA cm^{-2} current density and Tafel slopes. (d) Calculated total and partial electronic density of states of $NiCoSe_2$. (e) The electronic density of states for NiSe, CoSe, and $NiCoSe_2$. The Fermi level is set at 0 eV. The images (f) before and (g) after the water drop fell on the surface of $NiCoSe_2$/CC. (a- g). Reproduced with permission.[70] Copyright 2018, The Royal Society of Chemistry. (h) Schematic illustration of the preparation of MS-CS NTs. (i) TEM image of MS-CS NTs. (j) Polarization curves and (k) Tafel plots of $CoMoO_4$ NW, $MoSe_2$, $CoSe_2$, MS-CS NT and commercial Pt/C catalysts in 1 M KOH. (h- k). Reproduced with permission.[72] Copyright 2018, The Royal Society of Chemistry.

It is noteworthy to mention that the catalytic performance of materials considerately relies on their phase. For instance, 1T-MoS_2 exhibits a much higher reactivity than the thermodynamically favoured 2H-MoS_2.[20] Similarly, phase engineering can be utilized to tune the intrinsic catalytic activity of TMSe. Chen et al. found that the cubic phase $CoSe_2$ (c-$CoSe_2$) manifested notably improved activities over the orthorhombic phase $CoSe_2$ (o-

$CoSe_2$) in alkaline HER.[73] This is because c-$CoSe_2$ possessed a superior electrical conductivity, the ideal water adsorption energy, as well as faster transformation efficiency of H_{ads} into molecular hydrogen. In contrast, Zheng et al. found that the catalytic properties of c-$CoSe_2$ were inferior to P-doped o-$CoSe_2$ (o-$CoSe_2$|P) by a P-assisted transition process (**Figure 13a**).[74] Combined with XRD patterns, X-ray photoelectron spectroscopy (XPS) spectra, EDX spectra, and Raman spectra, the phase transformation process was illustrated in **Figure 13b**. The electrochemical tests suggested that o-$CoSe_2$|P outperformed c-$CoSe_2$ and annealed $CoSe_2$, and was comparable to that of Pt/C (**Figure 13c** and **d**). The SCN^- probing tests identified that P atoms were intrinsic active sites (**Figure 13e**). The DFT calculations suggested that the enriched charge density of o-$CoSe_2$|P, especially at the P-doped regions is much beneficial to HER process (**Figure 13f**). The obtained ΔG_{H*} also revealed that the P site owned the best activity for water reduction (**Figure 13g**). In addition, the Co sites in o-$CoSe_2$|P exhibited better water adsorption and dissociation abilities than other components in **Figure 13h** and **i.** The synergistic effect of P and Co in o-$CoSe_2$|P gave rise to the best catalytic performance. Additionally, a partial phase transition from Ni_3Se_2 to NiSe created the phase junctions (Ni_3Se_2/NiSe) and demonstrated a better electrocatalytic activity for alkaline HER than the single-phase counterparts.[75] This is mainly attributed to the maximum exposure of the active sites, fast charge transport, and favourable OH^- and H^+ adsorptions. Therefore, the strategy of constructing heterostructures by partial phase transformation is inspiring for the rational design of other high-activity electrocatalysts.

View Article Online
DOI: 10.1039/C9TA03220G

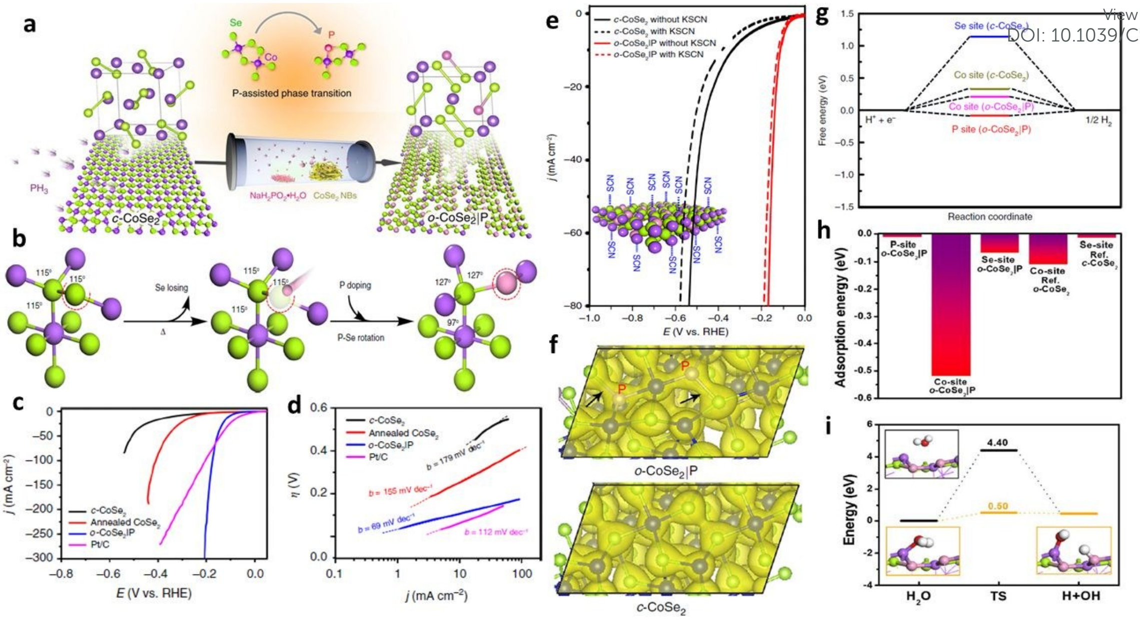

Figure 13. (a) Synthesis and physical characterization of o-$CoSe_2$|P. (b) Schematic of the P-doping-assisted phase-transition process from cubic to orthorhombic phases in $CoSe_2$. (c) Polarization curves and (d) Tafel plots for the HER on c-$CoSe_2$, annealed c-$CoSe_2$, o-$CoSe_2$|P, and commercial Pt/C catalyst (20 wt %). Catalyst loading: ~1.02 mg cm^{-2}. Sweep rate: 10 mV s^{-1}. (e) Comparison of SCN^- ions effects on the HER activities of c-$CoSe_2$ and o-$CoSe_2$|P, respectively. The inset shows the schematic of Co centers blocked by the SCN^- ions. (f) Calculated charge density distribution for o-$CoSe_2$|P (up) and c-$CoSe_2$ (down) catalysts. (g) Free energy diagrams for hydrogen adsorption at different sites on the (111) surface of o-$CoSe_2$|P (8 wt%) and c-$CoSe_2$. (h) Adsorption energy of H_2O molecule on o-$CoSe_2$|P surface. (i) H_2O dissociation in a vacuum and on o-$CoSe_2$|P surface. Reproduced with permission.[74] Copyright 2018, Nature Publishing Group.

3.3.5 Transition metal tellurides

Transition metal tellurides (TMTes) are emerging catalysts for alkaline HER, although only a few of TMTes have been reported. Compared with the congeners (O, S, Se), tellurium possesses a higher metallic characteristic, endowing a better electronic conductivity to TMTes and a higher degree of covalency in the metal-chalcogen bonds.[76, 194] These merits can benefit HER in alkaline solutions. To date, Co_xTe_y,[76, 195, 196] Ni_xTe_y,[194, 197, 198] and Mo_xTe_y[199] have demonstrated respectful catalytic properties towards alkaline HER. In a recent study, Wang et al. prepared component-controllable cobalt telluride nanoparticles by chemical vapor deposition.[76] Compared with CoTe/C and $CoTe_2$/C, the component optimized $Co_{1.11}Te_2$/C yielded more reducible Co species and a higher surface dispersion of Co ions. Electrochemical tests stated that the catalytic activity of $Co_{1.11}Te_2$/C was higher than CoTe/C and $CoTe_2$/C, with a low overpotential (η_{10} = 178 mV) and a small Tafel slope (77.3 mV dec^{-1}) (**Figure 14a** and **b**). Further, $Co_{1.11}Te_2$/C showed the smallest charge resistance and the largest double layer capacitance, which implied a fast electron-migration capacity and a large active surface area, respectively. (**Figure 14c** and **d**). $Co_{1.11}Te_2$/C also presented a good cycling capability with negligible performance loss in **Figure 14e**. The DFT calculations showed that ΔG_{H*} of $Co_{1.11}Te_2$ was the smallest one, suggesting the optimal H adsorption on the $Co_{1.11}Te_2$ surface in the alkaline HER process. The order of computational $|\Delta G_{H*}|$ successfully verified the experimental results. As aforementioned, the catalytic applications of TMTes are at the early stage, so further explorations are encouraged to develop high-performance TMTes toward alkaline HER.

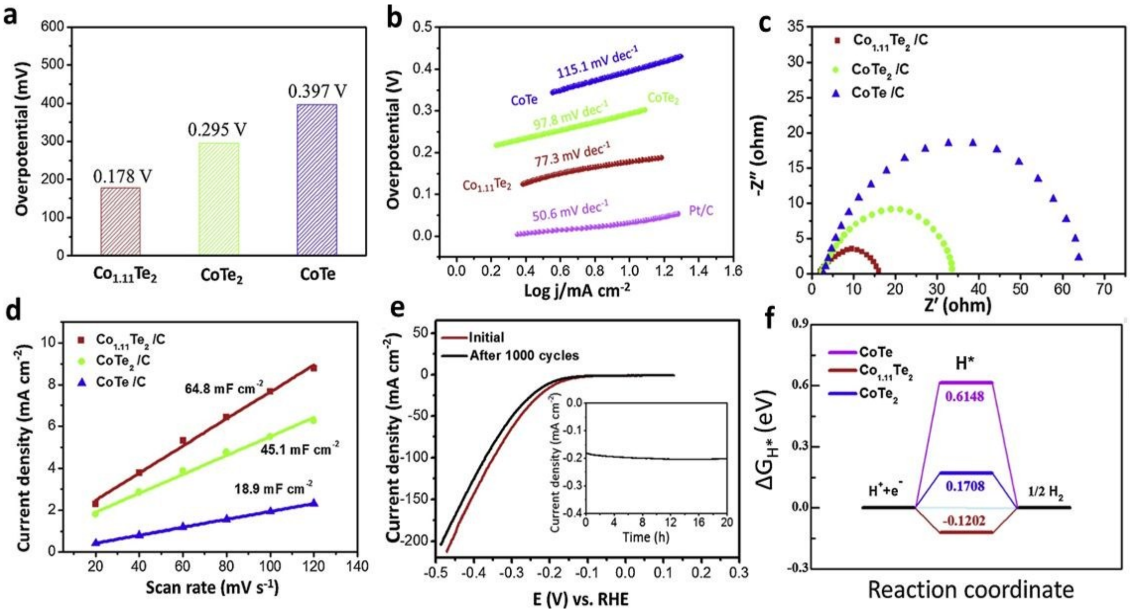

Figure 14. (a) Overpotentials of $Co_{1.11}Te_2$/C, $CoTe_2$/C and CoTe/C at the current of 10 mA cm^{-2}. (b) Tafel slopes of $Co_{1.11}Te_2$/C, $CoTe_2$/C and CoTe/C. (c) Nyquist plots. (d) The plot of double-layer charging current density versus scan rate. (e) CV curves of the $Co_{1.11}Te_2$/C catalyst before and after 1000 cycles and the insert showing chronoamperometric curves at the current of 10 mA cm^{-2}. (f) Gibbs free energy diagram of $CoTe_2$, $Co_{1.11}Te_2$ and CoTe. Reproduced with permission.[76] Copyright 2019, Elsevier Ltd.

3.4 Nitrogen group transition metal catalysts

3.4.1 Transition metal nitrides

Transition metal nitrides (TMNs) are new favourites in alkaline HER which possess unique metallic physiochemical properties and electronic features.[200] The nitrogen elements can raise the *d*-electron density and lead to the contraction of *d*-band of TMs, affording TMNs with the similar electronic structure to the noble metals (i.e., Pd and Pt).[200] Additionally, the distinguished conductivity and good corrosion resistance also make TMNs high-performance electrocatalysts.[201]

Ni_xN_y and Mo_xN_y are the primary documented catalysts. Commonly, the y/x is less than 1 in TM_xN_y, such as Ni_3N,[5, 78, 79, 81] Mo_2N,[202, 203] $Cu_xNi_yFe_{4-x-y}N$,[204] and Ni_3FeN,[205] because incorporation of N atoms into a transition metal lattice is thermodynamically unfavourable.[77] The low valance state of the metal atoms may result in oxidation of TMNs during the electrochemical tests.[206] Thus, creating N-rich TMNs ($x/y < 1$) is a great strategy to ameliorate the longevity and intrinsic activity of catalysts. For example, Jin and co-workers designed Mo_5N_6 nanosheets by a Ni-inducing growth method.[77] Compared with $Ni_{0.2}Mo_{0.8}N$, MoN and Ni_3N, Mo_5N_6 possessed a higher electrocatalytic activity (η_{10} = 94 mV, Tafel slope 66 mV dec^{-1}) and impressive durability in 1M KOH. Further study indicated that the appealing capability of Mo_5N_6 originated from its Pt-like electronic structure and the high valance state of the Mo atoms. Moreover, bimetallic and trimetallic nitrides are recognized to exhibit better abilities than the corresponding single metal nitrides due to the regulated electrical conductivity and the synergy between/among the adjacent heteromatals.[204] The currently reported P-$NiMo_4N_5$,[207]

$Cu_xNi_yFe_{4-x-y}N$,[204] $Cu_xNi_{4-x}N$,[204] FeNi-N,[205] and Ni-Mo-N[9] are identified as high-performance and low-cost catalysts towards alkaline HER.

Hybridizing TMNs with other components (i.e., carbon materials, metals/alloys, TMXs), especially metals, can further upgrade the electrocatalytic performance. In this part, TMN/C (TMN/carbon) and TMN/M (TMN/alloy) will be detailed. Generally, carbon materials prominently work as a conductive substrate, and they can also disperse active sites, protect metallic catalysts from corrosion and regulate the electron culture of the supported TMNs nanoparticles.[200] As a consequence, the addition of carbon materials can significantly improve the catalytic performance of TMNs.[78, 203, 205, 208, 209] For instance, Zhou et al. prepared a carbon layer-coated Ni_3N nanocomposite (Ni_3N@CQDs) which possessed a porous structure (**Figure 15a**) and a few atoms thick amorphous carbon layers coated on the Ni_3N surface (**Figure 15b**).[78] It could be found that O atoms covalently bridged C and Ni atoms and formed Ni-O-C structures (**Figure 15c**). Electrochemical experiments disclosed that Ni_3N@CQDs exhibited higher catalytic activities than GC, CQDs, and Ni_3N, with a lower overpotential (η_{10} = 69 mV) and a small Tafel slope (108 mV dec^{-1}) (**Figure 15d** and **e**). Compared to Ni_3N, Ni_3N@CQDs manifested much better stability (**Figure 15f**), and the advancement of current density could be attributed to the increased number of utilizable active sites due to the activation effect. Hence, the CQDs coating not only upgraded HER activities for the Ni_3N surfaces but also stabilized the catalysts in the alkaline media. Further computational results revealed that the presence of negatively charged C sites became catalytic centers which obviously decreased the energy barrier for the water dissociation step, from 2.33 eV to 1.66 eV, thus accelerating the Volmer step (**Figure 15g** and **h**). Therefore, combining

View Article Online
DOI: 10.1039/C9TA03220G

TMNs with carbon materials into hybrids is an effective approach to develop robust and durable alkaline HER electrocatalysts.

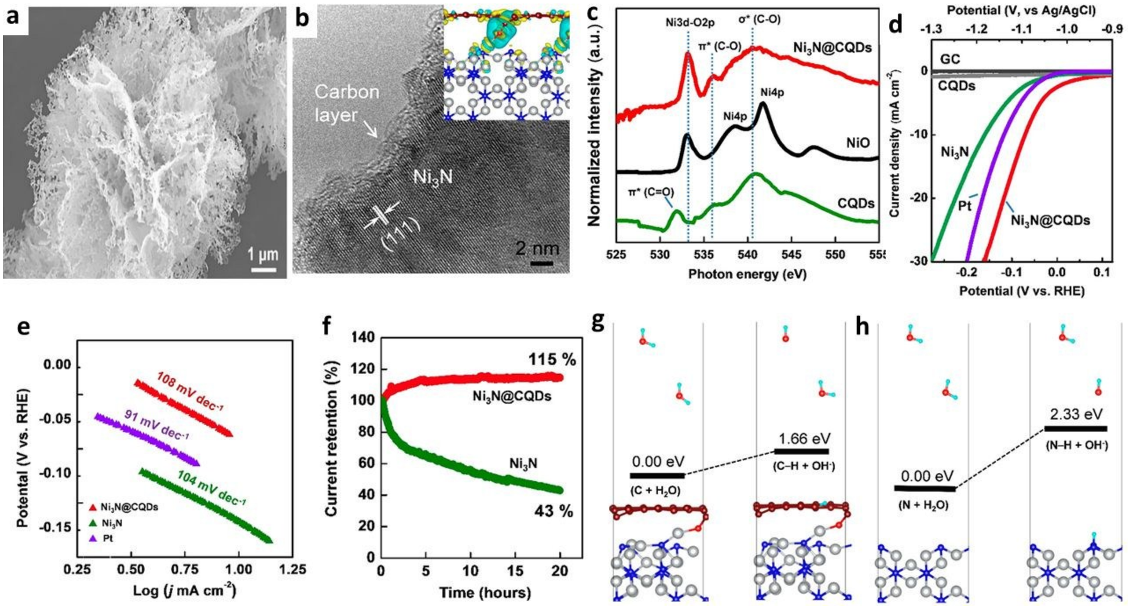

Figure 15. (a) SEM of Ni_3N@CQDs. (b) HRTEM image of Ni3N@CQDs. The inset is the simulated charge distributions in the proposed Ni_3N@CQDs structural model. The loss and the gain of the charge are denoted by yellowish and bluish colors, respectively, with the isosurface values of $\Delta\rho = \pm 2 \times 10^{-3}$ e/Å^3. (c) O K-edge XANES spectra of Ni_3N@CQDs, commercial NiO, and the CQDs treated in NH_3 at 370 °C. (d) LSV polarization curves of Ni_3N@CQDs in comparison with platinum (Pt) electrode, Ni_3N, CQDs, and glassy carbon (GC) electrode in a 1 M KOH aqueous solution. (e) Tafel slopes of Ni_3N@CQDs, Ni_3N and Pt electrode. (f) Normalized HER amperometric I-t curves of Ni_3N@CQDs and Ni_3N at a constant overpotential of 77 mV (-1.1 V *vs* Ag/AgCl). (g, h) Comparison of HER Volmer reaction step and the resultant binding energies on carbon-coated Ni_3N(110) (g) and Ni_3N(110) (h) surfaces, N, Ni, C, O, and H atoms are marked in blue, gray, brown, red, and cyan colors, respectively. Reproduced with permission.[78] Copyright 2018, American Chemical Society.

Heterojunctions can integrate multiple catalytic components for alkaline HER with increased active sites and ungraded electrical conductivity.[80] Furthermore, the interfaces between different active components can further improve the catalytic performance of the hybrids.[209] Novel nanocomposites of TMN and metal/alloy such as Co-Ni_3N,[210] Ni_3N/Ni,[79] Co-Mo_2N,[202] NC-NiCu-NiCuN,[80] Co/CoN,[209] Pt-Ni_3N,[5] Ni/$NiMo_4N_5$,[9] and Co/VN[211] have exhibited superior electrocatalytic capabilities. For example, Song et al.

View Article Online
DOI: 10.1039/C9TA03220G

developed a Ni_3N/Ni interfacial electrocatalysts which owned higher intrinsic specific activities than Pt/C in 1.0M KOH (**Figure 16a** and **b**).[79] The in-depth DFT study demonstrated that H atoms preferred to adsorb along the interfaces between Ni_3N and Ni (**Figure 16c**). Moreover, Ni_3N/Ni possessed a higher water adsorption energy of 0.33 eV than Ni_3N (0.09 eV) and Ni (0.29 eV), as well as the smallest activation energy barrier of water dissociation (**Figure 16d** and **e**). The computational results revealed that the interfacial sites of Ni_3N/Ni provided appropriate binding affinities towards H_2O and H, and facilitated the water dissociation. In another study, Hou et al. fabricated NC-NiCu-NiCuN catalysts with carbonization-/nitridation-induced *in situ* growth strategies.[80] The presence of Ni_3N, Cu_3N, and NiCu offered the catalyst more active sites (**Figure 16f**). The electrocatalytic activity of TMN/alloy hybrids (η_{100} = 149 mV, Tafel slope 55 mV dec^{-1}) was better than the TMN/M composites with the single metal compound (**Figure 16g** and **h**). Surprisingly, the NC-NiCu-NiCuN also exhibited outstanding activities for OER, and it only took 1.56 eV to deliver 10 mA cm^{-2} water splitting current (**Figure 16i**). The superior catalytic performance could be ascribed to the improved electrical conductivity and enhanced accessibility of the active sites.

Apart from TMN/M and TMN/alloy hybrids, combining TMN with other electroactive TMXs (i.e., TMOs,[81, 203] TMCs[203]) also manifests talented potentials. Take CeO_2 as an example, Sun et al. found that the Ni_3N-CeO_2/TM nanohybrids performed better than CeO_2/TM, Ni_3N/TM,[81] and NiO-CeO_2/TM, with a low overpotential (η_{10} = 80 mV) and a small Tafel slope (122 mV dec^{-1}). Further study indicated that the incorporation of CeO_2 could refine the electrical conductivity and interfacial synergy between Ni_3N and CeO_2.

View Article Online
DOI: 10.1039/C9TA03220G

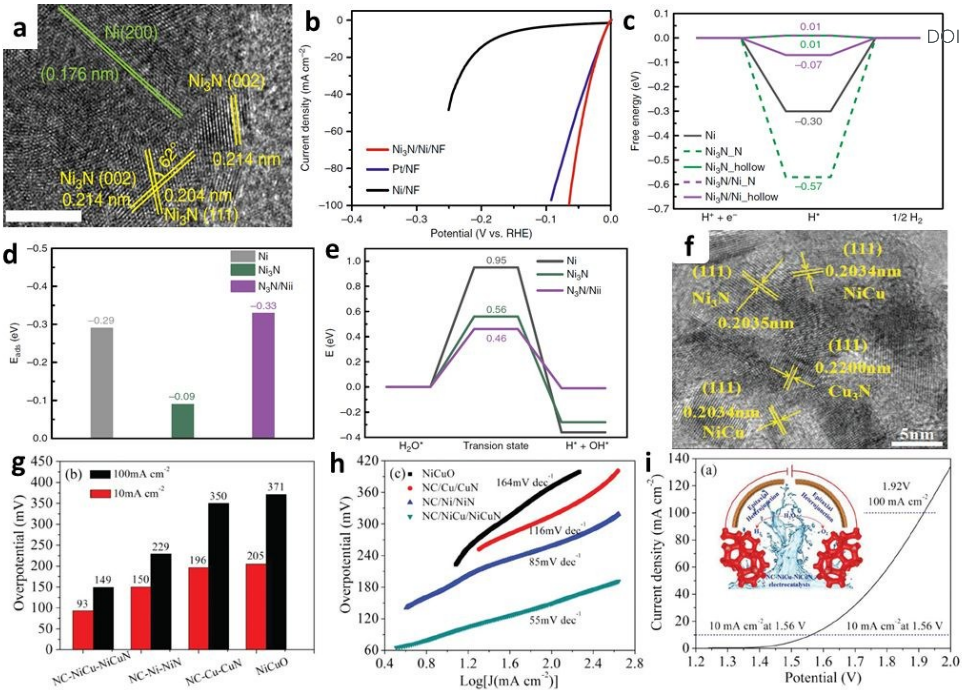

Figure 16. (a) HRTEM image of Ni$_3$N/Ni interface. Scale bar, 5 nm. (b) Linear sweep voltammetry (LSV) curves of Ni$_3$N/Ni/NF, Ni/NF, and optimized Pt/NF (Pt/C: 2.5 mg cm^{-2}) for HER in 1.0 M KOH with the current density normalized by the geometric electrode area. (c) Hydrogen adsorption free energy (ΔG_{H*}) on Ni, Ni$_3$N, and Ni$_3$N/Ni. (d) Adsorption energy of water on Ni, Ni$_3$N, and Ni$_3$N/Ni. (e) Energy barrier for water dissociation on Ni, Ni$_3$N, and Ni$_3$N/Ni. (a- e). Reproduced with permission.[79] Copyright 2018, Nature Publishing Group. (f) TEM images of NC-NiCu-NiCuN nanowires. (g) Overpotentials at 10 and 100 mA cm^{-2}. (h) Tafel slopes of NiCuO, NC-Cu-CuN, NC-Ni-NiN, and NC-NiCu-NiCuN electrodes. (i) Overall-water-splitting performance of NC-NiCu-NiCuN array with two-electrode configuration. (f- i). Reproduced with permission.[80] Copyright 2018, Wiley-VCH.

3.4.2 Transition metal phosphides

Transition metal phosphides (TMPs) are the most extensively spotlighted candidates for alkaline HER because of their impressive catalytic performance and low cost. The origin of their excellent catalytic activities mainly due to the electronic features of P. Phosphorus atoms in TMPs can extract electrons from the neighbouring transition metals due to the high electronegativity. The negatively charged P atoms can trap the positively charged proton as a base.[157] Therefore, the presence of P atoms leads to the moderate bonding with the reaction intermediates/products over the catalyst surface.[16] Thus, TMPs typically possess higher electrocatalytic activities than TMXs with other anions.[212] In

View Article Online
DOI: 10.1039/C9TA03220G

this part, the application features, as well as effective strategies to boost the catalytic activity of TMPs in alkaline HER, will be discussed.

Single TM-based phosphides are the most reported TMPs. To date, Co_xP_y, Ni_xP_y, Fe_xP_y, Mo_{xPy}, Cu_xP_y, and W_xP_y have shown great activities to HER in basic media. Interestingly, the high conductive 2D TMP monolayer and corresponding oxidized counterpart are predicted as promising HER catalysts based on the DFT computations.[213] Among a series of calculated TMPs, Mo_2P-2H and Fe_2P-2H have a favourable ΔG_H which indicates a better HER performance, which is further verified by the experiment that these catalysts indeed exhibit high-performance in HER. Therefore, the advanced DFT calculations are great indicators for discovering innovative electrocatalysts for HER.

It is suggested that the variation of component can alter the catalytic performance of TMPs significantly because of the different roles of different elements. For example, Liu et al. designed a series of Ni_xP_y micro-spheres,[82] and the catalytic properties of $Ni_{90}P_{10}$ were the best among the as-prepared TMPs (**Figure 17a-b**). Further study revealed that the ΔG_{H*} of $Ni_{90}P_{10}$ was the smallest (**Figure 17c**), which well supported the experimental results. The high P ratio can lead to favourable bonding strength of reaction intermediates/products with catalyst surfaces which indicates a better HER performance.

Beyond single TM-based phosphides, bimetallic phosphides own better activities for alkaline HER. Taking advantages of the synergistic effects of bimetallic sites with modulated electronic configurations and structural flexibility, bimetallic phosphides performed better than the single TM-based phosphides.[29, 83] Among all the reported bimetallic phosphides (e.g., CoFeP,[214, 215] NiCuP,[84] NiCoP,[29, 83, 216-218] NiMoP[33, 85]),

View Article Online
DOI: 10.1039/C9TA03220G

NiCoP is the most frequently documented one. Recently, Mo et al. designed bimetallic $Ni_{2-x}Co_xP$ catalysts by electrospinning and pyrolysis (**Figure 17d**).[83] They found that the $Ni_{0.67}Co_{1.33}P$/N-C exhibited the best catalytic activity (i.e., the smallest η_{10}, the lowest Tafel slope, and the highest ECSA) over other NiCoPs with different Ni/Co ratios (**Figure 17e** and **f**). Furthermore, the computational results stated that the regulated electronic structure resulted in the boosted hydrogen binding and the improved alkaline HER kinetics. More discussion involves this topic can be referred to a previous review.[16]

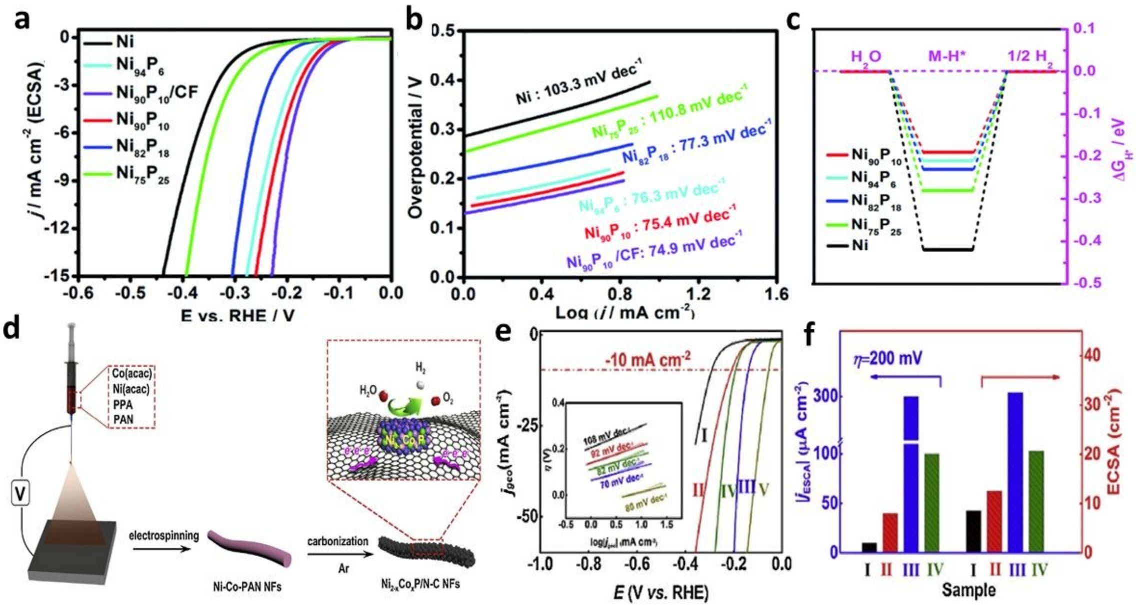

Figure 17. (a) LSV curves and (b) the corresponding Tafel plots for Ni, $Ni_{94}P_6$, $Ni_{90}P_{10}$, $Ni_{82}P_{18}$, and $Ni_{75}P_{25}$ on Ti and $Ni_{90}P_{10}$ on CF. (c) H adsorption free energy of $Ni_{90}P_{10}$ and Ni. (a- c). Reproduced with permission.[82] Copyright 2018, The Royal Society of Chemistry. (d) Schematic illustration for the fabrication of $Ni_{2-x}Co_xP$/N-C NFs. (e) Polarization curves and (f) corresponding ECSA and j_{ECSA} at η=200 mV of phosphide-modified GCEs in 1.0M KOH, along with that of commercial 40% Pt/C (I: $Ni_{1.67}Co_{0.33}P$/N-C, II: $Ni_{1.00}Co_{1.00}P$/N-C, III: $Ni_{0.67}Co_{1.33}P$/N-C, IV: $Ni_{0.33}Co_{1.67}P$/N-C, V: 40% Pt/C). (d- f). Reproduced with permission.[83] Copyright 2019, Elsevier Ltd.

Doping becomes an efficient approach to upgrade the capability of TMPs. For TMPs, the dopants can be metals, non-metals, as well as both of them. It is highly suggested that the alkaline HER process can be affected by the atomic type and/or the exposed crystal phase of the catalyst.[219] Hence, the dopants can have distinguishable impacts on the

View Article Online
DOI: 10.1039/C9TA03220G

catalytic behavior of TMPs. Firstly, metal doping has prominent influence on the electronic structure, stability and surface properties of TMPs, resulting in a better catalytic performance. For example, Chu et al. designed a Cu-doped Ni_2P with the NiCu layered double hydroxide as a precursor (**Figure 18a**).[84] Experimental results implied that the $Ni_{1.8}Cu_{0.2}$-P/NF just required a small overpotential of 78mV to reach a current density of 10 mA cm^{-2} and a low Tafel slope of 70 mV dec^{-1} for the HER in 1.0 M KOH (**Figure 18b** and **c**). DFT study indicated that the Cu doping tuned the electronic structure of the Ni_2P by offering extra electrons in the valence band and near Fermi surface of $Ni_{1.8}Cu_{0.2}P$ to raise the Fermi level to a higher energy level (**Figure 18d**). Also, the calculated ΔG_{H*} of $Ni_{1.8}Cu_{0.2}P$ (-0.282 eV) and Ni_2P (-0.607 eV) signified that Cu doping decrease the energy barrier for HER (**Figure 18e**). Lately, anions doping demonstrate great potentials in upgrading the catalytic activity of TMPs. Inspired by the impressive role of metal oxides and hydroxides in water dissociation and adsorption of hydrogen intermediates, oxygen has been recognized as an ideal dopant to ameliorate the catalytic ability of TMPs. Zhang and co-workers fabricated oxygen-incorporated $NiMoP_2$ nanowire arrays on the Ni foam substrate.[85] Surprisingly, the as-prepared O-$NiMoP_2$/Ni manifested a geometrical catalytic current density of 10 mA cm^{-2} at a low overpotential of 31 mV with a Tafel slope of 62.11 mV dec^{-1}. The theoretical calculations revealed that oxygen incorporation not only improved the interaction between H* and metal atoms toward a more favourable calculated ΔG_{H*}, but remarkably promoted H_2O adsorption. Similarly, the role of N in the N-Co_2P/CC is almost the same as O. Men et al. found that N doping could tune the electronic structure of Co_2P, resulting in optimised adsorption free energies of water (ΔG_{H2O*}) and hydrogen (ΔG_{H*}), facilitating alkaline HER through the Volmer-Heyrovsky process.[86]

Based on the benefits of both metal and non-metal doping strategies, the dual-doping approach also evoked increasing interests among the researchers. For instance, Xu et al. recently developed new oxygen and copper co-doped CoP nanowire array electrode by a low-temperature phosphatization method.[87] They found that the lattices of the co-doped sample became curvy and locally distorted (**Figure 18f**), which would induce more exposure of surface active sites. The alkaline HER performance of prepared samples signified that the co-doped catalysts were better than the un-doped CoP and the oxygen-doped CoP (**Figure 18g** and **h**). The calculated free energy diagram indicated that both the water adsorption energy and the Gibbs free energy of hydrogen adsorption of O, Cu-CoP were lower than those of CoP (**Figure 18i**). The enhancement is due to the co-incorporation of oxygen and copper atoms in CoP, which results in the exposure of more active sites and optimization of activated water dissociation energy, as well as binding free energy of H* intermediates. To date, most of the reported catalysts are single doped, so more efforts are encouraged to explore the optimal categories and dosages of co-dopants to attain desirable catalysts.

View Article Online
DOI: 10.1039/C9TA03220G

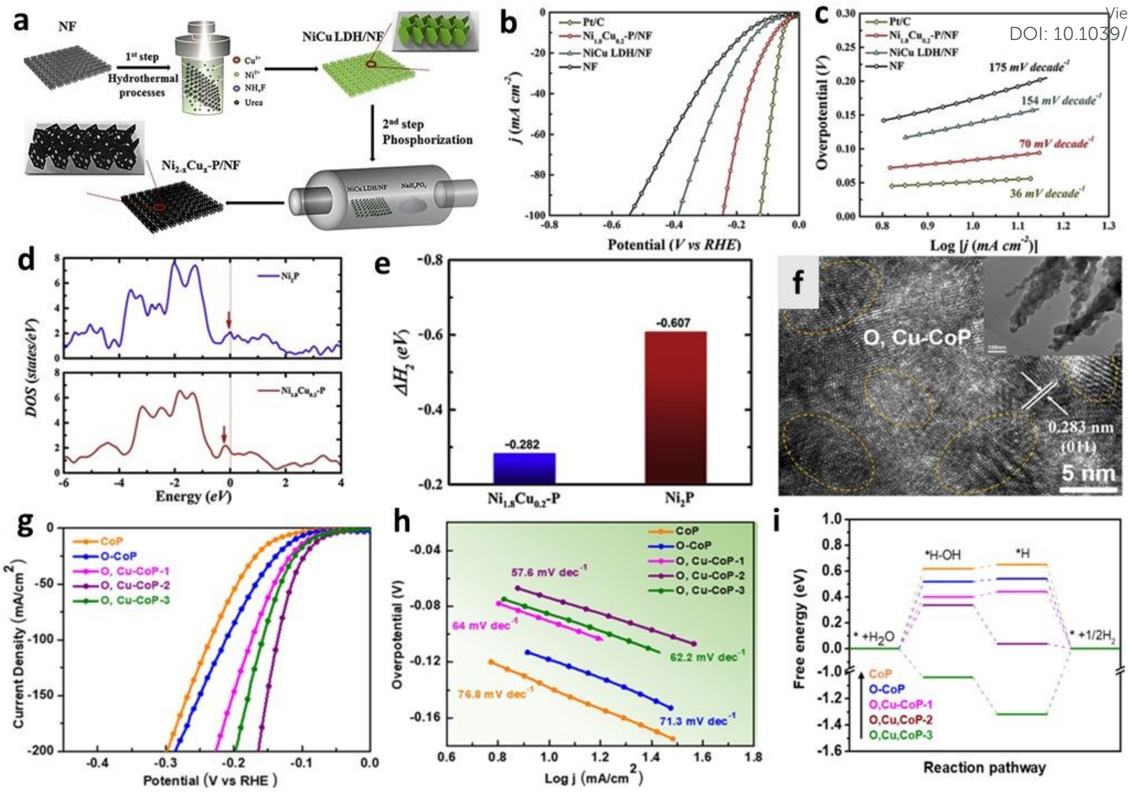

Figure 18. (a) Process steps in the synthesis of high-performance $Ni_{2-x}Cu_x$-P electrocatalysts. (b) Polarization curves of HER and (c) corresponding Tafel plots derived from the polarization curves. (d) Calculated DOS for Ni_2P and $Ni_{1.8}Cu_{0.2}$-P. (e) HER free-energy change of Ni_2P doped with Cu. (a- e). Reproduced with permission.[84] Copyright 2019, Elsevier Ltd. (f) HRTEM images of O, Cu-CoP. Inset: Corresponding TEM images. The circles indicate the lattice distortion. (g) IR-corrected polarization curves and (h) Tafel plots of the O, Cu-CoP nanowire, O-CoP nanowire, CoP nanowire electrodes, and bare carbon cloth in 1 M KOH electrolyte with Ag/AgCl as the reference electrode and a graphite bar as the counter electrode. (i) HER diagram on the (011) surface of clean CoP and oxygen- and copper-doped CoP. (f- i). Reproduced with permission.[87] Copyright 2018, American Chemical Society.

Theoretically, the hybrid materials would inherit the merits of each component and may manifest new features due to the coupling effect, thus demonstrating higher electrocatalytic activities than the single components. To date, novel composites of TMPs/C (i.e. $Ni_{2-x}Co_xP$/N-C NFs,[83] CQDs/MoP,[220] Co_2P@NPC/CC,[221] MoP/CNT,[222] Ni_2P@NPCNFs,[223] Ni_2P@PCG,[224] Ru_2P/RGO[225]), TMPs/Ms (i.e. Co/CoP,[226, 227] Cu@Cu_3P,[228] Ni@Ni_2P-Ru[88]) and TMPs/TMXs (i.e. $V_4P_{6.98}$/VO$(PO_3)_2$,[229] Ni_3S_2/Ni_2P,[230] CoP/CeO_2,[127] CoP(MoP)-$CoMoO_3$@CN,[231] Ni_2P/Fe_2P,[232] FeP/Ni_2P,[89] MoC-MoP/BCNC NFs,[233] CoP/Mo_2C-NC[92]) have exhibited superb potentials for alkaline HER.

In this part, representative catalysts of TMPs/Ms and TMPs/TMXs will be discussed. Recently, Liu et al. fabricated a unique multi-heterogeneous Ni@Ni_2P-Ru nanorod with a simple one-pot synthetic strategy (**Figure 19a**).[88] The as-prepared hybrids contained Ni_2P, Ni and Ru phases (**Figure 19b**), and the introduced Ru could regulate the phosphating process of Ni by a Ru-Ni coordination effect to obtain Ni@Ni_2P-Ru heterogeneous nanorods. Surprisingly, the electrocatalytic activity of Ni@Ni_2P-Ru was comparable to that of Pt/C (20 wt.%), with a low overpotential (η_{10} = 31 mV) and a small Tafel slope (41 mV dec^{-1}) (**Figure 19c** and **d**). Additionally, the DFT calculations revealed that Ru sites improved the H adsorption/desorption behaviors over Ni_2P (**Figure 19e**). In another study, Yu et al. prepared a TMP/TMP (FeP/Ni_2P) hybrid by a simple thermal treatment process.[89] Numerous FeP and Ni_2P nanocrystals were distributed uniformly on the surface, forming abundant active sites on the catalyst (**Figure 19f** and **g**). The obtained hybrids showed higher electrocatalytic capability (η_{10} = 14 mV, Tafel slope 24.2 mV dec^{-1}) than the corresponding single components, even the Pt electrode (**Figure 19h** and **i**). Compared to Ni_2P, FeP/Ni_2P possessed a much higher C_{dl}, suggesting that the hybrids owned a high active surface area (**Figure 19j**). In-depth DFT investigations revealed that the introduction of FeP could significantly reduce the ΔG_{H*} on Ni_2P surface(**Figure 19k**), which further supported the experimental results. Surprisingly, FeP/Ni_2P also presented marvelous potentials for OER, and it only took a very low cell voltage of 1.42 V to afford 10 mA cm^{-2} for overall water splitting (**Figure 19l**). Thus, low-cost and high-performance hybrids hold great potential for large-scale applications.

View Article Online
DOI: 10.1039/C9TA03220G

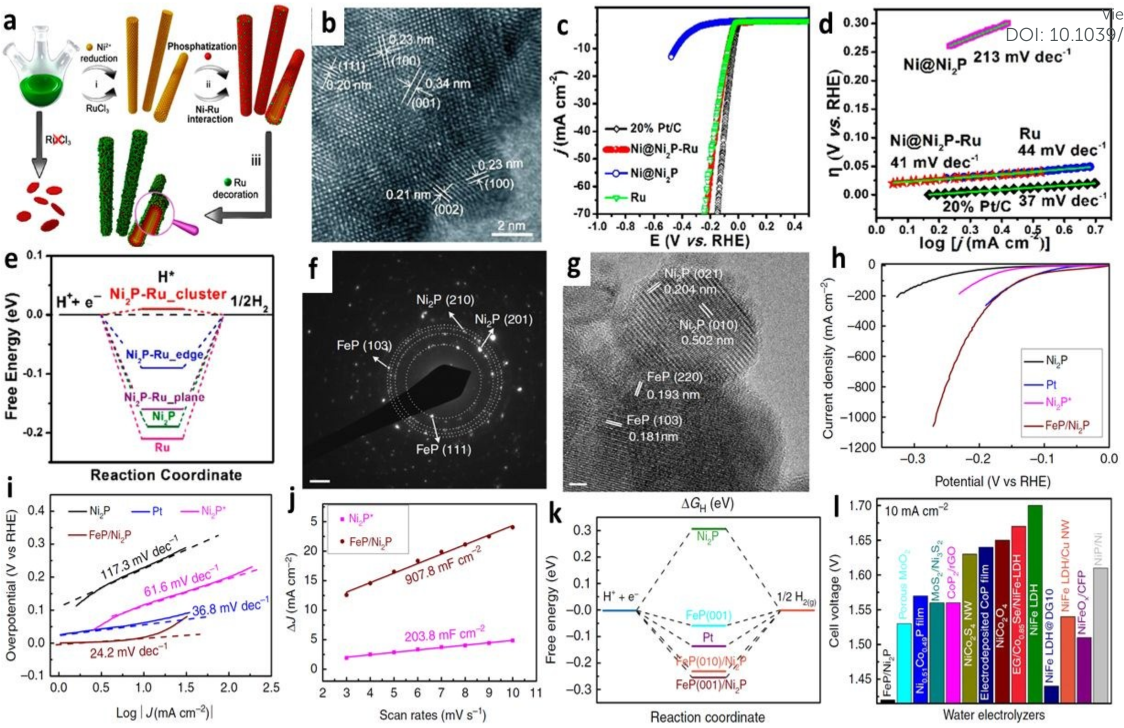

Figure 19. (a) Schematic illustration of the formation of Ni@Ni$_2$P-Ru HNRs. (2) HRTEM image of Ni@Ni$_2$P-Ru. (c) LSV HER curves (scan rate: 5 mV s^{-1}) and (d) Tafel plots of the different catalysts in 1.0 M KOH. (e) Computed free energy diagram of HER. (a- e). Reproduced with permission.[88] Copyright 2018, American Chemical Society. (f) The SAED pattern taken from the FeP/Ni$_2$P catalysts. Scale bar, 2 1/nm. (g) A typical HRTEM image taken from the FeP/Ni$_2$P catalysts. Scale bar, 2 nm. (h) The HER polarization curves of different catalysts. (i) The relevant Tafel plots. (j) Double-layer capacitance measurements for determining electrochemically active surface areas of Ni$_2$P and FeP/Ni$_2$P electrodes. (k) Free energy diagram for ΔG_H, the hydrogen adsorption free energy at pH= 14 on FeP/Ni$_2$P catalyst in comparison with Ni$_2$P and benchmark Pt catalysts. (l) Comparison of the cell voltages to achieve 10 mA cm^{-2} among different water alkaline electrolyzers. (f- l). Reproduced with permission.[89] Copyright 2018, Nature Publishing Group.

3.5 Transition metal carbides

Transition metal carbides (TMCs) have shown impressive catalytic performance towards alkaline HER thanks to their noble-metal-like electronic structures, structural robustness, and earth abundance.[234] The *d* orbitals of M atoms will be broadened with the help of *s*- and *p*- orbitals of C atoms, thus forming a similar Pt *d*-band state.[235] Recently, TMCs like Mo$_x$C$_y$,[23, 235, 236] W$_x$C$_y$,[237, 238] V$_x$C$_y$,[39, 239] and Ni$_x$C$_y$[240] have been applied in alkaline HER, especially Mo$_2$C. An informative summary can be found in the latest review.[235]

Despite these advantages, the relatively poor conductivity of TMCs requires a highly conductive substrate. In most cases, carbon materials function well and can promote the electrocatalytic properties. Lately, Wei et al. prepared a Mo_2C/G-NCS (graphene wrapping N-doped porous carbon microspheres) catalyst by a two-step process.[25] The ultrafine nanoparticles with a size about 4 nm were embedded into the carbon matrix. The designed porous structure enhanced the electrode-electrolyte contact points and the charge transfer process. The XPS results indicated the presence of graphitic N, pyridinic N, and Mo-N. The pyridinic N was the primary N species to benefit the HER process. The formation of Mo-N bonds implied that N atoms were doped into Mo_2C, and this electron-rich dopant could downshift the density of empty *d*-band in Mo_2C, thus weakening the Mo-H strength. Similar phenomena were also reported in other studies.[24, 241, 242] The electrochemical tests indicated that the Mo_2C/G3-NCS750 sample possessed an outstanding alkaline HER activity ($\eta_{10} = 66$ mV, Tafel slope 37 mV dec^{-1}). Therefore, graphene wrapping, good conductivity, the well-defined porous microspherical structure, ultrafine Mo_2C nanocrystal, and regulated Mo-H strength all benefit the alkaline HER process.

Other sophisticated methods are also efficient to promote the catalytic performance of TMCs, such as heteroatom doping and hybridizing with TMXs. In doping strategies, the universally employed dopants include N,[24, 243] P,[244, 245] Ni,[246] and the combinations of these single elements.[90, 246] Recently, Ji and co-authors prepared N, P-codoped Mo_2C/MoC nanofibers via pyrolysis of phosphomolybdic acid-doped polyaniline nanofibers.[90] Further experimental results indicated electron transfer from Mo to P and N. Specifically, for Mo_2C, the charge migration can enhance H adsorption onto Mo sites, whilst for MoC, the N and P act as the basic sites to trap positively protons and mediate proton transfer to the adjacent Mo sites to boost the HER process.

TMCs/TMXs hybrids, such as Mo/Mo_2C,[93] Co/β-Mo_2C,[247] MoO_2/α-Mo_2C,[22] Mo_2N/Mo_2C,[91, 241, 248] Mo_2C/Mo_3Co_3C,[249] MoC/Mo_2C,[234, 250] and Mo_2C/CoP[92] all exhibited appealing electrocatalytic activities for alkaline HER. In a recent study, Yan et al. applied an *in situ* catalytic etching method to prepare a Mo_2N-Mo_2C heterostructure.[91] Many holes were spotted to present adjacent to nanoparticles, and intimate contacts of Mo_2C with Mo_2N were identified by the HRTEM image in **Figure 20a** and **b**. The shift in XPS results further confirmed the electron transport between Mo_2C and Mo_2N, which benefited the catalytic reaction (**Figure 20c**). The obtained Mo_2N-Mo_2C/HGr-3 sample delivered a magnificent catalytic performance (η_{10} = 154 mV, Tafel slope 68 mV dec^{-1}) and good durability. DFT calculations implied that N atoms at the interface of N-Mo-C should be the dominant active sites in the Mo_2N-Mo_2C hybrid because of the smallest ΔG_{H*} of 0.046 eV (**Figure 20d**). Analogously, interfaces in catalysis is also highlighted in other reports, which outperforms the catalytic properties of each part in the heterojunction. For example, Luo et al. suggested that the catalytic performance of CoP/Mo_2C-NC was better that CoP and Mo_2C-NC.[92] The main reason was that the electron cloud transferred from Co to Mo through Co-P-Mo bonds, resulting in the generation of high valence state for Co^{3+} species and the low valence states for Mo^{2+} and Mo^{3+} species, providing rich active sites for alkaline HER. Interestingly, Xiong et al. unveiled that the Mo/Mo_2C heterointerfaces could not only supply an platform to gather the double-phase interface consisted of catalytic sites (exposed β-Mo_2C defects) and the electron-transfer channel (metallic Mo), but also optimize the intrinsic binding energy between H_{ads} and catalyst surface.[93] Thus, the Mo/Mo_2C hybrid exhibited superior alkaline HER activities (η_{10} = 79 mV, Tafel slope 62.86 mV dec^{-1}) than the sole Mo and β-Mo_2C.

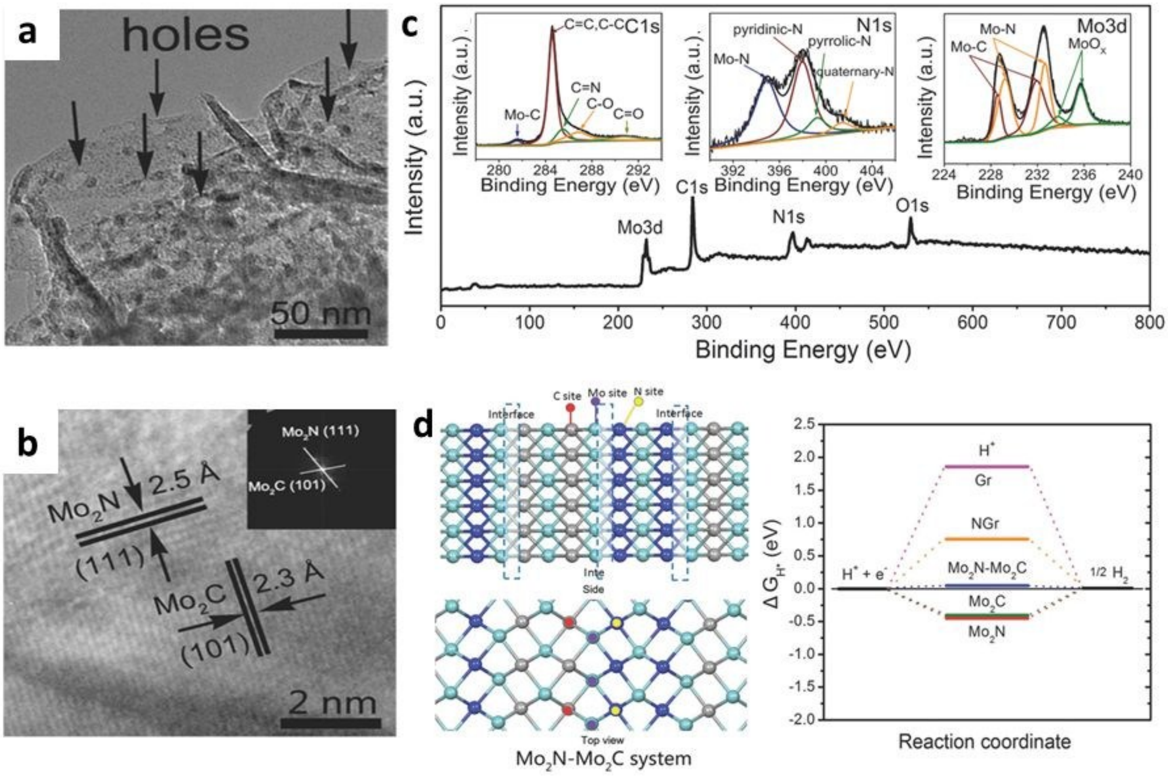

Figure 20. (a) Magnified TEM image, (b) HRTEM image (inset: FFT of Mo_2N and Mo_2C), and (c) XPS survey spectrum of the Mo_2N-Mo_2C/HGr-3 hybrid. (d) Possible adsorption sites of H* on the Mo_2N-Mo_2C system and calculated free-energy diagram for HER based on the various studied systems. Reproduced with permission.[91] Copyright 2018, Wiley-VCH.

3.6 Transition metal borides

Transition metal borides (TMBs) have been extensively exploited as active catalysts for OER, while their performance in HER is seldom documented. Recently, the good electrocatalytic abilities of TMBs have attracted enormous attention, and Mo_xB_y,[251] Ni_xB_y,[94, 252, 253] Co_xB_y,[254] Fe_xB_y,[255] Ru_xB_y,[256] etc. have been applied in alkaline HER. It is suggested that the coupling interactions between *s*-, *p*- orbitals of B and *d*- orbitals of M can regulate the *d*-orbitals center of TMBs downshift away from the Fermi level (**Figure 21a**), thus obtaining an optimized M-H affinity and promoted HER

View Article Online
DOI: 10.1039/C9TA03220G

performance.[256] Li et al. studied the catalytic trends of 12 TMBs,[256] from Group IV B to Group VIII metal diborides. The computational results indicated that the *d*-band center of TMBs was a good descriptor of the HER activity. A generally linear relationship can be established between the *d*-band center and the absolute value of ΔG_{H*} (**Figure 21b**). The experimental results were in line with the DFT calculations (**Figure 21c**), and the catalytic properties of RuB_2 were better than those of Pt/C (20 wt.%) in 1 M KOH. In addition, the activation energy of water dissociation step on RuB_2 (001) plane was lower than that on Pt (111) surface (0.64 eV vs. 0.85 eV), revealing a more favourable kinetic process for RuB_2 (**Figure 21d**). Therefore, the theoretical and experimental study figured out the importance of rationally tailoring the electronic structure of TMBs on regulating their catalytic activities.

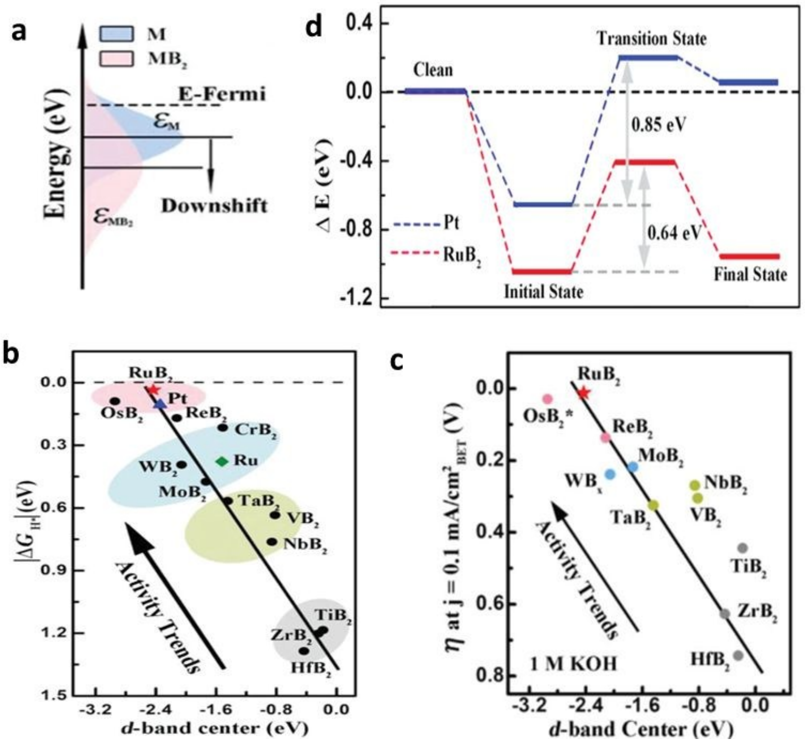

Figure 21. (a) Schematic explanation of the boron effect on the d-bands of metal. ε_M and ε_{MB2} represent *d*-band centers of metal and metal diboride, respectively. (b) A fitted linear relationship between hydrogen adsorption free energy (ΔG_{H*}) and *d*-band center of MB_2, Pt, and Ru. (c) A fitted linear relationship between the measured overpotential and *d*-band center at a current density of 0.1 mA cm^{-2} (normalized by BET surface area) in 1.0

View Article Online
DOI: 10.1039/C9TA03220G

M KOH solution. (d) Reaction pathways for water molecule dissociation on the RuB_2 (001) and Pt (111) surfaces. Reproduced with permission.[256] Copyright 2018, Wiley-VCH.

It is worth mentioning that amorphous TMBs are inevitably oxidized when exposed to air and water, thus forming oxides/hydroxides on the surface.[94, 252, 254, 257] The presence of oxides/hydroxides can benefit the alkaline HER process. For instance, Chen et al. fabricated the Ni_xB/f-MWCNT hybrid by a room-temperature approach (**Figure 22a**).[94] The XPS peak of B-O confirmed that the surface oxidation of Ni_xB, the Ni-O bonds originated from the interactions of Ni_xB with the O-containing functional groups on the MWCNT surface. The O 1s spectra (C-O-Ni) also marked a strong coupling effect by the oxygen bridge (**Figure 22b-d**). Electrochemical tests illustrated that Ni_xB/f-MWCNT possessed higher catalytic activities (η_{10} = 116 mV, Tafel slope 70.4 mV dec^{-1}) than Ni_xB, f-MWCNT, and their mechanical mixture (**Figure 22e** and **f**). Additionally, the Ni_xB/f-MWCNT owned better stability than Pt for alkaline HER (**Figure 22g**). The XPS results of the Ni_xB/f-MWCNT sample after the 100-hour HER test indicated the formation of $Ni(OH)_2$ on the catalyst surface (**Figure 22h**). Totally, the $Ni(OH)_2/Ni_xB$ hybrids worked as the active component. The superb activity of $Ni(OH)_2$ for water dissociation and H*/OH* adsorption could significantly improve the catalytic performance of Ni_xB/ f-MWCNT. Accordingly, partial oxidation can be utilized as a facile strategy in the design of high-performance TMBs catalysts.

Apart from mono-metal borides, ternary borides also exhibit impressive catalytic performance. The introduction of a secondary metal/non-metal element can enhance the catalytic HER activity because of the regulated electronic structure and synergistic effect.[258] Hitherto, Co-Mo-B,[258, 259] Co-Ni-B,[257, 260] Co-W-B,[261] and Co-B-P[262] have shown decent catalytic properties towards HER in basic media.

View Article Online
DOI: 10.1039/C9TA03220G

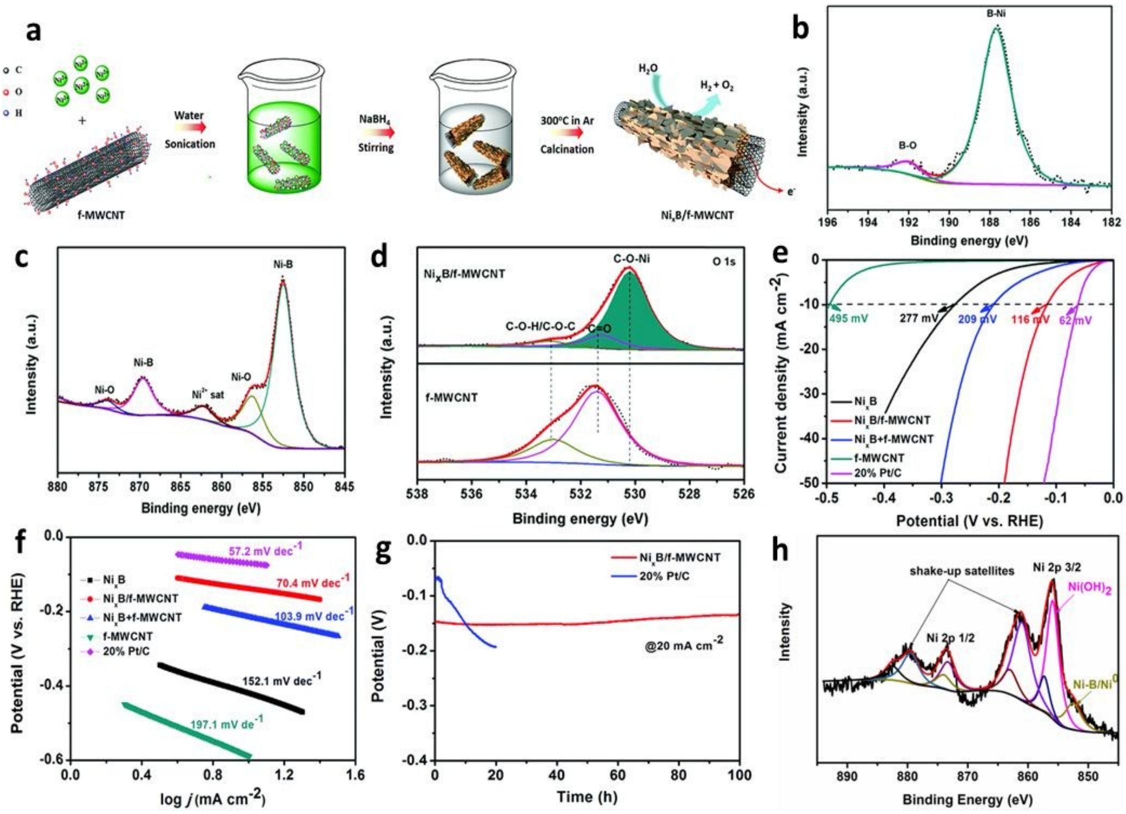

Figure 22. (a) Schematic of the synthesis of Ni$_x$B/f-MWCNT bifunctional electrocatalysts. Core-level XPS spectra of Ni$_x$B/f-MWCNT (b) B 1s spectrum of Ni$_x$B/f-MWCNT, (c) Ni 2p spectrum of Ni$_x$B/f-MWCNT, (d) O 1s spectra of f-MWCNT and Ni$_x$B/f-MWCNT. (e) Polarization curves and (f) corresponding Tafel plots of Ni$_x$B/f-MWCNT, Ni$_x$B, Ni$_x$B + f-MWCNT, f-MWCNT, and commercial 20 wt% Pt/C catalysts in 1 M KOH electrolyte. (g) HER chronopotentiometry curves of Ni$_x$B/f-MWCNT and Pt/C under the current density of 20 mA cm^{-2} over 100 hours of operation. (h) Core-level XPS spectra near the region of Ni 2p of Ni$_x$B/f-MWCNT after the 100-hour HER test in H$_2$-saturated 1 M KOH electrolyte under the current density of 20 mA cm^{-2}. Reproduced with permission.[94] Copyright 2018, The Royal Society of Chemistry.

Apart from those aforementioned strategies mainly focus on enhancing the intrinsic catalytic activity of the catalysts, constructing porous nanostructures has also been proved to be an efficient strategy for enhancing the catalytic performance of the catalysts.[263-267] Generally, a porous structures can increase the specific surface area with the maximum exposed active sites and provide more electrolyte-electrode contact points.[24] Additionally, the unique architecture facilitate the charge transfer, and improve the mass transportation/diffusion during the alkaline HER process.[263, 268] For instance, Hao et al. developed a simple electroless plating process to fabricate a Co-B/Ni catalyst with a unique porous nodule structure and abundant internal spaces for catalytic reactions.[95] Further experimental results indicated that the HER activity decay was highly relevant to the decrease and blockage of internal pores, which verified the importance of the porous architecture. Meanwhile, the porous structure guarantees good mechanical adhesion and provides enormous vent channels for the gaseous product (H_2). Therefore, the porous structures of TMBs play a key role in the enhancement of electrocatalytic performance in HER.[94, 257, 262, 269, 270]

4. Concluding Remarks and Outlook

Nowadays, tremendous research enthusiasms dedicated to advancing the technology for hydrogen production, especially the water splitting in alkaline electrolytes. Therefore, it is of critical significance to create sufficient low-cost electrocatalysts to substitute noble metals. In this regard, TM-based materials hold impressive potentials. In this review, we summarise the recent progress on TM-based electrocatalysts for the alkaline hydrogen evolution reaction. According to their featured anions, 1) TMs; 2)TM alloys; 3) oxygen group TM-based catalysts (TMOs, LDHs, TMSs, TMSes, and TMTes); 4) nitrogen group TM-based catalysts (TMNs, TMPs); 5) TMCs; and 6) TMBs are comprehensively presented. We also highlight the mainstream strategies to upgrade the catalytic properties of each TMX. These state-of-the-art strategies aim at the following three goals: 1) improving the inherent catalytic activity by component regulation, defect (vacancy) engineering, doping, phase engineering, facet engineering, and hybridizing (interface engineering), etc.; 2) enriching active sites through nanosizing, designing dimensional architectures (0-3D), and hierarchical/porous structuring, etc.; 3) enhancing conductivity with the assistance of highly conductive substrates, such as graphene, Ni foam, and carbon materials. For a typical kind of TMX, selected strategies are highlighted in this review, but all of the aforemented strategies are effiective for all category of TMXs in constructing high-performance electrocatalysts.

To date, although remarkable progress has been achieved in the development of respectful electrocatalysts for alkaline HER, there are still some issues that deserve further explorations. Firstly, the design of novel electrocatalysts requires novel strategies to transform the mediocre materials into a high-performance catalyst through increasing the number of active sites and improving the conductivity, intrinsic activity, as well as durability. The "all-in-one" strategy offers the pristine material impressive catalytic properties. Nevertheless, how to assemble the related approaches logically is a key issue, which needs more efforts. In addition, computational methods can provide valuable guidelines to rapidly discover novel catalysts for alkaline HER. Combining experimental tests and computational results will improve the research efficiency and avoid the time-consuming trial-and-error route.[271] Another vital factor should be considered is the catalyst preparation procedures, where the reaction time and temperature, safety issues, and environmental consequences should be carefully evaluated.

Secondly, the catalytic mechanisms of alkaline HER require more in-depth investigations. The *In situ* and operando spectroscopic and microscopic techniques are highly recommended to understand the catalytic phenomena at the catalyst surface region. Moreover, DFT calculations are valuable tools to unveil the catalytic processes at the atomic scale. The computational results can provide significant information about reaction energetics, reaction routes, intermediate evolution, and charge distributions etc. Additionally, the theoretical calculation plays a critical role in prediction and explanation of the catalytic performance of the designed materials. Under this circumstance, the rational design of model catalyst by DFT studies is an important step to match and guide the real catalysts in HER processes.

Thirdly, parameters for catalysts evaluation should be further standardized. To date, overpotentials at 10 mA cm^{-2} (η_{10}) and Tafel slope are the most popular descriptors and used by almost all the reported papers. However, other factors are often documented randomly, such as the specific/mass activity, turnover frequency, stability, and onset potential. These issues result in unfair performance comparisons among different catalysts. Additionally, mass loading has a major influence on the evaluating parameters.

Finally, it is surprising to find that many of HER electrocatalysts reported above are great candidates for OER and/or oxygen reduction reaction (ORR). These multifunctional catalysts can further decrease the running cost and facilitate the experimental setups in overall water splitting and batteries. Hence, it is of great significance to analyse the origins of versatile abilities and offer valuable guidance for the design of future high-performance electrocatalysts.

Acknowledgments

This work is supported by the Australian Research Council (ARC) Future Fellowship (FT160100195). Mr. Zhijie Chen acknowledges the China Scholarship Council (CSC) for the scholarship support.

References

1. Z. W. Seh, J. Kibsgaard, C. F. Dickens, I. Chorkendorff, J. K. Norskov and T. F. Jaramillo, *Science*, 2017, **355**, eaad4998.

View Article Online
DOI: 10.1039/C9TA03220G

2. T. Li, G. Luo, K. Liu, X. Li, D. Sun, L. Xu, Y. Li and Y. Tang, *Adv. Funct. Mater.*, 2018, **28**, 1805828.
3. J. Wei, M. Zhou, A. Long, Y. Xue, H. Liao, C. Wei and Z. J. Xu, *Nanomicro Lett*, 2018, **10**, 75.
4. M. Gong, D.-Y. Wang, C.-C. Chen, B.-J. Hwang and H. Dai, *Nano Res.*, 2015, **9**, 28-46.
5. Y. Wang, L. Chen, X. Yu, Y. Wang and G. Zheng, *Adv. Energy Mater.*, 2017, **7**, 1601390.
6. Y. Shen, Y. Zhou, D. Wang, X. Wu, J. Li and J. Xi, *Adv. Energy Mater.*, 2017, **8**, 1701759.
7. N. Mahmood, Y. Yao, J. W. Zhang, L. Pan, X. Zhang and J. J. Zou, *Adv. Sci. (Weinh)*, 2018, **5**, 1700464.
8. B. Ruqia and S. I. Choi, *ChemSusChem*, 2018, **11**, 2643-2653.
9. T. Wang, X. Wang, Y. Liu, J. Zheng and X. Li, *Nano Energy*, 2016, **22**, 111-119.
10. F. Safizadeh, E. Ghali and G. Houlachi, *Int. J. Hydrogen Energy*, 2015, **40**, 256-274.
11. K. Zeng and D. Zhang, *Prog. Energy Combust. Sci.*, 2010, **36**, 307-326.
12. Y. Zheng, Y. Jiao, A. Vasileff and S. Z. Qiao, *Angew. Chem. Int. Ed. Engl.*, 2018, **57**, 7568-7579.
13. J. Mohammed-Ibrahim and X. Sun, *J. Energy Chem.*, 2019, **34**, 111-160.
14. B. Xiong, L. Chen and J. Shi, *ACS Catal.,* 2018, **8**, 3688-3707.
15. N. Han, P. Liu, J. Jiang, L. Ai, Z. Shao and S. Liu, *J. Mater. Chem. A*, 2018, **6**, 19912-19933.
16. Y. Pei, Y. Cheng, J. Chen, W. Smith, P. Dong, P. M. Ajayan, M. Ye and J. Shen, *J. Mater. Chem. A,* **2018**, 6, 23220-23243.
17. X. Zhang, C. Shi, B. Chen, A. N. Kuhn, D. Ma and H. Yang, *Curr. Opin. Chem. Eng.*, 2018, **20**, 68-77.
18. M. Samadi, N. Sarikhani, M. Zirak, H. Zhang, H.-L. Zhang and A. Z. Moshfegh, *Nanoscale Horiz.*, 2018, **3**, 90-204.
19. Y. Shi and B. Zhang, *Chem. Soc. Rev.*, 2016, **45**, 1529-1541.
20. A. Li, Y. Sun, T. Yao and H. Han, *Chemistry*, 2018, **24**, 18334-18355.
21. P. Jiang, Y. Yang, R. Shi, G. Xia, J. Chen, J. Su and Q. Chen, *J. Mater. Chem. A*, 2017, **5**, 5475-5485.
22. Y. Liu, B. Huang and Z. Xie, *Appl. Surf. Sci.*, 2018, **427**, 693-701.
23. W. Yuan, Q. Huang, X. Yang, Z. Cui, S. Zhu, Z. Li, S. Du, N. Qiu and Y. Liang, *ACS Appl. Mater. Interfaces*, 2018, **10**, 40500-40508.
24. S. Jing, L. Zhang, L. Luo, J. Lu, S. Yin, P. Shen and P. Tsiakaras, *Appl. Catal., B,* 2018, **224**, 533-540.
25. H. Wei, Q. Xi, X. Chen, D. Guo, F. Ding, Z. Yang, S. Wang, J. Li and S. Huang, *Adv. Sci. (Weinh)*, 2018, **5**, 1700733.
26. Y. Liu, G. D. Li, L. Yuan, L. Ge, H. Ding, D. Wang and X. Zou, *Nanoscale*, 2015, **7**, 3130-3136.
27. X. Zhang, Z. Wu and D. Wang, *Electrochim. Acta*, 2018, **281**, 540-548.
28. S. Gao, Y. Zhang, Y. Zhang, B. Wang and S. Yang, *Small*, 2018, **14**, e1804388.
29. Z. Fang, L. Peng, Y. Qian, X. Zhang, Y. Xie, J. J. Cha and G. Yu, *J. Am. Chem. Soc.*, 2018, **140**, 5241-5247.
30. R. Zhang, X. Wang, S. Yu, T. Wen, X. Zhu, F. Yang, X. Sun, X. Wang and W. Hu, *Adv. Mater.*, 2017, **29**, 1605502.
31. M. Cao, Z. Xue, J. Niu, J. Qin, M. Sawangphruk, X. Zhang and R. Liu, *ACS Appl. Mater. Interfaces*, 2018, **10**, 35224.
32. J. X. Feng, J. Q. Wu, Y. X. Tong and G. R. Li, *J. Am. Chem. Soc.*, 2018, **140**, 610-617.
33. L. Yu, I. K. Mishra, Y. Xie, H. Zhou, J. Sun, J. Zhou, Y. Ni, D. Luo, F. Yu, Y. Yu, S. Chen and Z. Ren, *Nano Energy,* 2018, **53**, 492-500.
34. D. Voiry, M. Chhowalla, Y. Gogotsi, N. A. Kotov, Y. Li, R. M. Penner, R. E. Schaak and P. S. Weiss, *ACS Nano*, 2018, **12**, 9635-9638.
35. Y. Wang, D. Yan, S. El Hankari, Y. Zou and S. Wang, *Adv. Sci. (Weinh)*, 2018, **5**, 1800064.

36. S. Anantharaj, S. R. Ede, K. Karthick, S. Sam Sankar, K. Sangeetha, P. E. Karthik and S. Kundu, *Energy Environ. Sci.*, 2018, **11**, 744-771.
37. S. Anantharaj, S. R. Ede, K. Sakthikumar, K. Karthick, S. Mishra and S. Kundu, *ACS Catal.*, 2016, **6**, 8069-8097.
38. P. Yu, F. Wang, T. A. Shifa, X. Zhan, X. Lou, F. Xia and J. He, *Nano Energy*, 2019, **58**, 244-276.
39. W. Fu, Y. Wang, H. Zhang, M. He, L. Fang, X. Yang, Z. Huang, J. Li, X. Gu and Y. Wang, *J. Catal.*, 2019, **369**, 47-53.
40. Z.-F. Huang, J. Wang, Y.C. Peng, C.-Y. Jung, A. Fisher and X. Wang, *Adv. Energy Mater.*, 2017, **7**, 1700544 .
41. L. Wang, Y. Li, M. Xia, Z. Li, Z. Chen, Z. Ma, X. Qin and G. Shao, *J. Power Sources*, 2017, **347**, 220-228.
42. H. Jin, X. Liu, S. Chen, A. Vasileff, L. Li, Y. Jiao, L. Song, Y. Zheng and S.-Z. Qiao, *ACS Energy Lett.*, 2019, DOI: 10.1021/acsenergylett.9b00348, 805-810.
43. Q. Shao, Y. Wang, S. Yang, K. Lu, Y. Zhang, C. Tang, J. Song, Y. Feng, L. Xiong, Y. Peng, Y. Li, H. L. Xin and X. Huang, *ACS Nano*, 2018, **12**, 11625-11631.
44. W. Chen, J. Pei, C. T. He, J. Wan, H. Ren, Y. Wang, J. Dong, K. Wu, W. C. Cheong, J. Mao, X. Zheng, W. Yan, Z. Zhuang, C. Chen, Q. Peng, D. Wang and Y. Li, *Adv. Mater.*, 2018, **30**, e1800396.
45. B. Lu, L. Guo, F. Wu, Y. Peng, J. E. Lu, T. J. Smart, N. Wang, Y. Z. Finfrock, D. Morris, P. Zhang, N. Li, P. Gao, Y. Ping and S. Chen, *Nat. Commun.*, 2019, **10**, 631.
46. J. Su, Y. Yang, G. Xia, J. Chen, P. Jiang and Q. Chen, *Nat. Commun.*, 2017, **8**, 14969.
47. Q. Lv, L. Yang, W. Wang, S. Lu, T. Wang, L. Cao and B. Dong, *J. Mater. Chem. A*, 2019, **7**, 1196-1205.
48. T. Zhang, K. Yang, C. Wang, S. Li, Q. Zhang, X. Chang, J. Li, S. Li, S. Jia, J. Wang and L. Fu, *Adv. Energy Mater.*, 2018, **8**, 1801690.
49. L. Fang, Z. Jiang, H. Xu, L. Liu, Y. Guan, X. Gu and Y. Wang, *J. Catal.*, 2018, **357**, 238-246.
50. S. Peng, F. Gong, L. Li, D. Yu, D. Ji, T. Zhang, Z. Hu, Z. Zhang, S. Chou, Y. Du and S. Ramakrishna, *J. Am. Chem. Soc.*, 2018, **140**, 13644-13653.
51. D. Liu, C. Zhang, Y. Yu, Y. Shi, Y. Yu, Z. Niu and B. Zhang, *Nano Res.*, 2018, **11**, 603-613.
52. F. Lai, J. Feng, X. Ye, W. Zong, G. He, Y.-E. Miao, X. Han, X. Y. Ling, I. P. Parkin, B. Pan, Y. Sun and T. Liu, *J. Mater. Chem. A*, 2019, **7**, 827-833.
53. S. Li, N. Yang, L. Liao, Y. Luo, S. Wang, F. Cao, W. Zhou, D. Huang and H. Chen, *ACS Appl. Mater. Interfaces*, 2018, **10**, 37038-37045.
54. Y. Ou, W.Q. Tian, L. Liu, Y. Zhang and P. Xiao, *J. Mater. Chem. A,* 2018, **6**, 5217-5228.
55. X. Yu, J. Zhao, L.-R. Zheng, Y. Tong, M. Zhang, G. Xu, C. Li, J. Ma and G. Shi, *ACS Energy Lett.*, 2018, **3**, 237-244.
56. G. Chen, T. Wang, J. Zhang, P. Liu, H. Sun, X. Zhuang, M. Chen and X. Feng, *Adv. Mater.*, 2018, **30**, 1706279.
57. J. Hu, C. Zhang, L. Jiang, H. Lin, Y. An, D. Zhou, M. K.H. Leung and S. Yang, *Joule*, 2017, **1**, 383-393.
58. T. Kou, T. Smart, B. Yao, I. Chen, D. Thota, Y. Ping and Y. Li, *Adv. Energy Mater.*, 2018, **8**, 1703538.
59. X. Zhong, J. Tang, J. Wang, M. Shao, J. Chai, S. Wang, M. Yang, Y. Yang, N. Wang, S. Wang, B. Xu and H. Pan, *Electrochim. Acta*, 2018, **269**, 55-61.
60. J. Jian, L. Yuan, H. Qi, X. Sun, L. Zhang, H. Li, H. Yuan and S. Feng, *ACS Appl. Mater. Interfaces*, 2018, **10**, 40568-40576.
61. G. Zhang, Y.-S. Feng, W.-T. Lu, D. He, C.-Y. Wang, Y.-K. Li, X.-Y. Wang and F.-F. Cao, *ACS Catal.*, 2018, **8**, 5431-5441.
62. C. Zhang, Y. Shi, Y. Yu, Y. Du and B. Zhang, *ACS Catal.,* 2018, **8**, 8077-8083.
63. Z. Wu, J. Guo, J. Wang, R. Liu, W. Xiao, C. Xuan, K. Xia and D. Wang, *ACS Appl. Mater. Interfaces*, 2017, **9**, 5288-5294.

64. H. Liu, X. Ma, Y. Rao, Y. Liu, J. Liu, L. Wang and M. Wu, *ACS Appl. Mater. Interfaces*, 2018, **10**, 10890-10897.

65. G. Zhang, X. Zheng, Q. Xu, J. Zhang, W. Liu and J. Chen, *J. Mater. Chem. A*, 2018, **6**, 4793-4800.

66. G. Zhao, X. Wang, S. Wang, K. Rui, Y. Chen, H. Yu, J. Ma, S. X. Dou and W. Sun, *Chem. Asian J*, 2019, **14**, 301-306.

67. F. Jing, Q. Lv, Q. Wang, K. Chi, Z. Xu, X. Wang and S. Wang, *Electrochim. Acta*, 2019, **304**, 202-209.

68. Y. Zhu, H.-C. Chen, C.-S. Hsu, T.-S. Lin, C.-J. Chang, S.-C. Chang, L.-D. Tsai and H. M. Chen, *ACS Energy Lett.*, 2019, **4**, 987-994.

69. X. Wang, B. Zheng, B. Wang, H. Wang, B. Sun, J. He, W. Zhang and Y. Chen, *Electrochim. Acta*, 2019, **299**, 197-205.

70. J. Yu, Y. Tian, F. Zhou, M. Zhang, R. Chen, Q. Liu, J. Liu, C.-Y. Xu and J. Wang, *J. Mater. Chem. A*, 2018, **6**, 17353-17360.

71. Y. Yang, W. Zhang, Y. Xiao, Z. Shi, X. Cao, Y. Tang and Q. Gao, *Appl. Catal., B*, 2019, **242**, 132-139.

72. X. Wang, B. Zheng, B. Yu, B. Wang, W. Hou, W. Zhang and Y. Chen, *J. Mater. Chem. A*, 2018, **6**, 7842-7850.

73. P. Chen, K. Xu, S. Tao, T. Zhou, Y. Tong, H. Ding, L. Zhang, W. Chu, C. Wu and Y. Xie, *Adv. Mater.*, 2016, **28**, 7527-7532.

74. Y. R. Zheng, P. Wu, M. R. Gao, X. L. Zhang, F. Y. Gao, H. X. Ju, R. Wu, Q. Gao, R. You, W. X. Huang, S. J. Liu, S. W. Hu, J. Zhu, Z. Li and S. H. Yu, *Nat. Commun.*, 2018, **9**, 2533.

75. Y. Zhong, B. Chang, Y. Shao, C. Xu, Y. Wu and X. Hao, *ChemSusChem*, 2018, DOI: 10.1002/cssc.201802091.

76. H. Wang, Y. Wang, L.Tan, L. Fang, X. Yang, Z. Huang, J. Li, H. Zhang and Y. Wang, *Appl. Catal., B,* 2019, **244**, 568-575.

77. H. Jin, X. Liu, A. Vasileff, Y. Jiao, Y. Zhao, Y. Zheng and S. Z. Qiao, *ACS Nano*, 2018, **12**, 12761-12769.

78. M. Zhou, Q. Weng, Z. I. Popov, Y. Yang, L. Y. Antipina, P. B. Sorokin, X. Wang, Y. Bando and D. Golberg, *ACS Nano*, 2018, **12**, 4148-4155.

79. F. Song, W. Li, J. Yang, G. Han, P. Liao and Y. Sun, *Nat. Commun.*, 2018, **9**, 4531.

80. J. Hou, Y. Sun, Z. Li, B. Zhang, S. Cao, Y. Wu, Z. Gao and L. Sun, *Adv. Funct. Mater.*, 2018, **28**, 1803278.

81. Z. Sun, J. Zhang, J. Xie, X. Zheng, M. Wang, X. Li and B. Tang, *Inorg. Chem.Front.*, 2018, **5**, 3042-3045.

82. Q. Liu, C. Tang, S. Lu, Z. Zou, S. Gu, Y. Zhang and C. M. Li, *Chem. Commun. (Camb)*, 2018, **54**, 12408-12411.

83. Q. Mo, W. Zhang, L. He, X. Yu and Q. Gao, *Appl. Catal., B*, 2019, **244**, 620-627.

84. S. Chu, W. Chen, G. Chen, J. Huang, R. Zhang, C. Song, X. Wang, C. Li and K. (Ken) Ostrikov, *Appl. Catal., B,* 2019, **243**, 537-545.

85. L. Zhang, X. Wang, X. Zheng, L. Peng, J. Shen, R. Xiang, Z. Deng, L. Li, H. Chen and Z. Wei, *ACS Appl. Energy Mater.*, 2018, **1**, 5482.

86. Y. Men, P. Li, J. Zhou, G. Cheng, S. Chen and W. Luo, *ACS Catal.*, 2019, **9**, 3744-3752.

87. K. Xu, Y. Sun, Y. Sun, Y. Zhang, G. Jia, Q. Zhang, L. Gu, S. Li, Y. Li and H. J. Fan, *ACS Energy Lett.*, 2018, **3**, 2750-2756.

88. Y. Liu, S. Liu, Y. Wang, Q. Zhang, L. Gu, S. Zhao, D. Xu, Y. Li, J. Bao and Z. Dai, *J. Am. Chem. Soc.*, 2018, **140**, 2731-2734.

89. F. Yu, H. Zhou, Y. Huang, J. Sun, F. Qin, J. Bao, W. A. Goddard, 3rd, S. Chen and Z. Ren, *Nat. Commun.*, 2018, **9**, 2551.

90. L. Ji, J. Wang, X. Teng, H. Dong, X. He and Z. Chen, *ACS Appl. Mater. Interfaces*, 2018, **10**, 14632-14640.

91. H. Yan, Y. Xie, Y. Jiao, A. Wu, C. Tian, X. Zhang, L. Wang and H. Fu, *Adv. Mater.*, 2018, **30**, 1704156.

92. X. Luo, Q. Zhou, S. Du, J. Li, L. Zhang, K. Lin, H. Li, B. Chen, T. Wu, D. Chen, M. Chang and Y. Liu, *ACS Appl. Mater. Interfaces*, 2018, **10**, 42335-42347.

93. J. Xiong, J. Li, J. Shi, X. Zhang, N.-T. Suen, Z. Liu, Y. Huang, G. Xu, W. Cai, X. Lei, L. Feng, Z. Yang, L. Huang and H. Cheng, *ACS Energy Lett.*, 2018, **3**, 341-348.

94. X. Chen, Z. Yu, L. Wei, Z. Zhou, S. Zhai, J. Chen, Y. Wang, Q. Huang, H. E. Karahan, X. Liao and Y. Chen, *J. Mater. Chem. A*, 2019, **7**, 764-774.

95. W. Hao, R. Wu, R. Zhang, Y. Ha, Z. Chen, L. Wang, Y. Yang, X. Ma, D. Sun, F. Fang and Y. Guo, *Adv. Energy Mater.*, 2018, **8**, 1801372.

96. Y. Yang, J. Liu, S. Guo, Y. Liu, and Z. Kang, *J. Mater. Chem. A*, 2015, **3**, 18598-18604.

97. M.A. McArthur, L. Jorge, S. Coulombe and S. Omanovic, *J. Power Sources,* 2014, **266**, 365-373.

98. X.-F. Yang, A. Wang, B. Qiao, J. Li, J. Liu and T. Zhang, *Accounts Chem. Res.,* 2013, **46**, 1740-1748.

99. M. Sheng, W. Weng, Y. Wang, Q. Wu and S. Hou, *J. Alloys Compd.,* 2018, **743**, 682-690.

100. D.S.P. Cardoso, L. Amaral, D.M.F. Santos, B. Sljukic, C.A.C. Sequeira, D. Maccio and A. Saccone, *Int. J. Hydrogen Energy*, 2015, **40**, 4295-4302.

101. J. Zhang, M. D. Baro, E. Pellicer and J. Sort, *Nanoscale*, 2014, **6**, 12490-12499.

102. W. Gao, W. Gou, X. Zhou, J. C. Ho, Y. Ma and Y. Qu, *ACS Appl. Mater. Interfaces*, 2018, **10**, 1728-1733.

103. M. Fang, W. Gao, G. Dong, Z. Xia, S. Yi, Y. Qin, Y. Qu and J. C. Ho, *Nano Energy,* 2016, **27**, 247-254.

104. P. M. Csernica, J. R. Mckone, C. R. Mulzer, W. R. Dichtel, H. D. Abruña and F. J. DiSalvo, *ACS Catal.*, 2017, **7**, 3375-3383.

105. M. Kuang, Q. Wang, P. Han and G. Zheng, *Adv. Energy Mater.*, 2017, **7**, 1700193.

106. Z. Cao, H. Li, C. Zhan, J. Zhang, W. Wang, B. Xu, F. Lu, Y. Jiang, Z. Xie and L. Zheng, *Nanoscale*, 2018, **10**, 5072-5077.

107. J. Chen, G. Xia, P. Jiang, Y. Yang, R. Li, R. Shi, J. Su and Q. Chen, *ACS Appl. Mater. Interfaces*, 2016, **8**, 13378-13383.

108. X. Yu, M. Zhang, Y. Tong, C. Li and G. Shi, *Adv. Energy Mater.*, 2018, **8**, 1800403.

109. L. Xie, Q. Liu, X. Shi, A. M. Asiri, Y. Luo and X. Sun, *Inorg. Chem. Front.*, 2018, **5**, 1365.

110. Z. Cao, Q. Chen, J. Zhang, H. Li, Y. Jiang, S. Shen, G. Fu, B. A. Lu, Z. Xie and L. Zheng, *Nat. Commun.*, 2017, **8**, 15131.

111. A. Oh, Y. J. Sa, H. Hwang, H. Baik, J. Kim, B. Kim, S. H. Joo and K. Lee, *Nanoscale*, 2016, **8**, 16379-16386.

112. W. Ahn, M. G. Park, D. U. Lee, M. H. Seo, G. Jiang, Z. P. Cano, F. M. Hassan and Z. Chen, *Adv. Funct. Mater.*, 2018, **28**, 1802129.

113. P. Zou, J. Li, Y. Zhang, C. Liang, C. Yang and H. J. Fan, *Nano Energy*, 2018, **51**, 349-357.

114. X. Feng, X. Bo and L. Guo, *J. Power Sources*, 2018, **389**, 249-259.

115. J. M. V. Nsanzimana, Y. Peng, M. Miao, V. Reddu, W. Zhang, H. Wang, B. Y. Xia and X. Wang, *ACS Appl. Nano Mater.*, 2018, **1**, 1228-1235.

116. A. Wang, H. Li, J. Xiao, Y. Lu, M. Zhang, K. Hu and K. Yan, *ACS Sustainable Chem. Eng.*, 2018, 6, 15995-16000.

117. R. Tong, Z. Sun, X. Wang, S. Wang and H. Pan, *ChemElectroChem*, 2019, **6**, 1338-1343.

118. T. Zhang, M.-Y. Wu, D.-Y. Yan, J. Mao, H. Liu, W. Hu, X.-W. Du, T. Ling and S.-Z. Qiao, *Nano Energy,* 2018, **43**, 103-109.

119. L. Yang, H. Zhou, X. Qin, X. Guo, G. Cui, A. M. Asiri and X. Sun, *Chem. Commun. (Camb)*, 2018, **54**, 2150-2153.

120. X. Wen, X. Yang, M. Li, L. Bai and J. Guan, *Electrochim. Acta,* 2019, **296**, 830-841.

121. R. Li, D. Zhou, J. Luo, W. Xu, J. Li, S. Li, P. Cheng and D. Yuan, *J. Power Sources,* 2017, **341**, 250-256.

122. H. Begum, M. S. Ahmed and S. Jeon, *Electrochim. Acta,* 2019, **296**, 235-242.

123. W. Zhou, X. F. Lu, J. J. Chen, T. Zhou, P. Q. Liao, M. Wu and G. R. Li, *ACS Appl. Mater. Interfaces*, 2018, **10**, 38906-38914.

124. Y. Gong, Z. Yang, Y. Lin, J. Wang, H. Pan and Z. Xu, *J. Mater. Chem. A,* 2018, **6**, 16950-16958.

125. Q. Zhou, T.-T. Li, J. Qian, Y. Hu, F. Guo and Y.-Q. Zheng, *J. Mater. Chem. A*, 2018, **6**, 14431-14439.

126. X. Shang, J.-Q. Chi, S.-S. Lu, B. Dong, Z.-Z. Liu, K.-L. Yan, W.-K. Gao, Y.-M. Chai, and C.-G. Liu, *Electrochim. Acta*, 2017, **256**, 100-109.

127. R. Zhang, X. Ren, S. Hao, R. Ge, Z. Liu, A. M. Asiri, L. Chen, Q. Zhang and X. Sun, *J. Mater. Chem. A*, 2018, **6**, 1985-1990.

128. R. Xiang, Y. Duan, L. Peng, Y. Wang, C. Tong, L. Zhang and Z. Wei, *Appl. Catal., B*, 2019, **246**, 41-49.

129. Z.-J. Chen, G.-X. Cao, L.-Y. Gan, H. Dai, N. Xu, M.-J. Zang, H.-B. Dai, H. Wu and P. Wang, *ACS Catal.*, 2018, **8**, 8866-8872.

130. R. Shi, J. Wang, Z. Wang, T. Li and Y.-F. Song, *J. Energy Chem.*, 2019, **33**, 74-80.

131. Q. Qin, P. Li, L. Chen and X. Liu, *ACS Appl. Mater. Interfaces*, 2018, **10**, 39828-39838.

132. L. An, J. Feng, Y. Zhang, R. Wang, H. Liu, G.-C. Wang, F. Cheng and P. Xi, *Adv. Funct. Mater.*, 2018, **29**, 1805298.

133. W. Lu, Y. Song, M. Dou, J. Ji and F. Wang, *Chem. Commun.*, 2018, **54**, 646-649.

134. J. Liu, D. Zhu, T. Ling, A. Vasileff and S.-Z. Qiao, *Nano Energy*, 2017, **40**, 264-273.

135. K. Choi, I. K. Moon and J. Oh, *J. Mater. Chem. A*, 2018, **7**, 1468.

136. L. Wang, C. Gu, X. Ge, J. Zhang, H. Zhu and J. Tu, *ChemNanoMat*, 2018, **4**, 124-131.

137. X. Gao, H. Zhang, Q. Li, X. Yu, Z. Hong, X. Zhang, C. Liang and Z. Lin, *Angew. Chem. Int. Ed. Engl.*, 2016, **55**, 6290-6294.

138. S. Anantharaj, K. Karthick and S. Kundu, *Mater. Today Energy*, 2017, **6**, 1-26.

139. X. Zhang, S. Zhu, L. Xia, C. Si, F. Qu and F. Qu, *Chem. Commun. (Camb)*, 2018, **54**, 1201-1204.

140. H. Yang, C. Wang, F. Hu, Y. Zhang, H. Lu and Q. Wang, *Sci. China Mater.*, 2017 **60**, 1121-1128.

141. H. Yin, S. Zhao, K. Zhao, A. Muqsit, H. Tang, L. Chang, H. Zhao, Y. Gao and Z. Tang, *Nat. Commun.*, 2015, **6**, 6430.

142. Y. Wang, H. Zhuo, X. Zhang, X. Dai, K. Yu, C. Luan, L. Yu, Y. Xiao, J. Li, M. Wang and F. Gao, *Nano Energy,* 2018, **48**, 590-599.

143. L. Xie, X. Ren, Q. Liu, G. Cui, R. Ge, A. M. Asiri, X. Sun, Q. Zhang and L. Chen, *J. Mater. Chem. A*, 2018, **6**, 1967-1970.

144. Z. Xing, C. Han, D. Wang, Q. Li and X. Yang, *ACS Catal.*, 2017, **7**, 7131-7135.

145. U. K. Sultana, J. D. Riches and A. P. O'Mullane, *Adv. Funct. Mater.*, 2018, **28**, 1870306.

146. Z. Wang, X. Ren, X. Shi, A. M. Asiri, L. Wang, X. Li, X. Sun, Q. Zhang and H. Wang, *J. Mater. Chem. A*, 2018, **6**, 3864-3868.

147. B. Shang, P. Ma, J. Fan, L. Jiao, Z. Liu, Z. Zhang, N. Chen, Z. Cheng, X. Cui and W. Zheng, *Nanoscale*, 2018, **10**, 12330-12336.

148. Z. Zhu, H. Yin, C. T. He, M. Al-Mamun, P. Liu, L. Jiang, Y. Zhao, Y. Wang, H. G. Yang, Z. Tang, D. Wang, X. M. Chen and H. Zhao, *Adv. Mater.*, 2018, **30**, e1801171.

149. L. Zhang, I. S. Amiinu, X. Ren, Z. Liu, G. Du, A. M. Asiri, B. Zheng and X. Sun, *Inorg. Chem.*, 2017, **56**, 13651-13654.

150. X. Wang, R. Liu, Y. Zhang, L. Zeng and A. Liu, *Appl. Surf. Sci.,* 2018, **456**, 164-173.

151. L. Chen, J. Zhang, X. Ren, R. Ge, W. Teng, X. Sun and X. Li, *Nanoscale*, 2017, **9**, 16632-16637.

152. C. Liu, Q. Chen, Q. Hao, X. Zheng, S. Li, D. Jia, T. Gong, H. Liu and J. Zhang, *Int. J. Hydrogen Energy*, 2019, **44**, 4832-4838.

153. S.-Q. Liu, H.-R. Wen, G. Ying, Y.-W. Zhu, X.-Z. Fu, R. Sun and C.-P. Wong, *Nano Energy*, 2018, **44**, 7-14.

154. D. Kim, J. Park, J. Lee, Z. Zhang and K. Yong, *ChemSusChem*, 2018, **11**, 3618-3624.

155. Z. Zhang, Y. Jiang, X. Zheng, X. Sun and Y. Guo, *New J. Chem.*, 2018, **42**, 11285-11288.

156. X. Wang, Y. Yang, L. Diao, Y. Tang, F. He, E. Liu, C. He, C. Shi, J. Li, J. Sha, S. Ji, P. Zhang, L. Ma and N. Zhao, *ACS Appl. Mater. Interfaces*, 2018, **10**, 35145-35153.
157. J. Joo, T. Kim, J. Lee, S. I. Choi and K. Lee, *Adv. Mater.*, 2019, DOI: 10.1002/adma.201806682, e1806682.
158. J. Staszak-Jirkovský, C. D. Malliakas, P. P. Lopes, N. Danilovic, S. S. Kota, K.-C. Chang, B. Genorio, D. Strmcnik, V. R. Stamenkovic and M. G. Kanatzidis, *Nat. Mater.*, 2016, **15**, 197.
159. Q. Ding, B. Song, P. Xu and S. Jin, *Chem*, 2016, **1**, 699-726.
160. H. Wang, C. Li, P. Fang, Z. Zhang and J. Z. Zhang, *Chem. Soc. Rev.*, 2018, **47**, 6101-6127.
161. F. Yu, H. Yao, B. Wang, K. Zhang, Z. Zhang, L. Xie, J. Hao, B. Mao, H. Shen and W. Shi, *Dalton Trans.*, 2018, **47**, 9871-9876.
162. Y. Qu, M. Yang, J. Chai, Z. Tang, M. Shao, C. T. Kwok, M. Yang, Z. Wang, D. Chua, S. Wang, Z. Lu and H. Pan, *ACS Appl. Mater. Interfaces*, 2017, **9**, 5959-5967.
163. H. Du, R. Kong, F. Qu and L. Lu, *Chem. Commun. (Camb)*, 2018, **54**, 10100-10103.
164. H. Zhang and R. Lv, *Journal of Materiomics*, 2018, **4**, 95-107.
165. Y. Jia, J. Chen and X. Yao, *Mater. Chem. Front.*, 2018, **2**, 1250-1268.
166. M. Q. Yang, J. Wang, H. Wu and G. W. Ho, *Small*, 2018, **14**, e1703323.
167. Y. Wang, Y. Zhu, S. Afshar, M. W. Woo, J. Tang, T. Williams, B. Kong, D. Zhao, H. Wang and C. Selomulya, *Nanoscale*, 2019, **11**, 3500-3505.
168. J. Wang, Y. Gao and F. Ciucci, *ACS Appl. Energy Mater.*, 2018, **1**, 6409-6416.
169. Y. Luo, X. Li, X. Cai, X. Zou, F. Kang, H. M. Cheng and B. Liu, *ACS Nano*, 2018, **12**, 4565-4573.
170. J. Cao, J. Zhou, Y. Zhang, Y. Wang and X. Liu, *ACS Appl. Mater. Interfaces*, 2018, **10**, 1752-1760.
171. J.-Q. Chi, Y.-M. Chai, X. Shang, B. Dong, W. Zhang and Z. Jin, *J. Mater. Chem. A*, 2018, **6**, 24783-24792.
172. P. Wang, X. Zhang, J. Zhang, S. Wan, S. Guo, G. Lu, J. Yao and X. Huang, *Nat. Commun.*, 2017, **8**, 14580.
173. T. An, Y. Wang, J. Tang, W. Wei, X. Cui, A. M. Alenizi, L. Zhang and G. Zheng, *J. Mater. Chem. A*, 2016, **4**, 13439-13443.
174. Y.-S. Cheng, M. Ling, B.-B. Jiang, F.-H. Wu, Z.-H. Zhao, X.-N. Li, P.-F. He and X.-W. Wei, *ChemElectroChem*, 2019, **6**, 748-756.
175. Q. Qin, L. Chen, T. Wei and X. Liu, *Small*, 2018, 1803639.
176. Y. Gong, K. Tao and J. Lin, *Electrochim. Acta*, 2018, **274**, 74-83.
177. F. Jing, Q. Lv, J. Xiao, Q. Wang and S. Wang, *J. Mater. Chem. A*, 2018, **6**, 14207-14214.
178. F. Du, Z. Chen Y. Zhang, H. He, Y. Zhou, T. Li and Z. Zou, *Electrochem. Commun.*, 2019, **99**, 22-26.
179. M. Basu, *Chem. Asian J.*, 2018, **13**, 3204-3211.
180. S. Wan, W. Jin, X. Guo, J. Mao, L. Zheng, J. Zhao, J. Zhang, H. Li and C. Tang, *ACS Sustainable Chem. Eng.*, 2018, **6**, 15374-15382.
181. J. Yu, W.-J. Li, H. Zhang, F. Zhou, R. Li, C.-Y. Xu, L. Zhou, H. Zhong and J. Wang, *Nano Energy*, 2019, **57**, 222-229.
182. Y. Guo, D. Guo, F. Ye, K. Wang, Z. Shi, X. Chen and C. Zhao, *ACS Sustainable Chem. Eng.*, 2018, **6**, 11884-11891.
183. H. Wang, X. Wang, D. Yang, B. Zheng and Y. Chen, *J. Power Sources*, 2018, **400**, 232-241.
184. R. Bose, B. Patil, V. R. Jothi, T.-H. Kim, P. Arunkumar, H. Ahn and S. C. Yi, *J. Ind. Eng. Chem.*, 2018, **65**, 62-71.
185. J. Chen, A. Pan, Y. Wang, X. Cao, W. Zhang, X. Kong, Q. Su, J. Lin, G. Cao and S. Liang, *Energy Storage Materials*, 2018, DOI: 10.1016/j.ensm.2018.10.019.
186. Z. Huang, J. Liu, Z. Xiao, H. Fu, W. Fan, B. Xu, B. Dong, D. Liu, F. Dai and D. Sun, *Nanoscale*, 2018, **10**, 22758-22765.
187. B. Wang, Z. Wang, X. Wang, B. Zheng, W. Zhang and Y. Chen, *J. Mater. Chem. A*, 2018, **6**, 12701-12707.

188. H. Sun, J.-G. Li, L. Lv, Z. Li, X. Ao, C. Xu, X. Xue, G. Hong and C. Wang, *J. Power Sources*, 2019, **425**, 138-146.

189. L. Najafi, S. Bellani, R. Oropesa-Nuñez, A. Ansaldo, M. Prato, A. E. Del Rio Castillo and F. Bonaccorso, *Adv. Energy Mater.*, 2018, **8**, 1703212.

190. G. Zhao, P. Li, K. Rui, Y. Chen, S. X. Dou and W. Sun, *Chemistry*, 2018, **24**, 11158-11165.

191. C. Liu, K. Wang, X. Zheng, X. Liu, Q. Liang and Z. Chen, *Carbon*, 2018, **139**, 1-9.

192. C. Wang, P. Zhang, J. Lei, W. Dong and J. Wang, *Electrochim. Acta*, 2017, **246**, 712-719.

193. L. Najafi, S. Bellani, R. Oropesa-Nunez, M. Prato, B. Martin-Garcia, R. Brescia and F. Bonaccorso, *ACS Nano*, 2019, **13**, 3162-3176.

194. U. De Silva, J. Masud, N. Zhang, Y. Hong, W. P. R. Liyanage, M. Asle Zaeem and M. Nath, *J. Mater. Chem. A*, 2018, **6**, 7608-7622.

195. E.-K. Kim, H. T. Bui, N. K. Shrestha, C. Y. Shin, S. A. Patil, S. Khadtare, C. Bathula, Y.-Y. Noh and S.-H. Han, *Electrochim. Acta*, 2018, **260**, 365-371.

196. X. Wang, X. Huang, W. Gao, Y. Tang, P. Jiang, K. Lan, R. Yang, B. Wang and R. Li, *J. Mater. Chem. A*, 2018, **6**, 3684-3691.

197. Y. Ge, S. P. Gao, P. Dong, R. Baines, P. M. Ajayan, M. Ye and J. Shen, *Nanoscale*, 2017, **9**, 5538-5544.

198. S. Anantharaj, K. Karthick and S. Kundu, *Inorg. Chem.*, 2018, **57**, 3082-3096.

199. T. Kosmala, H. Coy Diaz, H.-P. Komsa, Y. Ma, A. V. Krasheninnikov, M. Batzill and S. Agnoli, *Adv. Energy Mater.*, 2018, **8**, 1800031.

200. X. Peng, C. Pi, X. Zhang, S. Li, K. Huo and P. K. Chu, *Sustainable Energy Fuels*, 2019, DOI: 10.1039/c8se00525g.

201. S. Dutta, A. Indra, Y. Feng, H. Han and T. Song, *Appl. Catal., B,* 2019, **241**, 521-527.

202. X. Shi, A. Wu, H. Yan, L. Zhang, C. Tian, L. Wang and H. Fu, *J. Mater. Chem. A*, 2018, **6**, 20100-20109.

203. Z. Lv, M. Tahir, X. Lang, G. Yuan, L. Pan, X. Zhang and J.-J. Zou, *J. Mater. Chem. A*, 2017, **5**, 20932-20937.

204. L. Gan, L. Hu, H. An, J. Fang, Y. Lai and J. Li, *ACS Appl. Mater. Interfaces*, 2018, **10**, 41465.

205. F. Yan, Y. Wang, K. Li, C. Zhu, P. Gao, C. Li, X. Zhang and Y. Chen, *Chemistry*, 2017, **23**, 10187-10194.

206. S. Wang, H. Ge, S. Sun, J. Zhang, F. Liu, X. Wen, X. Yu, L. Wang, Y. Zhang and H. Xu, *J. Am. Chem. Soc.*, 2015, **137**, 4815-4822.

207. F.-C. Shen, S.-N. Sun, Z.-F. Xin, S.-L. Li, L.-Z. Dong, Q. Huang, Y.-R. Wang, J. Liu and Y.-Q. Lan, *Appl. Catal., B*, 2019, **243**, 470-480.

208. M.-Q. Wang, C. Tang, C. Ye, J. Duan, C. Li, Y. Chen, S.-J. Bao and M. Xu, *J. Mater.Chem. A*, 2018, **6**, 14734-14741.

209. M. Fan, Y. Zheng, A. Li, K. Li, H. Liu and Z.-A. Qiao, *Catal. Sci. Technol.*, 2018, **8**, 3695-3703.

210. C. Zhu, A. L. Wang, W. Xiao, D. Chao, X. Zhang, N. H. Tiep, S. Chen, J. Kang, X. Wang, J. Ding, J. Wang, H. Zhang and H. J. Fan, *Adv. Mater.*, 2018, **30**, e1705516.

211. Y. Xiao, C. Tian, M. Tian, A. Wu, H. Yan, C. Chen, L. Wang, Y. Jiao and H. Fu, *Sci.China Mater.*, 2017, **61**, 80-90.

212. Y. Wang, B. Kong, D. Zhao, H. Wang and C. Selomulya, *Nano Today*, 2017, **15**, 26-55.

213. Y. Shao, X. Shi and H. Pan, *Chem. Mater.*, 2017, **29**, 8892-8900.

214. Y. Pei, Y. Ge, H. Chu, W. Smith, P. Dong, P. M. Ajayan, M. Ye and J. Shen, *Appl. Catal., B,* 2019, **244**, 583-593.

215. X. Zhang, X. Zhang, H. Xu, Z. Wu, H. Wang and Y. Liang, *Adv. Funct. Mater.*, 2017, **27**, 1606635.

216. Y. Liu, Y. Du, W.-K. Gao, B. Dong, Y. Han and L. Wang, *Electrochim. Acta*, 2018, **290**, 339-346.

217. S. Liu, Q. Liu, Y. Lv, B. Chen, Q. Zhou, L. Wang, Q. Zheng, C. Che and C. Chen, *Chem. Commun. (Camb)*, 2017, **53**, 13153-13156.

DOI: 10.1039/C9TA03220G

218. J. Li, M. Yan, X. Zhou, Z.-Q. Huang, Z. Xia, C.-R. Chang, Y. Ma and Y. Qu, *Adv. Funct. Mater.*, 2016, **26**, 6785-6796.

219. H. Du, L. Xia, S. Zhu, F. Qu and F. Qu, *Chem. Commun. (Camb)*, 2018, **54**, 2894-2897.

220. L. Zhang, Y. Yang, M. A. Ziaee, K. Lu and R. Wang, *ACS Appl. Mater. Interfaces*, 2018, **10**, 9460-9467.

221. C. Zhang, Z. Pu, I. S. Amiinu, Y. Zhao, J. Zhu, Y. Tang and S. Mu, *Nanoscale*, 2018, **10**, 2902-2907.

222. X. Zhang, X. Yu, L. Zhang, F. Zhou, Y. Liang and R. Wang, *Adv. Funct. Mater.*, 2018, **28**, 1706523.

223. M. Q. Wang, C. Ye, H. Liu, M. Xu and S. J. Bao, *Angew. Chem. Int. Ed. Engl.*, 2018, **57**, 1963-1967.

224. M. Miao, R. Hou, Z. Liang, R. Qi, T. He, Y. Yan, K. Qi, H. Liu, G. Feng and B. Y. Xia, *J. Mater. Chem. A*, 2018, **6**, 24107.

225. T. Liu, S. Wang, Q. Zhang, L. Chen, W. Hu and C. M. Li, *Chem. Commun. (Camb)*, 2018, **54**, 3343-3346.

226. Y. Li, H. Li, K. Cao, T. Jin, X. Wang, H. Sun, J. Ning, Y. Wang and L. Jiao, *Energy Storage Materials,* 2018, **12**, 44-53.

227. N. Bai, Q. Li, D. Mao, D. Li and H. Dong, *ACS Appl. Mater. Interfaces*, 2016, **8**, 29400-29407.

228. H. Zheng, X. Huang, H. Gao, G. Lu, W. Dong and G. Wang, *Chemistry*, 2019, **25**, 1083-1089.

229. L. Zhang, M. Cong, Y. Wang, X. Ding, A. Liu and Y. Gao, *ChemElectroChem*, 2019, **6**, 1329-1332.

230. Y. Zhou, T. Li, S. Xi, C. He, X. Yang and H. Wu, *ChemCatChem*, 2018, **10**, 5487-5495.

231. L. Yu, Y. Xiao, C. Luan, J. Yang, H. Qiao, Y. Wang, X. Zhang, X. Dai, Y. Yang and H. Zhao, *ACS Appl. Mater. Interfaces*, 2019, **11**, 6890-6899.

232. Y. Ge, P. Dong, S. R. Craig, P. M. Ajayan, M. Ye and J. Shen, *Adv. Energy Mater.*, 2018, **8**, 1800484.

233. N. Chen, Q. Mo, L. He, X. Huang, L. Yang, J. Zeng and Q. Gao, *Electrochim. Acta*, 2019, **299**, 708-716.

234. Z. Kou, L. Zhang, Y. Ma, X. Liu, W. Zang, J. Zhang, S. Huang, Y. Du, A. K. Cheetham and J. Wang, *Appl. Catal., B,* 2019, **243**, 678-685.

235. Q. Gao, W. Zhang, Z. Shi, L. Yang and Y. Tang, *Adv. Mater.*, 2019, **31**, e1802880.

236. Q. Hu, X. Liu, B. Zhu, L. Fan, X. Chai, Q. Zhang, J. Liu, C. He and Z. Lin, *Nano Energy,* 2018, **50**, 212-219.

237. Y.-Y. Ma, Z.-L. Lang, L.-K. Yan, Y.-H. Wang, H.-Q. Tan, K. Feng, Y.-J. Xia, J. Zhong, Y. Liu, Z.-H. Kang and Y.-G. Li, *Energy Environ. Sci.*, 2018, **11**, 2114-2123.

238. C. He and J. Tao, *Mater. Today Energy*, 2018, **8**, 65-72.

239. L. Peng, J. Shen, L. Zhang, Y. Wang, R. Xiang, J. Li, L. Li and Z. Wei, *J. Mater. Chem. A*, 2017, **5**, 23028-23034.

240. W. Xiong, Q. Guo, Z. Guo, H. Li, R. Zhao, Q. Chen, Z. Liu and X. Wang, *J. Mater.Chem. A*, 2018, **6**, 4297-4304.

241. X. Chen, J. Qi, P. Wang, C. Li, X. Chen and C. Liang, *Electrochim. Acta*, 2018, **273**, 239-247.

242. R. Wang, P. Sun, H. Wang and X. Wang, *Int. J. Hydrogen Energy*, 2018, **43**, 17244-17251.

243. Y. Huang, J. Ge, J. Hu, J. Zhang, J. Hao and Y. Wei, *Adv. Energy Mater.*, 2018, **8**, 1701601.

244. G. Yan, C. Wu, H. Tan, X. Feng, L. Yan, H. Zang and Y. Li, *J. Mater. Chem. A*, 2017, **5**, 765-772.

245. G. Yan, X. Feng, S. U. Khan, L. Xiao, W. Xi, H. Tan, Y. Ma, L. Zhang and Y. Li, *Chem. Asian J.*, 2018, **13**, 158-163.

246. J. Chen, J. Jia, Z. Wei, G. Li, J. Yu, L. Yang, T. Xiong, W. Zhou and Q. Tong, *Int. J. Hydrogen Energy*, 2018, **43**, 14301-14309.

247. T. Ouyang, Y. Q. Ye, C. Y. Wu, K. Xiao and Z. Q. Liu, *Angew. Chem. Int. Ed. Engl.*, 2019, **58**, 4923-4928.

248. S. Li, C. Cheng, A. Sagaltchik, P. Pachfule, C. Zhao and A. Thomas, *Adv. Funct. Mater.*, 2019, **29**, 1807419.

249. Y.-Q. Wang, Y. Xie, L. Zhao, X.-L. Sui, D.-M. Gu and Z.-B. Wang, *ACS Sustainable Chem. Eng.*, 2019, **7**, 7294-7303.

250. Z. Wei, X. Hu, S. Ning, X. Kang and S. Chen, *ACS Sustainable Chem. Eng.*, 2019, DOI: 10.1021/acssuschemeng.9b00210.

251. Z. Zhuang, Y. Li, Z. Li, F. Lv, Z. Lang, K. Zhao, L. Zhou, L. Moskaleva, S. Guo and L. Mai, *Angew. Chem. Int. Ed. Engl.*, 2018, **57**, 496-500.

252. W. Yuan, X. Zhao, W. Hao, J. Li, L. Wang, X. Ma and Y. Guo, *ChemElectroChem*, 2019, **6**, 764-770.

253. M. Cao, X. Zhang, J. Qin and R. Liu, *ACS Sustainable Chem. Eng.*, 2018, **6**, 16198-16204.

254. Z. Chen, Q. Kang, G. Cao, N. Xu, H. Dai, and P. Wang, *Int. J. Hydrogen Energy,* 2018, **43**, 6076-6087.

255. H. Li, P. Wen, Q. Li, C. Dun, J. Xing, C. Lu, S. Adhikari, L. Jiang, D. L. Carroll and S. M. Geyer, *Adv. Energy Mater.,* 2017, **7**, 1700513.

256. Q. Li, X. Zou, X. Ai, H. Chen, L. Sun and X. Zou, *Adv. Energy Mater.*, 2019, **9**, 1803369.

257. M. Sheng, Q. Wu, Y. Wang, F. Liao, Q. Zhou, J.n Hou and W. Weng, *Electrochem. Commun.,* 2018, **93**, 104-108.

258. Z. Sun, S. Hao, X. Ji, X. Zheng, J. Xie, X. Li and B. Tang, *Dalton Trans.*, 2018, **47**, 7640-7643.

259. N. P. S. Guptaa, R. Fernandes, S. Hanchate, A. Miotello and D.C. Kothari, *Electrochim. Acta,* 2017, **232**, 64-71.

260. S. Gupta, N. Patel, R. Fernandes, R. Kadrekar, A. Dashora, A.K. Yadav, D. Bhattacharyya, S.N. Jha, A. Miotello and D.C. Kothari, *Appl. Catal., B,* 2016, **192**, 126-133.

261. G.-X. Cao, N. Xu, Z.-J. Chen, Q. Kang, H.-B. Dai and P. Wang, *ChemistrySelect*, 2017, **2**, 6187-6193.

262. H. Sun, X. Xu, Z. Yan, X. Chen, L. Jiao, F. Cheng and J. Chen, *J. Mater. Chem. A*, 2018, **6**, 22062-22069.

263. C. Hu and L. Dai, *Adv. Mater.*, 2017, **29**, 1604942.

264. Q. Wang, Y. Ji, Y. Lei, Y. Wang, Y. Wang, Y. Li and S. Wang, ACS Energy Lett., 2018, **3**, 1183-1191.

265. Q. Hu, G. Li, X. Liu, B. Zhu, G. Li, L. Fan, X. Chai, Q. Zhang, J. Liu and C. He, J. Mater. Chem. A, 2019, **7**, 461-468.

266. Q. Hu, G. Li, G. Li, X. Liu, B. Zhu, X. Chai, Q. Zhang, J. Liu and C. He, Adv. Energy Mater., 2019, **9**, 1803867.

267. X. Liu, Q. Hu, B. Zhu, G. Li, L. Fan, X. Chai, Q. Zhang, J. Liu and C. He, Small, 2018, **14**, e1802755.

268. C. Song, Z. Zhao, X. Sun, Y. Zhou, Y. Wang and D. Wang, *Small*, 2019, 1804268.

269. N. Xu, G. Cao, Z. Chen, Q. Kang, H. Dai and P. Wang, *J. Mater. Chem. A*, 2017, **5**, 12379-12384.

270. X. Xu, Y. Deng, M. Gu, B. Sun, Z. Liang, Y. Xue, Y. Guo, J. Tian and H. Cui, *Appl. Surf. Sci.*, 2019, **470**, 591-595.

271. J. Liu, D. Zhu, C. Guo, A. Vasileff and S.-Z. Qiao, *Adv. Energy Mater.*, 2017, **7**, 1700518.

2001

View Article Online
DOI: 10.1039/C9TA03220G